Republic of Iraq
Ministry of Higher Education and Scientific Research
University of Babylon
college of scientific for women
Department of Laser Physics

A Study of the Plasma Emission Spectra of Au and Ag NPs Prepared by Laser Ablation

A Thesis
Submitted to the council College of Science the Department of Laser Physics University of Babylon as partial Fulfillment of the Requirement for the Degree of Master in science of Laser Physics

By

Baraa Hussam Ali

Supervised by

Assist.Prof. Dr. Lazem H. Aboud

Lect. Dr. Mohammed J. Jader

2023 A.D. **1445 A.H.**

بِسْمِ اللَّهِ الرَّحْمَٰنِ الرَّحِيمِ

يَرْفَعِ اللَّهُ الَّذِينَ آمَنُوا مِنكُمْ وَالَّذِينَ أُوتُوا الْعِلْمَ دَرَجَاتٍ

صدق الله العلي العظيم

سورة المجادلة (الآية 11)

Dedication

To my dear father..

To the memory of my dear mother..

To my husband , my daughter and my son..

To my brothers and sister..

To my friends ..

those who supported me with their love kindness, attention and encouragement..

Baraa

Acknowledgments

First of all, Thanks are due to Allah for the everlasting countless blessing.
I would like to express my sincere appreciation and deep gratitude to my supervisors‹**Assist. Prof. Dr. Lazem H. Aboud** and **Lect. Dr. Mohammed J. Jader**for their suggestions on the topic of this thesis, guidance, advice, and continuous encouragement throughout the research work.

I'm grateful to University of Babylon Department of Laser physics, and Dean of the college **Prof. Dr. Abeer F. Murad** and Assistant Dean **Assist. Prof. Dr. Saddam F. Haddawi** and the head of the department **Dr Jinan A. Abd**, for their help.

The authors would like to thank advance Laboratory **Prof. Dr. Sami A. Habana** and assit. Lect. **Rafaa T. Ahmed** , Department of Physics, College of Science, and the University of Babylon for their support and help in finishing this work ..

Baraa

Abstract

The current study focused on the plasma spectra which is emitted from gold and silver metals under the influence of laser pulses. To achieve this purpose, it is used Nd:YAG laser at wavelength of 1064 nm, pulse duration is 10 ns , laser energy is 100 mJ, the frequency is 6 Hz and 600 number of pulses focuses directly on metal targets.

Moreover, Gold and silver nanoparticles are synthesized experimentally using pulsed laser ablation in liquids. The metal nanoparticles are then deposited on silicon and glass substrates by dipping method, their emission spectra are studied using technique of Laser-induced breakdown spectroscopy (LIBS).

Thus, a comparison is made between bulk targets and nano-enhanced substrates. Plasma parameters such as, temperature, density, frequency, and Dybe length are calculated. As well as the optical, structural and electrical properties are measured by measuring Uv-Visible, XRD, FE-SEM and IV characteristics, respectively. Finally, gold and silver nanoparticles and their mixture are deposited on the surface of a solar cell to improve it is efficiency.

The obtained results proved that the Silver has larger plasma parameters than gold, this is due to the wavelength of the laser used, which causes silver to absorb laser light more than gold, this result is consistent with the results of absorption. An increase in plasma parameters was obtained when comparing plasma parameters before and after nanoparticle deposition on glass and silicon substrates.

The FE-SEM results showed the nanoparticles that the spherical shapes with the average size (13.9, 12.09 and 18.38) nm while the XRD results were showed the crystal size that were (10.9, 12.1 and 11.9) nm for each of the Au NPs, Ag NPs and their mixtures, respectively.

The results also proved the NELIBS technique can be used to improve of low-absorbance samples without causing internal cracks in the sample. This mechanism may lower the avalanche threshold of Si, thus intensities increasing of

the emission lines leading to enhanced detectability of LIBS, especially for the wavelength range from 400 to 550 nm. This is because the difference in the interaction mechanism of the laser radiation with the existing nanoparticles leads to the enhancement of the emission line.

Finally, the deposition of metal nanoparticles on the surfaces of solar cells improved their performance to obtain more power by increasing the absorption within the active layer at the plasmonic wavelength or by reducing the recombination process by increasing the surface conductivity.

List of Content

List of symbols

Symbols	Description	Units
A_{ji}	Electronic transmission probability	
d_{hkl}	Inter planar distance	Nm
E_g	Energy gap	ev
E_j	Excited upper level energy	ev
w_p	Plasma frequency	Hz
FWHM	Full width at half maximum	degree
g_j	Statistical weigh of electronic level	
D	Crystalline size	Nm
H	Planck constant	j.s
I	Ionization energy	ev
I_{ji}	Emitted line intensities	a.u
k_B	Boltzmann constant	j/k
m_e	Electron mass	Kg
N_d	Debye number	
n_e	Electron number density	cm^{-3}
N_j	Number density	cm^{-3}
T_e	Electron temperature	ev
W	work function	ev
$\Delta\lambda$	Emitted line breadth	Nm
U(T)	Partition function	
B	Diffraction line breadth	Rad
H	Plank's constant	j.s
Θ	Diffraction angle	degree
Λ	Wavelength	Nm
λ_D	Debye length	Cm
E	Lattice strain	
ε_o	vacuum permittivity	F.m
ω_p	Angular plasma frequency	rad/s

List of Abbreviations

Term	Description
FE-SEM	Field Emission-Scanning Electron Microscopy
LIPS	Laser-Induced Plasma Spectroscopy
LTE	Local Thermal Equilibrium
LIBS	Laser Induced Breakdown Spectroscopy
NPs	Nanoparticles
NELIBS	Nanoparticle Enhanced Laser Induced Breakdown Spectroscopy
OES	Optical Emission Spectroscopy
XRD	X-ray Diffraction
LSPR	Localized Surface Plasmon Resonance

List of Figures

List of Tables

Chapter One

Introduction

1.1 Introduction

The well-known method of Pulsed Laser Ablation (PLA) technique is one of the simplest way to prepare nanoparticles from various materials. A beam of pulsed laser has intensity is directed onto the target during the PLA, causing small explosions and particle ejections near the target[1]. The generated nanostructures are collected for additional analysis. Particularly, the properties of the generated nanostructures can be tuned by changing the plasma characteristics[2].

Nano science is the basis for building many modern technologies. A matter is considered to be a nanomaterial if one dimension, at least,less than 100 nm. They have completely different physical properties as compared to their bulk form [3].

A variety of techniques exist for generating nanomaterials, including chemical and physical techniques such as, vapor deposition techniques, electrolysis, and laser ablation method [4][5].

Nanomaterials display a wide range of interesting properties due to their smaller size and as a result of their higher surface-to-volume ratio compared to volumetric form. As a material approaches the nanoscale, its properties change because the surface atoms possess distinct properties. In addition, nanostructures have, such as the ability to trap electrons due to their small size, which cause quantum confinement effect[6].Metal nanoparticle such as gold and silver nanoparticle (Au NPs and Ag NPs) are considered as interesting ones due the unique optical properties of Localized Surface Plasmon Resonance (LSPR) , these noble metals exhibit new optical characteristics. So, these NPs incorporates in numerous fields of applications ranging from optoelectronic devices for medicine[7].

Laser Induced Breakdown Spectroscopy (LIBS) is one of the most popular methods for analyzing solid surfaces. This technique uses a pulsed laser to expose a very small area of the target surface to be analyzed [8].It is widely used to define the elemental composition of various substances. Recent studies frequently use [5].The LIBS to examine samples such as steels, alloys, and metals in geological, biological, and environmental research. The LIBS is also particularly adaptable because it perhaps utilized for solid, liquid, or gaseous samples. It gives immediate results, and thus has become essential for quality control in metallurgical production, by analyzing the light emitted by electronic transitions of atoms and molecules, which can identify compounds present in the plasma. It is one of the most frequently employed technologies in the production of modern electronics such as integrated circuits[9].

Since the metal nanoparticles modulate the incident electromagnetic field due to their localized surface plasmon resonance (SPR), therefore metallic nanostructures and their plasmonic effect are widely employed in laser spectroscopy. In addition, by modifying the optical properties and geometries of materials, it is possible to significantly improve their optical response [10][11]. Also, the presence of the nanomaterial strengthens the electromagnetic fields close to the surface of the particle, which allows the formation of electron seeds efficiently through the process of emission of the electron field, which leads to reducing the energy required for breakdown. Thus, by decreasing the breakdown threshold, the NPs on the sample surface can improve the LIBS spectra; This process is known as Nano Enhanced Laser Induced Breakdown Spectroscopy (NELIBS)[12].

On the other hand, the ability of each photovoltaic cell to capture high ratio of incoming light and generate electric current, which in turn has a variety of limiting constraints, determines photovoltaic cell performance. Accordingly, there are two ways to improve energy harvesting: through the use of light-trapping strategies and

by using spectral modulation techniques that shift the working spectrum band that absorbed by the cell for the maximal ratio[13].Plasmonic nanoparticles (NPs) can greatly improve solar cells by both aspects, trapping the electromagnetic field by scattering in the active layer of a solar cell within the appropriate spectral range. These spectral regions can be effectively tuned by modifying the size, shape and distribution of the NPs and the type of surrounding medium for the plasmonic NPs[14].Numerous studies over the past 10 years had been concerned with a wide range of topics on solar cell efficiency enhancement, in addition to the basic features of the solar cell enhancement by plasmonic particles such as gold and silver.

1.2 Literature Survey

Recently, interest has increased in the generation of pure and doped metal nanoparticles for use in various applications or for use in LIBS technology. Below are some recent studies that had focused on this field.

A. De Giacomo et al in (2013) [15] revealed through fast shadow images the influence of experimental parameters on the productivity of laser ablation in water. Among these parameters, laser repetition rate is crucial, which may enhance productivity by reducing production time. The main oscillation period of the cavitation bubble depends on the laser power, target material and shape. Once these parameters are determined, selection of the appropriate repetition rate becomes necessary to prevent subsequent pulses from being shielded by a cavitations bubble before reaching the target surface.

This study emphasizes how cavitation bubble dynamics, intricately linked to the analyze thickness and laser pulse parameters, significantly influence the application of laser ablation in liquids, especially in nanoparticle production. Moreover, in light of recent findings on enhanced fragmentation of laser

microcrystal with induced defects, these results can be interpreted as a dual effect of multiple shock waves leading to diverse fragment6ation phenomena .

DE GIACOMO et al , (2014) [16] used metal nanoparticles (NPs) to improve laser-induced spectroscopy (LIBS). In the case of conductors, emission signal enhancement of up to 1–2 orders of magnitude was obtained by depositing NPs on the sample surface by drying a small drop of colloidal solution. The basic mechanisms of nanoparticle-enhanced LIBS (NELIBS) were studied and the main reasons for this significantly greater enhancement were found to be related to the effect of NPs on the laser ablation process, in terms of producing seed electrons faster and more efficiently with respect to conventional LIBS. The properties of the plasma produced by NELIBS were investigated by emission spectroscopy and spectrally resolved images. Despite similar plasma parameters, NELIBS plasma was found to have a larger emission magnitude and longer stability than LIBS plasma .

Sládková *et al,* (2017) [17] studied the effect of vacuum level on the LIBS from a sample surface covered by silver NPs. The optimal enhancement of the LIBS parameters was signified with the aid of nanoparticles during laser ablation by increasing intensities of emission lines, and improving analytic sensitivity. When vacuum increased were being no significant effect on emission signals comparing to ambient pressure.

Koral *et al,* (2018) [12] used the NELIBS technique with transparent samples. The result showed no damage in the target sample, the AuNPs were deposited on the target surface before LIBS using pulsed laser of 532 nm wavelength, so that the plasmonic NPs enhanced the breakdown. The elemental analysis of exceptional specimens with high refractive indices benefited greatly from the use of this technique. In contrast, a laser on an untreated sample might penetrate it, causing breakdown below the surface layer that results in damage like cracking.

Aglio *et al*, (2018) [10] investigated on the fundamental enhancement mechanisms of LIBS by utilizing NPs. On various samples, including metals, transparent substances, and biological fluids, the interaction of high-intensity lasers with metal substrates and the laser-ablation processes boosted by nanoparticles were studied.

Sherbini *et al.* 2019 [18] investigated on the signals improvement of LIBS by different types of metal NPs of using Nd:YAG laser. They examined the influence of NPs size, laser wavelength and energy to generate best signals compare with bulk samples. Quantitative modeling infers improved detectability of atomic species in biological and chemical samples.

Zita Salajková et al, (2021) [19] demonstrated that the main attraction of non-explosive laser-induced breakdown spectroscopy (NELIBS) is its ability to enhance the intensity of emission lines compared to conventional laser-induced breakdown spectroscopy (LIBS). This enhancement is measured by measuring the ratio of NELIBS intensity to LIBS intensity. The effect of different sizes of spherical gold nanoparticles (Au NPs) on NELIBS enhancement was studied. Experimental results indicate that once an optimal distance between dried NPs in the sample is achieved to facilitate effective plasmon coupling with the laser electromagnetic field, the size of the NPs has little effect on the maximum signal enhancement. It can be concluded that different NP sizes correspond to different optimal distances between NPs, where larger NPs require larger distances to achieve optimization .

Ahmed *et al*, (2022) [20] synthesized of Au NPs using a PLA technique with 355 nm wavelength at different laser energies, and deposited on porous Si. Optical emission spectrometer was used to diagnose medium air to study the plasma characteristics in air. The results displayed on the rise of ionic gold emission lines.

Fadhil *et al*, (2022) [21] utilized a pulsed Nd-YAG laser of 1064 nm wavelength at different fluencies of pulsed laser in LIBS technique from different

Ag target configurations (nanoparticles and bulk samples to study the effect of target properties and laser energy on the plasma features. A comparison between NPs and their bulk form, NPs targets displayed a visible development in the emission lines intensity. Increasing laser fluence cause exponential decayed of atomic lines. Due the change in the basic properties of the NPs irradiated by high intensity laser details were advanced. The electron density and the temperature increased with the laser, and the Ag samples in the form of NPs clearly displayed enhancement of LIBS signals.

Hameed *et al*, (2022) [22] studied the emission lines of LIBS from three metallic targets (Cu, Ti and Ni) with laser pulses of 70 mW laser power in air. The electron temperature was determined using the ratio method, which in the ranges of 0.34-0.44 eV, 0.28-0.42 eV, and 0.34-0.45 eV for Cu, Ti, and Ni respectively.

Khan et al, (2022) [23] employed the NELIBS technique to study the distinguishability of spectral lines. A colloidal of Cu NPs was generated by pulsed laser ablation in distilled water and dried on the Al surface. The study investigated with different laser intensity and NPs concentration in the unit area. The optimal NPs concentration and laser influence was 45 $\mu L/cm^2$, and 28.3 GW/cm^2 respectively.

Ahmed and others , (2023) [24] utilized an external electric field to enhance the signal intensities of emission lines and improve the limit of detection for gold alloys. Five different gold alloys were analyzed using Electric Field-Assisted Laser-Induced Breakdown Spectroscopy (EF-LIBS) technology. The EF-LIBS spectra contain emission lines specific to the constituent elements present in the samples. The intensities of emission lines are proportional to the concentrations of the elements. The laser-produced plasma was generated by focusing a laser with 100 mJ energy and a pulse duration of 5 nanoseconds.It is evident from this research that Electric Field-Assisted Laser-Induced Breakdown Spectroscopy (EF-LIBS) can be employed to enhance signal intensity and improve the limit of

detection for precious elements such as copper, silver, and gold. In the presence of an external electric field, the plasma acts as a current carrier when the external electric field reaches the threshold value of 49 V/mm. This effect induces a plasma re-excitation process, resulting in a significant enhancement of signal intensities .

1.3 Aim of this Work

This study aimed to study the plasma emission spectra of gold and silver nanoparticles and detecting the generated spectrum formed by the LIBS technique. The study also aimed to prepare nanoparticles experimentally using the pulsed laser ablation method, so that they could be used to enhance the efficiency of the solar cell.

Chapter Two

Theoretical Part

2.1 Introduction

This chapter includes the fundamental concepts of nanomaterials, their preparations, applications, laser-matter interaction, and plasma criteria. It also includes the fundamental nano-enhanced LIBS, structural properties, and the principle of using plasmonicnanomaterials in enhancing solar cells.

2.2 Pulsed-Laser Ablation

Numerous processes, such as chemical vapor deposition [25], hydrothermal [26], and PulsedLaser Ablation (PLA) [27] are employed to create nanoparticles. Among these techniques, PLA has certain advantages due to the simplicity of manufacturing different nanoparticles with the ability to control several parameters[28].

The PLA is a broadly used technique that is used for producing nanostructures from solid targets by ablation either gas or under vacuum. Pulsed-Laser Ablation in Liquid (PLAL), a novel chemical synthesis technique, offers a viable platform for the production of colloidal metal nanoparticles by a physical procedure. The surface characteristics of the PLAL nanoparticles set them apart from their chemically generated counterparts in a significant way. They are now desirable candidates for a wide range of exciting applications, including catalysis, biology, sensing, and the creation and storage of sustainable energy [29].

Laser ablation is the process of converting bulk materials into nanoparticles. Low laser power heated the sample by absorbing energy, which caused the target to vaporize. High-powered laser energy frequently transforms into plasma interaction with matter. The ablation technique was used to remove materials with a pulsed laser. The amount of material abated by a single laser pulse depends on a number of factors, including the laser's wavelength, power, pulse duration, and the target's optical absorbance [30].

Plasma appears near the target surface, where free electrons are accelerated by electromagnetic radiation to the threshold energy needed to ionize the atoms, forming additional atoms that assist in ionization [31]. The shock wave rapidly expands the plasma. A specific wavelength of radiation is released when the excited species descend during the cooling of the plasma[32]. Both scientific and commercial applications can greatly benefit from laser ablation [33]. Laser ablation is used to create nanoparticles in many different applications. This type of physical vapor deposition is a particular one [34][35].

A large number of studies conducted even in the field of generating nanoparticles by laser pulses of nanosecond pulse duration[36]. A pulsed laser is used to illuminate a metal plate immersed in a liquid under different wavelengths, pulse period, and different laser power [37]. Spherical NPs can be formed by aggregation of particles if the colloidal particle solution is suitable [38].

The PLA technology uses a high pulse power on the surface of the solid sample immersed in the liquid that makes the surface turn into a column of plasma containing particles with high kinetic energy, such as atoms, ions and electrons, which in turn condenses into nanoparticles. To produce atoms with high stability depending on the initial sample and the liquid, as the species in the column interact with the molecules of the surrounding liquid [39]. Depending on the laser flounce and time scales, the heat and time pressures within the interaction volume can be extremely harsh for milliseconds [40]. These high pressures and temperatures enable to produce materials with completely new properties [41].

2.2.1 Laser Matter Interaction

The laser-matter interaction occurs with different features according to different parameters such as the characteristics of the used laser (intensity, wavelength, pulse duration). It is also influenced by the irradiation method (incidence angle, laser spot area). In addition, the target type, geometry, and

surface morphology are potential parameters to improve the laser-matter interaction. Electrons are accelerated to high energies by the dynamics of plasma generation, which react with other species and causes photon emission. The LIBS can be enhanced by the existence of effective plasmonic NPs by enhancing laser absorbance, this addition produced sensitive diagnostic tools for elementary analysis [42].

The radiation-induced heating mechanism is mostly responsible for the interaction between the pulsed laser and the target surface material. Initially, this heat creates droplets of molten metal that heat the surrounding medium, causing it to evaporate. Very high and instantaneous pressure is generated in this region due to inertial confinement [43]. The pressure created by the vapor can raise the boiling point of a substance, allowing the extracted substance to remain in its liquid state even at a higher temperature than its boiling point. The shock wave is produced as a result of the sudden increase in pressure generated by the plasma, which causes the temperature of the laser-induced plasma to rise rapidly as shown in Figure[44].

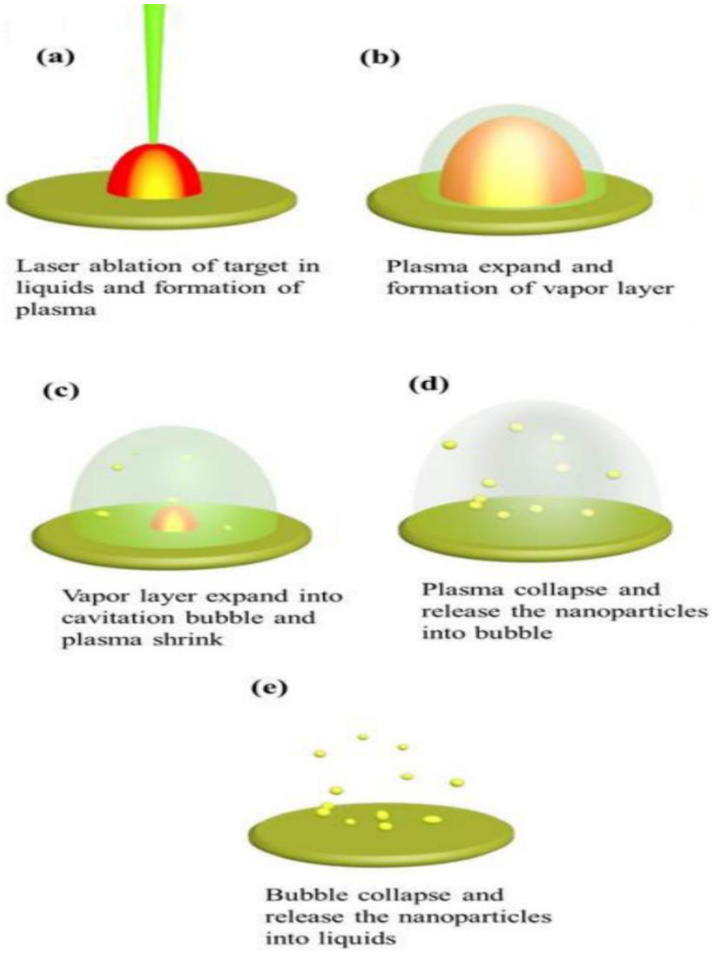

Figure 2.1 : Schematic of Plasma Matter Interaction Steps [48].

2.3Nano Materials

There are different ways of classifying nanomaterials. The size and shape of NPs are the most effects on their properties. So, The nanostructures can be categorized allowing a number of dimensions out of the nano-scale as three classes[45].

- Zero-dimensional nanostructures (0D): such as quantum dots.
- One-dimensional nanostructures (1D): such as nanorods.
- Two-dimensional nanostructures (2D): such as Graphene[46].

The characteristics of nanostructures are widelyaffected by the preparationmethod, procedure, and theirspecificparameters[47].

The preparation techniques of NPs can be classified according to the reaction type as chemical or physical methods. Two main approaches of nanomaterialscreation of top-down and bottom-up approaches, as illustrated in Figure 2.2 [48].

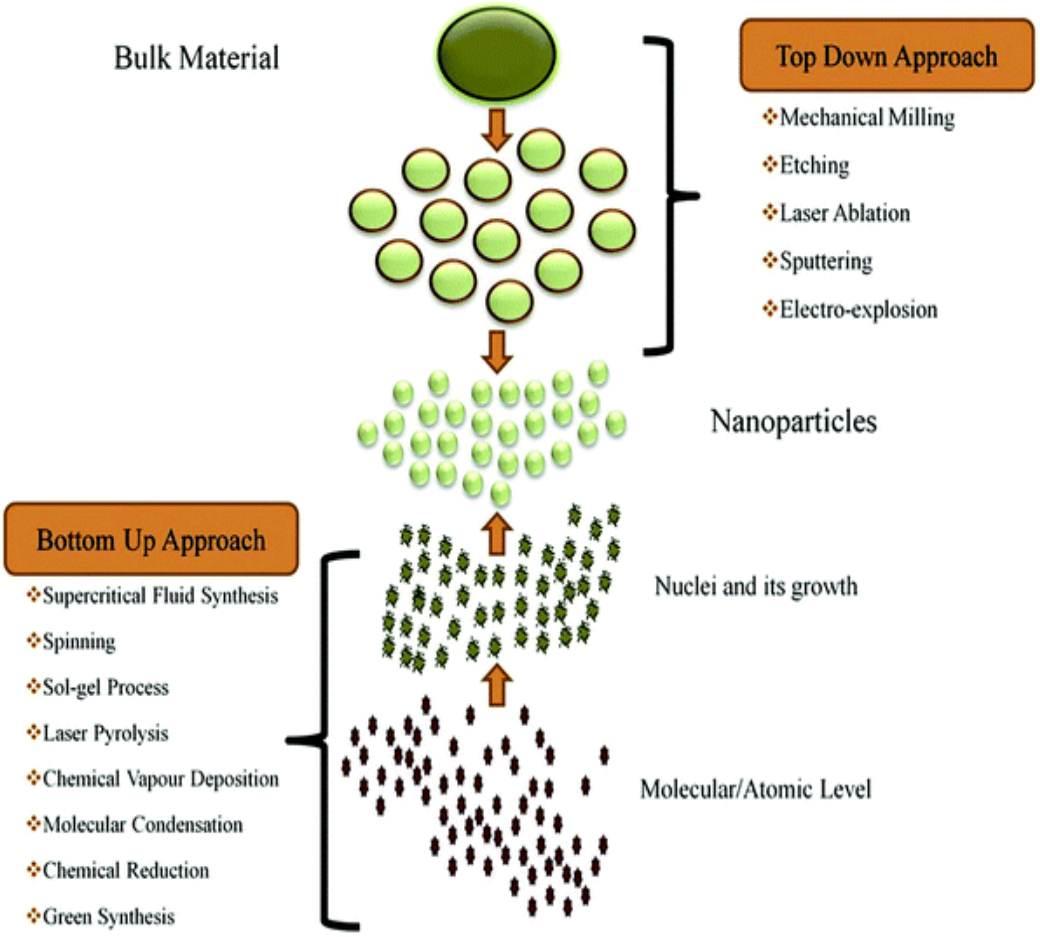

Figure 2.2 : The synthesis of nanomaterials via top-down and bottom-up approaches[49]

The "top-down" strategy requires separating bulk materials in order to generate the nanostructures. While the "bottom-up" one, involves collecting individual molecules or atoms to form nanostructures[49].

The well-known method of the PLA technique is one of simple way to prepare nanoparticles from various materials. At low laser flux, the material is heated by the absorbed laser energy and evaporates or sublimates. At high laser flux, the

material is typically converted to a plasma. A beam of pulsed laser has high-power is directed onto the target during PLA, causing small explosions and particle ejections near the target. The generated nanostructures are collected for additional analysis. Particularly, the properties of the generated nanostructures can be tuned by changing the plasma characteristics. The nanosecond pulsed laser can heat and thermally damage the processed material, but an ultra-short laser of femtoseconds causes minimal material damage. The depth over which the laser energy is absorbed, and thus the amount of material removed by a single laser pulse, depends on the material's optical properties and the laser wavelength and pulse length[50].

2.3.1 Applications of Nanoparticles

Nanomaterials are used in many fields with a variety of applications, including those related to medicine, such as drug delivery for therapy to specifically target tumors to reduce side effects on other organs [51]. Microbial sensing can also be applied using carbon nanotubes [52]. Mineral NPs are widely applied in cosmetics as a mask against exposure to harmful UV rays[53].

Nanomaterials are also used in many military applications such as military sensors based on nanomaterials such as TiO_2nanoparticles[54]. Nanomaterials are also used in selective solar absorption applications to be able to absorb heat over a widespread range of wavelengths while reducing emissions much more efficiently than bulk samples [55]. The use of nanomaterials is widespread in pharmaceutical and medical fields, including photodynamic therapy of tumors [56], drug delivery [57], tissue regeneration [58], biosensing[59], and DNA structure research [60].

2.4 Gold Nanoparticles

Gold (Au) is a chemical element has atomic number 79. It is a bright metallicyellow, dense, soft metal in pure form. Au is resistant to most acids. The Au exist as face centered cubic structure, and each unit cell contains 4 atoms as shown in Figure (2.3).

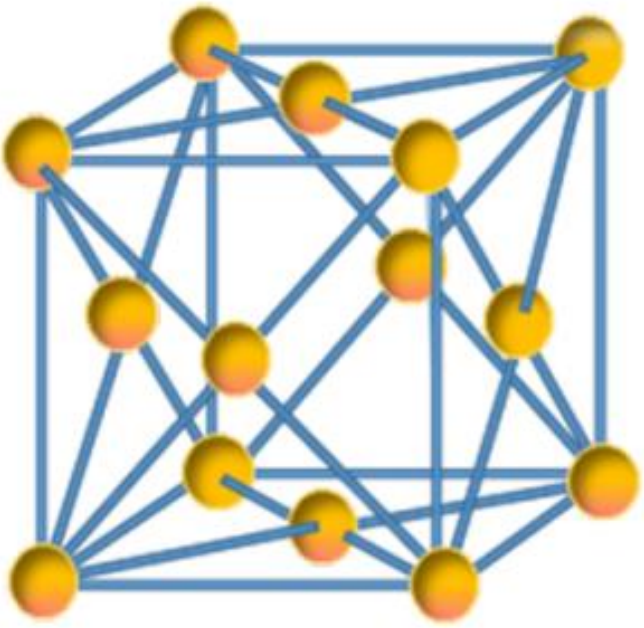

Figure 2.3: Unit Cell of gold crystal is consists of four atoms[61].

The Au can simply convert into nanoparticles by different technique including chemical, and physical routes. The gold nanoparticles (Au NPs) have attracted more attention in many scientific and application fields owing to their unique characteristics, such as electrical conductivity, low toxicity, and modifiable size to control their optical properties, biocompatibility, and chemical stability which depends on the size. The practical use of nanoparticles in medical use is according to high stability and biocompatibility in the solution, since NPs are transported through canals in aqueous systems. The Au NPs can characterized by different techniques such as electron microscope and UV-Vis absorbance. The Au NPs exhibits strong absorbance in the visible region wavelengths within the range of 500 nm to 600 nm depending on the size of the particles [61].

2.5 Silver Nanoparticles

Silver (Ag) is a chemical element has atomic number 47. A soft, silver, lustrous transition metal, it exhibits the highest electrical and thermal conductivity. The metal is found the Earth's crust as an alloy or minerals. Ag has a completely

filled 4d orbital ($4d^{10}$ $5s^{1}$) in its ground state. So, Ag displays two oxidation states (+1 and +2)[62].

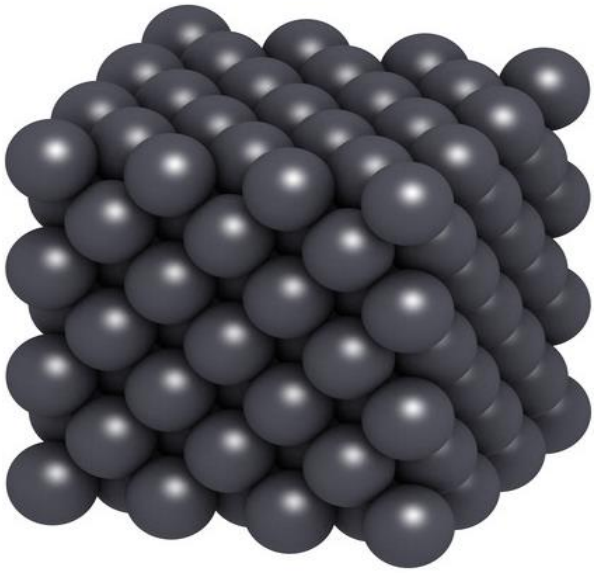

Figure2.4:Atomic Arrangement of Silver Atom in their Crystal Structure[63].

Nano-silver (Ag NPs) show different physical, chemical and optical properties compared with their bulk form. The optical property of Ag NPs is size and shape dependent. Ag NPs used for different application purposes as its properties of the SPR which employed in numerous application such as optical fibre sensor based on localized SPR using Ag nanoparticles, DNA detection by surface-enhanced Raman scattering (SERS) [63].The Ag NPs are promising bactericidal agents and plasmonic NPs for environmental applications, owing to their various favorite properties. For example, the Ag NPs generates reactive oxygen species (ROS), the SPR and specific reaction selectivity [64].

2.6 Surface Plasmon Resonance

The Plasmon effect is a resonant interaction between an electromagnetic wave of a certain frequency that corresponds to the oscillation frequency of the cloud of electrons confined in metallic nanoparticles with a size smaller than the

electromagnetic wavelength [65]. The local field present in and around the particle is amplified via harmonic resonance, this phenomenon has been explained by many theories as scattering centers of light [66]. The ability to modulate the electromagnetic wave allowing the size, shape and composition of nanoparticles makes this phenomenon attractive for a large number of studies. As a result, it can be controlled using metal alloy nanoparticles depending on the component ratio or as a basic design for the shape and size of the nanostructures[67].

The science of nanomaterials began with the first observations in 1802, when Richter discovered that continuous grinding of gold would turn it into a violet powder. This change was explained by its transformation from large size to nano size without changing the substance. It was concluded that due to the refraction of the light the very fine gold particles changed color[68]. Since the scattering of a particular wavelength of incident light by the nanoparticle is smaller than the wavelength of the light, the result is an electron dipole oscillation within the particle called the plasmonic frequency[65], as shown in Figure 2.5.

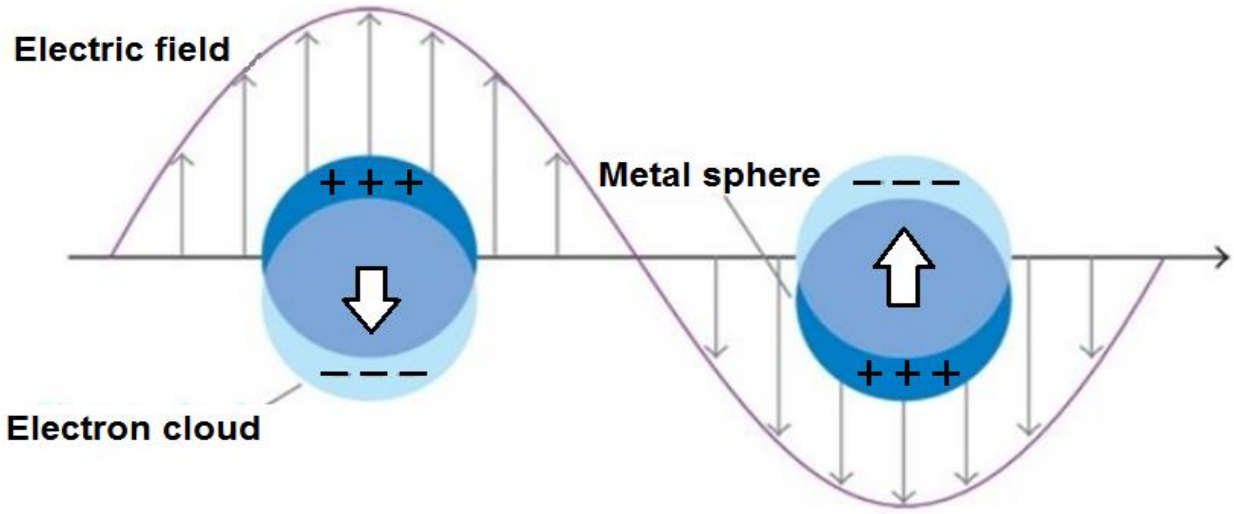

Figure 2.5:Schematic of Surface Plasmon Resonance ofConfined-Electrons with an External Electromagnetic Radiation[69].

Plasmonic metallic nanoparticles efficiently scattered light at a specific frequency. By adjusting the size and form of NPs, the frequency responsivity can be controlled across the electromagnetic range. As a result of shifting the

absorption edge, the NPs dispersions also changed. As an illustration, solutions containing gold NPs have a ruby-red hue due to a strong scattering in the green region, but solutions containing silver NPs have a yellow color coming from the plasmonic band in the blue range[70].

These constrained oscillated charges considerably strengthen the local electric field both inside and outside the particle. This resonance predominates as a result of nonlinear or linear response. The plasmonic band can be controlled by a many concepts such as the fundamental characteristics of the composition contents, particle size, and configuration[66].

2.7 Laser Induced Breakdown Spectroscopy

Recently, Laser-Induced Breakdown Spectroscopy (LIBS) technique has concerned high attention in numerous studies in different fields such as medical applications [71].A pulsed laser is used as an excitation source in a technique of spectroscopy of atomic or molecular components known as the LIBS. By examining the laser-induced plasma emission spectra, specific atomic or molecular components are identified. This technique is used for any substance whether it is solid, liquid or gas [72]. The only limitations are the laser output power and the wavelength used for the detector. The LIBS works mainly by focusing the laser beam on a small area on the surface of the sample, which leads to ablation and the formation of a plasma column due to the high temperatures that ionize the atoms of excited ionic and atomic species, which emit specific radiations after de-excitation process[73].

The LIBS can be applied at different environmental conditions [74]. Plasma reactions during the irradiation are highly dependent on the surrounding media, and pressure, in addition to laser parameters such as laser flounce, wavelength and its pulse duration [75].A typical LIBS system includes a Q-switched laser, optics to

focus the laser light on a sample and another to collect the emitted light, a high-resolution spectrophotometer, and a computer to control the system and to record the data, as shown in Figure 2.6 [76].

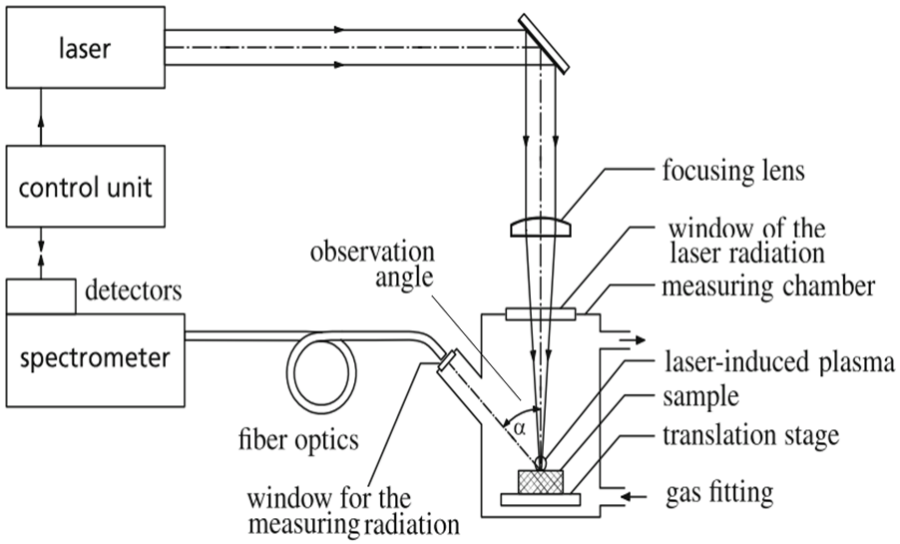

Figure 2.6: A Schematic of Typical the LIBS System[77].

2.8 The Improvement by LIBS Technique

The electromagnetic energy of light striking an object is greatly amplified when a bulk sample is replaced by a nanoparticle. The existence of metallic nanostructures under laser irradiation cause to rise the local electromagnetic field of the incident light [78]. Conduction electrons in metallic nanoparticles oscillate constructively when exposed to an electromagnetic wave such as a laser pulse, which leads to enhanced breakdown and plasma generation. This technique is known as the LIBS and NELIBS. The electromagnetic fields around the outer layer of the particle are strengthened, making it possible to efficiently generate the primary electronic seeds needed to generate plasma via field emissions of electrons, creating the potential for direct electron emission at the surface. The Keldysh parameter (γ) determines the type of interaction between the laser and the material that leads to ionization of the atoms through the phenomenon of tunneling the work function either through the field emission or photon absorption processes

[79].

$$\gamma = \omega \frac{\sqrt{m_e V_B}}{eE} \quad \text{.....(2.1)}$$

where V_B is the work function, E is the electric field intensity, ω is the laser frequency .If γ> 1, the ionization occurs by photons absorption, while, if γ< 1, the field emission is the main mechanism of ionization .The ionization process changed to electron field emission by increasing the electromagnetic field irradiation.

The main reason for the coupling of the endodontic is the generation of seed electrons. As a result of sample heating and electron acceleration caused by laser irradiation, more electrons are emitted through field emission phenomenon, which greatly increases the effectiveness of avalanche induction and electron excitation. The G_{OES} factor is used to determine the theoretical ratio between the two intensities for the emission of the NELIBS and LIBS:

$$G_{OES} = \frac{I_{NELIBS}}{I_{LIBS}} = \frac{N_{0,NELIBS}}{N_{o,LIBS}} \frac{Z(T_{LIBS})}{Z(T_{NELIBS})} \; exp\left[\frac{E_j}{k_\beta}\left(\frac{1}{T_{LIBS}} - \frac{1}{T_{NELIBS}}\right)\right] \text{..... (2.2)}$$

The generation of the seeds electron is the crucial step for plasma initiation by laser-induced. The NPs surface plasmon assist right free electrons generation by field emission, which reduce the break down threshold and creates significantly denser plasma [78]. Figure 2.7 shows schematically the laser mater interaction with the existence of NPs.

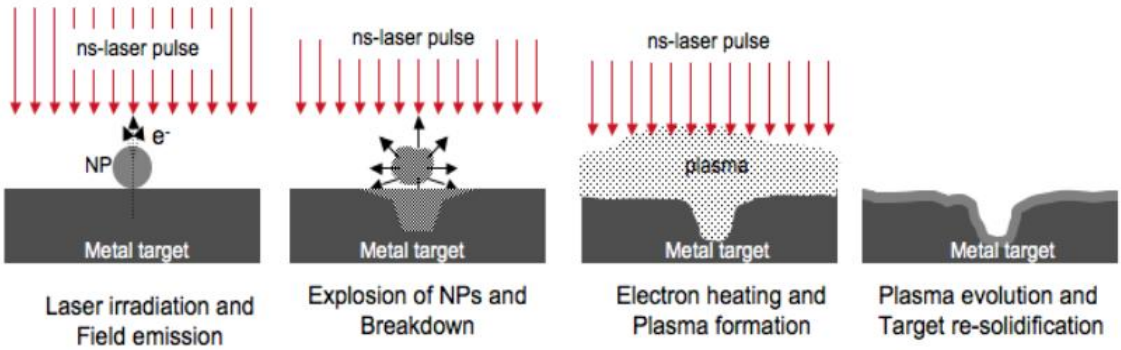

Figure 2.7: Laser matter Interaction NPs [78].

The surface, diameter, and concentration of NPs are the main factors that determine how effective the nanoparticle enhancing process. There are an optimum inter- distance between NPs (d), and their diameters (D) of largest field improvement which cause optimal enhancement of the plasma generation. Decreasing the distances between than its optimal point can decrease the growth in the induced plasmon field [80].

2.9 Plasma Criteria

Plasma is a non-dimensional medium that has a quasi-neutral character, although it contains many positively or negatively charged particles and neutral particles, and it performs as collective behavior. Plasma is described as the fourth state of matter because it appears after giving enough additional energy to the gas to ionize part of its atoms [81]. The state of plasma differs in its characteristics radically from the gaseous state, as plasma has a good conductivity of electric current as a result of its possession of free charges that act as a conductor of electric current. The Plasma interacts with electric and magnetic fields due to the Coulomb force and the Lorentz force due to the presence of moving charges within the plasma. The plasma also interacts with electromagnetic waves within certain frequencies that correspond to the internal frequencies of the plasma[82].

Cold and hot plasma can be distinguished from each other based on plasma parameters including density and average kinetic energy of the particles. The classification of plasmas based on electron temperature and density is shown in Figure 2.8. Cold plasma contains only a small percentage of ionized gas atoms. In this case, the electron temperature is much larger than the ion temperature which in turn is much larger than the gas temperature ($T_e >> T_i >> T_g$). While in the hot plasma the electron temperature (T_e) and the ion temperature (T_i) are close in values($T_e \approx T_i$) [83]

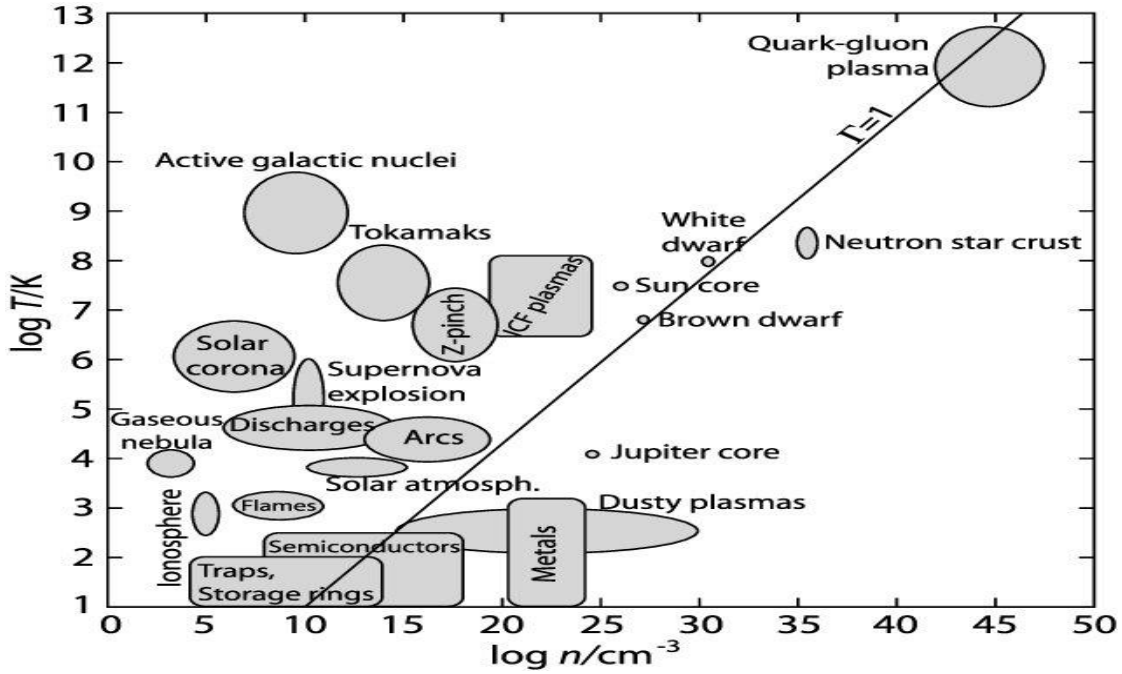

Figure 2.8: Types of Plasma with Different Plasma Temperature Electron Number Density[81].

Owing to complexity of plasma, there are different models for understanding the plasma characteristics, such as particle motion or can be described as fluid [84].

The shielding of an external electric field on the plasma causes the nearby charged particles rearrange themselves, which leads to the generation of an opposite field that blocks the field. If charge is immersed within the plasma, the charges accumulating around it act as a shield to block the field over a short distance. The thickness of the sheath, or as defined by the Debye length ($\boldsymbol{\lambda_D}$), is the distance over which the electric field is shielded[85].

$$\boldsymbol{\lambda_D} = \sqrt{\frac{\boldsymbol{\varepsilon_0 k_B T_e}}{\boldsymbol{n_e e^2}}} \quad \text{..... (2.3)}$$

The first plasma criteria say that the geometrical size of the plasma (L) should be much greater than the Debye length ($L >> \lambda_D$), to achieve the quasi-neutrality.

The second plasma condition states that there must be many electrons inside a "Debye sphere" to fulfill the collective behavior condition:

$$N_D = \frac{4\pi n_e}{3}\lambda_D^3 \gg 1 \quad \text{..... (2.4)}$$

The third condition states that electromagnetic forces must be more dominant in the motion of particles than that caused by collisions. That is, the electrons must complete many oscillations inside the plasma before they collide with other species. The electron frequency inside the plasma is calculated from the following relationship [85]:

$$\omega_{\mathrm{p}} = 2\pi f_p = \sqrt{\frac{n_e e^2}{m_e \varepsilon_0}} \quad \text{(2.5)}$$

where m_e is the electron mass .

2.10 Optical Emission Spectroscopy (OES)

To understand the properties of the plasma, it is important to characterize the plasma parameters to understand their effect on the morphology of the plasma nanoparticles, their effect on the surface configurations [86][87]. Imaging, thermography, mass spectroscopy, ion probes, optical absorption, interferometry, and electrical probes are some of the methods used in plasma diagnostics. The OES method can be considered as the simplest and most effective method for plasma diagnosis. This method uses emissions from reactions within the plasma to characterize the plasma [88]. By striking a target surface with a high-power laser beam and ionizing the material, plasma is generated. Therefore, after the laser photons reach the target, the plasma emits a variety of spectral emission [89].

The dominant emitted lines from plasma corresponding to electronic transitions in atomic or ionic electronic species [90].

According to the assumption of local thermodynamic equilibrium, the intensity distribution of the spectral lines will obey Boltzmann distribution principle. So, the plasma temperature (T_e) is overrule the existence states in each level. In addition, the probability of transitions (A_{ji}), and the statistical weight of the excitation level (g_j) also effect the line intensity, as: [91].

$$I_{ji} = \frac{N}{U(T)} g_j A_{ji} h\upsilon_{ji} e^{-E_j/k_\beta T_e} \quad \text{(2.6)}$$

where $E_j$is the upper level energy. By taking the natural logarithm for both sides, this relation converted to so called Boltzmann-Plot [92]. The plasma temperature can determine from this equation, using the intensity of emitted lines of a selected species, from the slope of the linear relation between left hand side against the upper level energy [93]:

$$ln\left[\frac{\lambda_{ji}I_{ji}}{hcA_{ji}g_j}\right] = -\frac{1}{kT}(E_j) + ln\left|\frac{N}{U(T)}\right| \quad \text{(2.7)}$$

where: λ_{ji} and I_{ji} are the wavelength and line intensities. *N*and *U(T)*represent the density of states of the emitted species, and partition function, respectively.

The electron number density (n_e) can determine according to the Saha-Boltzmann equation, using atom and ion spectral lines [94].

$$n_e[cm^{-3}] = \frac{I_Z^*}{I_{Z+1}^*}\ 6.04 \times 10^{21}(T)^{3/2} \times exp\left[\left(-E_{k,z+1} + E_{k,z} - \chi_z\right)/k_\beta T\right] \quad \text{(2.8)}$$

where $I_z^* = I_Z \lambda_{ki,Z}/g_{k,Z}A_{ki,Z}$ and χ_z is the ionization energy of the species.

It also can be determined employing Stark broadening effect from the emitted line width ($\Delta\lambda$), which can write in a simple form [95]:

$$n_e = \left(\frac{\Delta\lambda}{2\omega}\right) \times N_r \quad \text{(2.9)}$$

Whereω , and N_r represent the electron impact factor and electron density from previously determined data for a specific transition, respectively.

2.11 Solar Cells

The world is searching for renewable energy sources on a large scale to develop environmentally acceptable technologies in order to meet the energy needs of the world. One of the most important applications of renewable energies is photovoltaic cells, which are of global interest for their ability to generate energy

for a variety of fields using solar radiation available in many countries [96].

An electric current is generated within the depletion region near the junction by photon absorption, which generates an electron-hols pairs. In order to leave the depletion region, the free electron and hole have enough energy. Electrons will flow through a wire if it is bridged between the anode and the cathode. As it passes through the external load it attracts the electron to the positive pole of the P-type material and generates an electric current while the gap moves to the back electrical contact by drawing it to the negative charge of the N-type material.

2.11.1 Solar Cell Parameters

In an ideal cell, the total current I is equal to the current Iℓ generated by the photoelectric effect minus the diode current I_D, according to the equation:

$$I = I_l - I_D = I_l - I_o\left(e^{\frac{qV}{KT}} - 1\right) \quad \text{(2.10)}$$

where I_0 is the saturation current of the diode, q is the elementary charge, k is a Boltzmann constant, T is the cell temperature, and V is the measured cell voltage. While, an accurate model includes diode model as the following equation[96]:

$$I = I_l - I_o\left(e^{\frac{q(V-I\,R_S)}{nKT}} - 1\right) - \frac{V+I\,R_S}{R_{Sh}} \quad \text{(2.11)}$$

Where, R_S and R_{SH} represents the equivalent series and shunt resistances. Figure 2.9shows an equivalent circuit for a photovoltaic device[97]

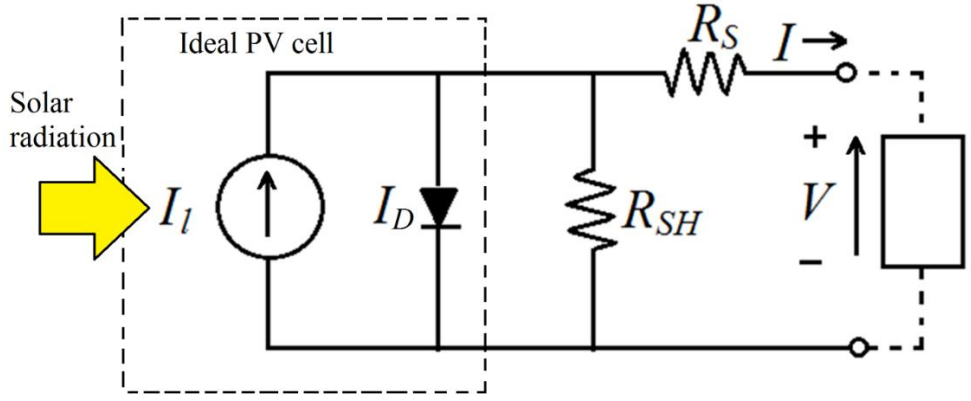

Figure 2.9: A Simple Representation of Solar Cell [97].

The I-V curve of an illuminated PV cell has the shape shown in Figure 2.10 as the voltage across the measuring load is swept from zero to V_{OC}, and many parameters for the cell can be determined from this cure.

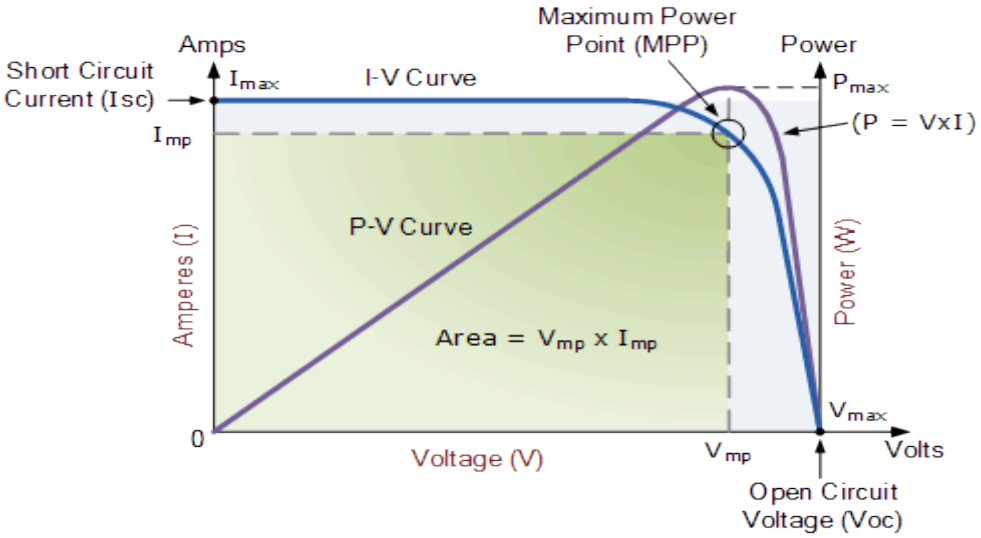

Figure 2.10: I-V and P-V Curves for a Solar Cell[98].

The power delivered by a solar cell is the product of current and voltage ($I \times V$). When the solar cell is not connected to any load, the voltage across the cell called as the open circuit voltage (V_{oc}). While, when the solar cell is short circuited, the current flowing out of the cell reaches its maximum called as circuit current (I_{sc}). The point at which the cell generates maximum power atI_m and V_m.

The fill factor is the relationship between the maximum power over the product of the open-circuit voltage times the short-circuit current[99].

$$FF = \frac{I_m V_m}{I_{SC} V_{oc}} \quad \text{.....(2.12)}$$

The efficiency of a photovoltaic cell is the ratio between the maximum produce electrical power over the incident irradiance power on the cell[99].

$$\eta = \frac{I_m V_m}{P_{in}} \times 100\% \quad \text{.....(2.13)}$$

2.11.2 Plasmonic Solar Cells

Numerous strategies for capturing photons had been put forth by studies, such as the use of anti-reflection coatings [100], grids in windows, photonic crystals, and plasmonic effect of metal nanoparticles [101]. The Plasmonic NPs had served as the foundation of numerous studies utilizing the aforementioned methods[100]. The plasmonic method is, in fact, among the greatest methods for improving localized light absorption [102].

Metallic nanoparticles with the LSPR support operate as a light trap because of the interaction between the confined charge inside the particle and the incoming light, which resulted in a scattering effect [103]. The LSPR can boost the solar conversion efficiency by generating a strong electromagnetic field on the metal NPs surface, which in turn increases the absorption of the active layer in the visible range of wavelengths[104].

The addition of metallic nanoparticles enhances the solar cell efficiency by the LSPR effect, a shift in the Fermi level, a rapid injection of electrons into semiconductor materials, and accelerated charge separation generated by the electromagnetic field [105].

The two primary categories of light-trapping methods are extending the optical path inside the cell and lowering the reflection coefficient of the top surface. Increasing absorption has an effect on the lower recombination rate, higher open circuit voltage, and higher conversion efficiency [106]. In order to collect more incident light, Au and Ag NPs dispersed on the surface may also function as an efficient scattering element. As a result, surface has significantly increased light harvesting, thus, it is possible to get a larger short circuit current density , thus greater efficiency[107].

2.12 Structural Properties of Nanomaterial

Several techniques are employed to characterize the basic properties of nanomaterials. One of the important properties that have a close relationship with other physical properties is the structural properties. The study of structural properties makes it possible to know many basic characteristics, such as degree of crystallinity, phase, crystal size, and strain. According to Bragg's law, when monochromatic-wavelength of X-rays fall on a crystalline material at a certain angle, the angle of diffraction of the radiation (θ) depends on the separation distances between the lattice planes (d_{hkl})[108].

$$n\,\lambda = 2\,d_{hkl}\,sin\,\theta \quad \text{..... (2.14)}$$

while, the crystallite size can determined according to the diffraction line breadth (β) as shown by Debye-Shcerrer's formula [109]:

$$D = \frac{0.9\,\lambda}{\beta\,.cos(\Theta)} \quad \text{..... (2.15)}$$

The lattice constant (a) for cubic structure can calculated according to the relation [110]:

$$a = d_{hkl}\sqrt{h^2 + k^2 + l^2} \quad \text{.....(2.16)}$$

Chapter Three

Experimental Work and Procedures

3.1 Introduction

This chapter introduced the experimental work steps and techniques for the preparation and diagnosis of metal nanoparticles by PLAL technique, and laser-induced plasma from bulk and nano enhanced targets. It is also includes the procedure for applying the prepared nanoparticles to enhance a solar cell and how to characterize the photovoltaic cell specifications. Figure 3.1 shows the schematic of experimental steps.

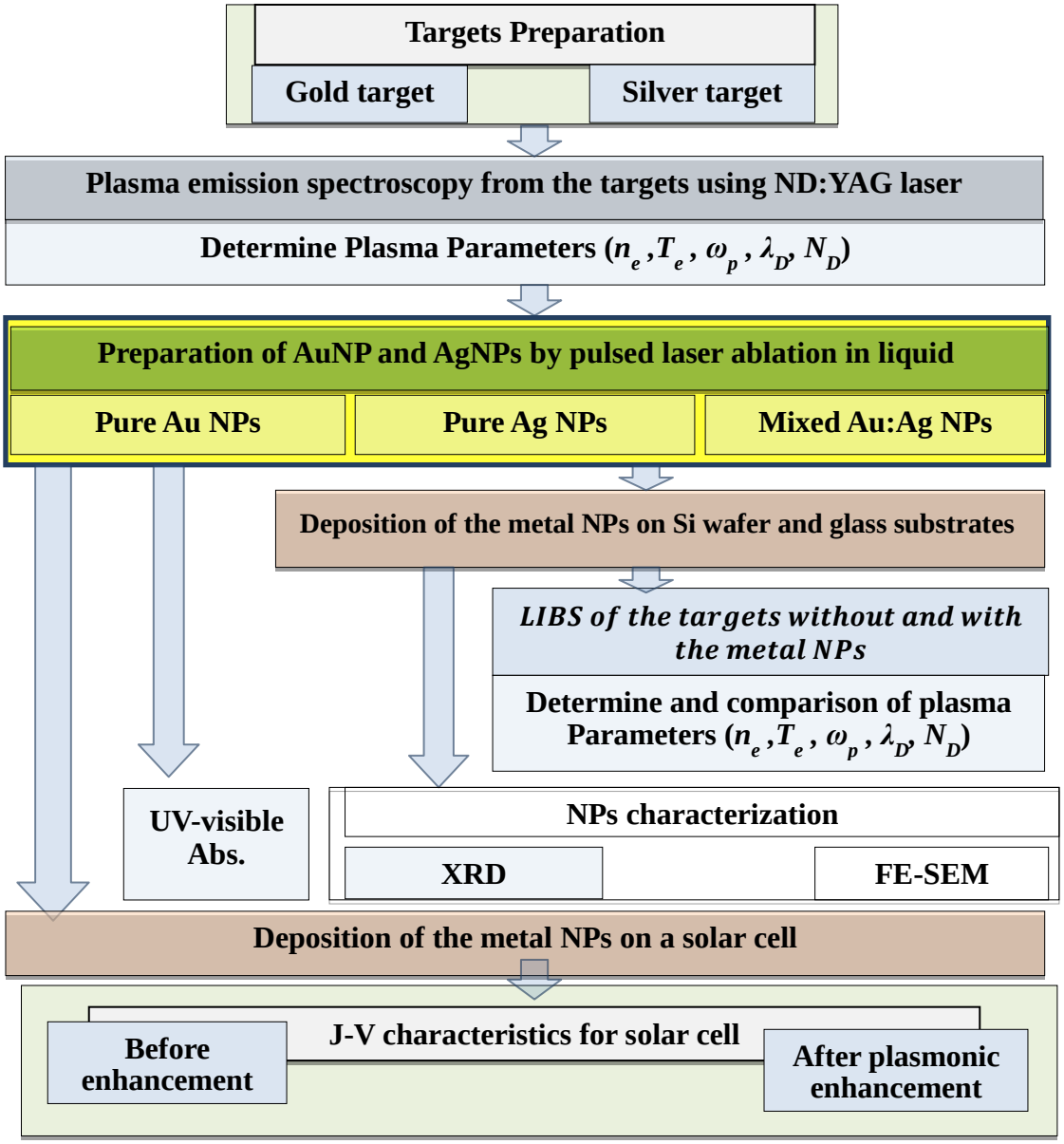

Figure 3.1: Schematic Diagram of the Experimental Steps.

3.2 Materials

The materials used in this work to prepare nanoparticles, and to examine the nano enhanced the LIBS employing these metal nanoparticles are listed in Table 3.1.

Table 3.1: Chemical Material and their Origin.

Gold plate	
Chemical formula	Au
Appearance	Golden plate
Purity	99.9%
Silver plate	
Chemical formula	Ag
Appearance	Gray plate
Purity	99.9%
Silicon wafer	
Chemical formula	Si
Appearance	Front Surface: Polished; Back Surface: Etched
Roughness	< 0.5 nm
Orientation:	[100]
Type/Dopant:	P-type /Boron dopant
Company	Alpha Nanotech
Glass slides	
Chemical formula	Soda-Lime glass
Appearance	Transparence glass

3.3 Target preparation

The target samples prepared from high purity99.9% of the gold and silver plates of 4 mm thickness as shown in Figure 3.2. The targets were treated as follows:

1-The surface of the samples was polished by three polishing steps.
2- The targets surface were cleaned by vibrating with ultrasound in acetone for 15 minutes.
3- The above targets were cleaned by ultrasonic vibrator in distilled water for 15 minutes.
4- The samples are dried by blowing the air.

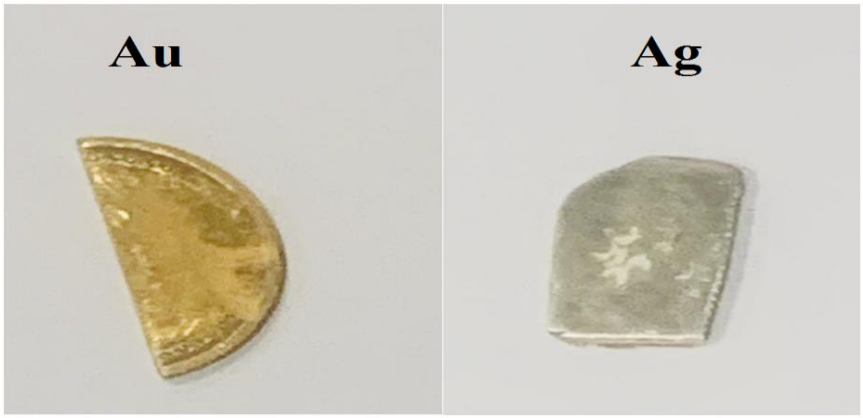

Figure 3.2:The Targets are the Au and Ag using in this work.

3.4 Plasma Emission Spectroscopy

The laser-induced breakdown spectroscopy (LIBS) set up comprise of a Q-switched Nd:YAG laser source, and a spectrometer connected to computer for data collection.

3.4.1 Laser Source

Q-switched Nd:YAG laser has a fundamental wavelength of 1064 nm (Sigma Aldrich, Germany), 10 ns pulse duration, and 4 Hz pulses repetition was used as a source for the LIBS experiment. The laser beam is focused onto the target's surface utilizing a quartz lens at its focal length of 10 cm to reduce the incoming spot

diameter from 5 mmat the laser head to 0.027 mm on the sample.

The device consist of an external handy piece, power supply, controller, and cooling system using distilled water. The used pulsed laser energy in this work was100 mJ.

3.4.2 Spectrometer

Optical emission spectroscopy diode-array type (Spectra View 2100 from Korea Materials & Analysis Corp.) was used in plasma diagnostics. It is a fast technique of low power requirements with a charge coupled device (CCD) array detector. The emission light from the plasma is collected by the spectrometer and the spectral information is sent to the spectrometer. It is dispersed via a fixed grating across a linear charge-coupled device (CCD) array detector. The A/D converter transforms the analog data collected from the spectrometer into digital information. This is passed to the software, providing the user with application-specific information. The data are visualized using Visual Spectra 2.1 software. Figure 3.3 displays Spectra View 2100Located at the University of Babylon/College of Science for women/Nano Laboratory. Table 3.2 lists the specification of the spectrometer.

Table 3.2: The Specification of Spectra View 2100Spectrometer.

Wavelength range	400 nm ~ 850 nm (Visible only)
Resolution	1.2 nm (25㎛ slit)
Sensor	Silicon Charge Coupled Device (Si-CCD)-2048 pixels
Grating	600 lines/mm
Physical dimension	35 x 98 x 250 mm
Integration time	12~13 scans/second (with Pentium 133 MHz)

Figure3.3:Spectra View 2100Spectrometer.

3.4.3 LIBS Procedure

The pulsed Nd-YAG laser has a fundamental wavelength of 1064 nm, a pulse width of 10 ns, and a negative specificity factor switch, and pulse laser energy of 100 mJ was employed in the LIBS method, which was created to detect the generated plasma emission spectra. The laser pulse was focused on the sample using the fluorescence lens, with a focal length of 10 cm into 0.027 mm spot diameter.

The target was situated inside the sample holder at the focal point of the lens. The optical fiber was positioned and configured so that it made an angle of 45° with the laser axis at a distance of 5 cm from the sample. The aperture of the optical fiber has a diameter (NA = 0.22/200 m), and the a lens at the intake of the fiber gathers and concentrates the plasma emission into it. The plasma emission fibers are then presented to the slit within the spectrum analyzer model (Spectra View 2100), using a silicon Charge-coupled device (Si-CCD), which consists of a number of detectors to record spectral lines with (600 Lines/mm) notches. The detected light turned into digital signals. The spectra was captured with a 0.8 nm precision spanning at the wavelength range of (200-900) nm as. The accuracy of all spectrum data was checked using the National Institute of Standards and Technology (NIST)database.

Next, the application (Visual Spectra 2.1) transforms the digital signals, and detects the spectral lines of the materials inside the target. The spectra was captured with a 0.8 nm precision spanning the wavelength range of (200-900) nm. The accuracy of all spectrum data was checked using the NIST data base. The experimental arrangement is shown in Figure 3.4.

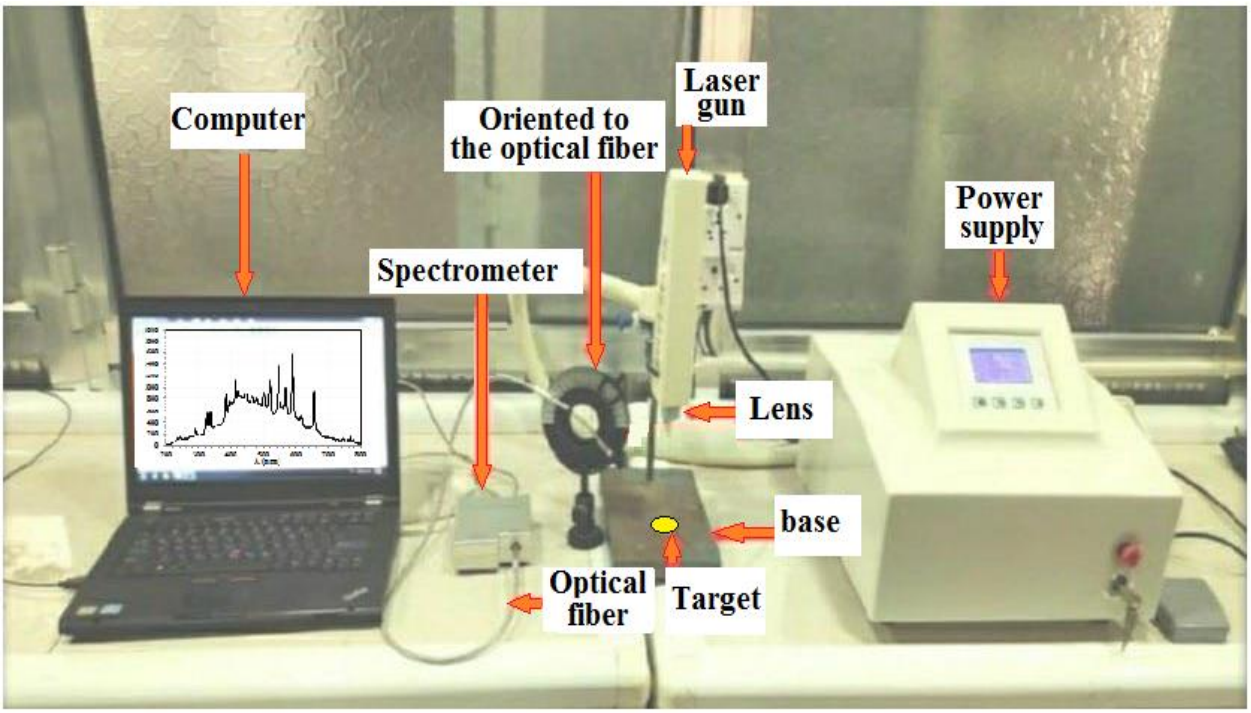

Figure 3.4: Experimental Arrangement of The LIBS Process.

3.4 Pulse Laser Ablation in Liquid

The nanoparticles were created the Au and Ag NPS through the process ablation using Nd:YAG laser ablation in distilled water at different number of pulses(200, 400, 600, and 800 pulse) at 100 mJ energy, 1064 nm wavelength,10nanoseconds pulse duration, and 4 Hz repetition frequency. The setup was shown in Figure 3.5. The colloidal in waterwas synthesis the color of water turned into purple color of the Au NPs and yellow of the Ag NPs, as shown in Figure3.6.

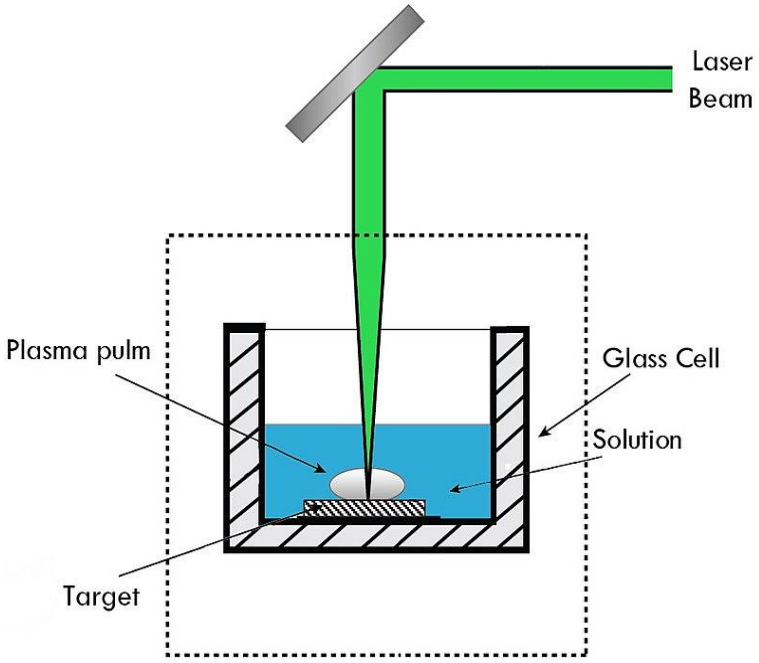

Figure 3.5: Laser ablation in liquid setup.

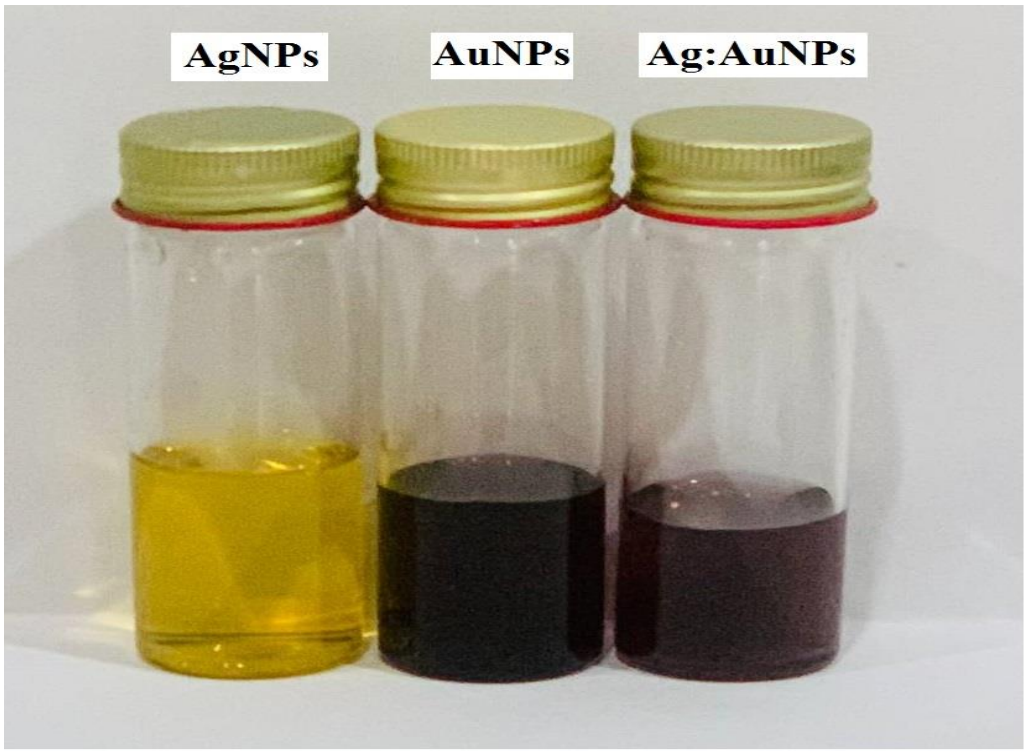

Figure3.6: the images of Nanoparticles Colloidal at 600 pulse.

The prepared the Au NPs and Ag NPs samples were mixed into different mixtures ratio as shown in Figure 3.7.

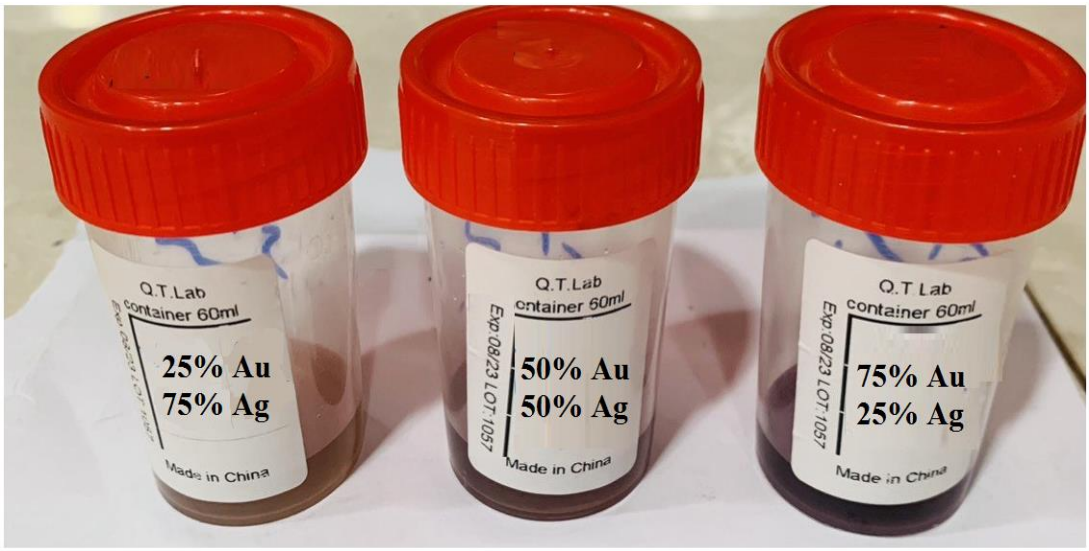

Figure 3.7: The Mixed AuNPs:AgNPs Samples at Different Ratios.

3.6 Deposition of Nanoparticles

After preparing the nanoparticle solutions, the suspension samples of the Au NPs, Ag NPs, and their mixture at different ratios were deposited on glass substrates and other time on silicon wafer substrates (n-type silicon wafer of (100) orientation was cut into 15×15 mm2 dimensions and cleaned processed) using dip-coating technique using the devise (PTL-OV6P, MALAYSIA, INDONESIA) as in Figure 3.8. The base is immersed in the solution for 120 seconds and extracted in 60 seconds at a temperature of 80 °C. This cycle was repeated five times to obtain homogeneous deposition of gold nanoparticles on the glass and Si. The final sample for Au NPs/Si and Ag NPs/Si were shown in Figure 3.9.

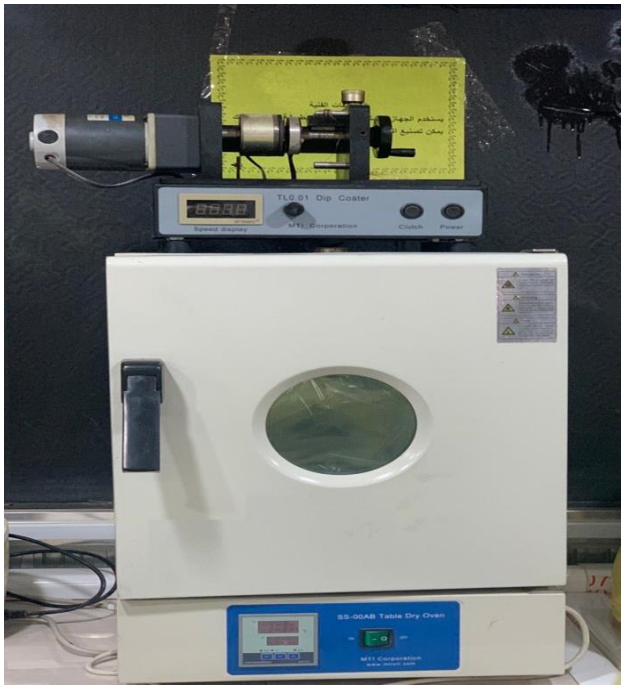

Figure 3.8: Dip-Coating Device.

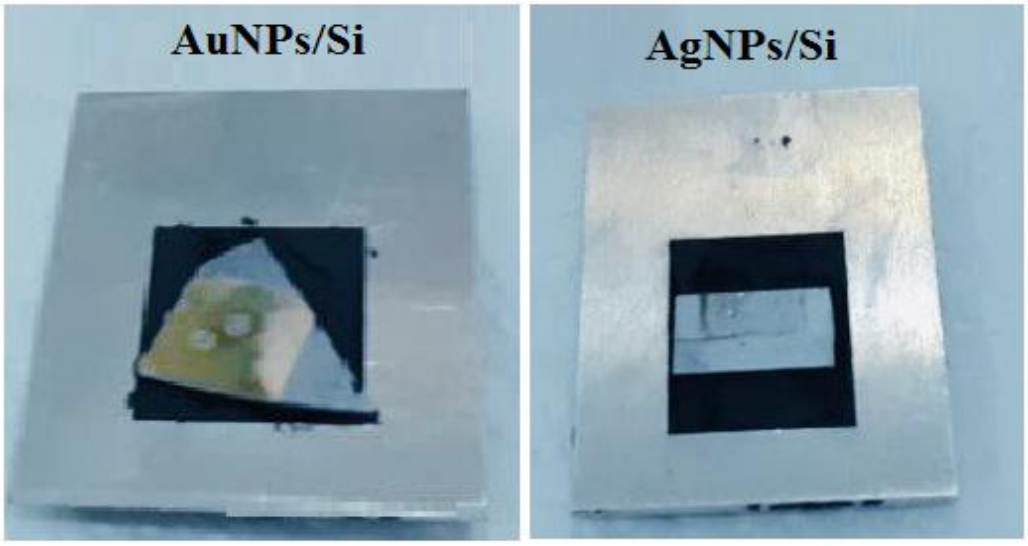

Figure 3.9:Deposited Samples.

The thickness of the prepared films was measured by the interferometer method, and the thickness was 220 ∓10 nm for all samples.

3.7Characterization and procedures of Nanoparticles

Many techniques are used to characterize the prepared metal nanoparticles which include : structural properties, surface morphology, and optical properties:

3.7.1 Structural Properties

The structural Properties of the prepared nanoparticle samples deposited on Si wafer were examined using the X-ray diffraction(ADX-2700 X-ray Diffraction ,USA)illustrated in Figure 3.10 Located at the University of Kufa /College of Science. A mono chromatic wavelength of 1.5405 Å wavelength corresponding to $Cu_{k\alpha}$electronic transition using 30 mA current and 40 kV high voltage power supply. The diffraction angle (2θ)within the range (20°-80°) at speed of 5.00 (degree /min).

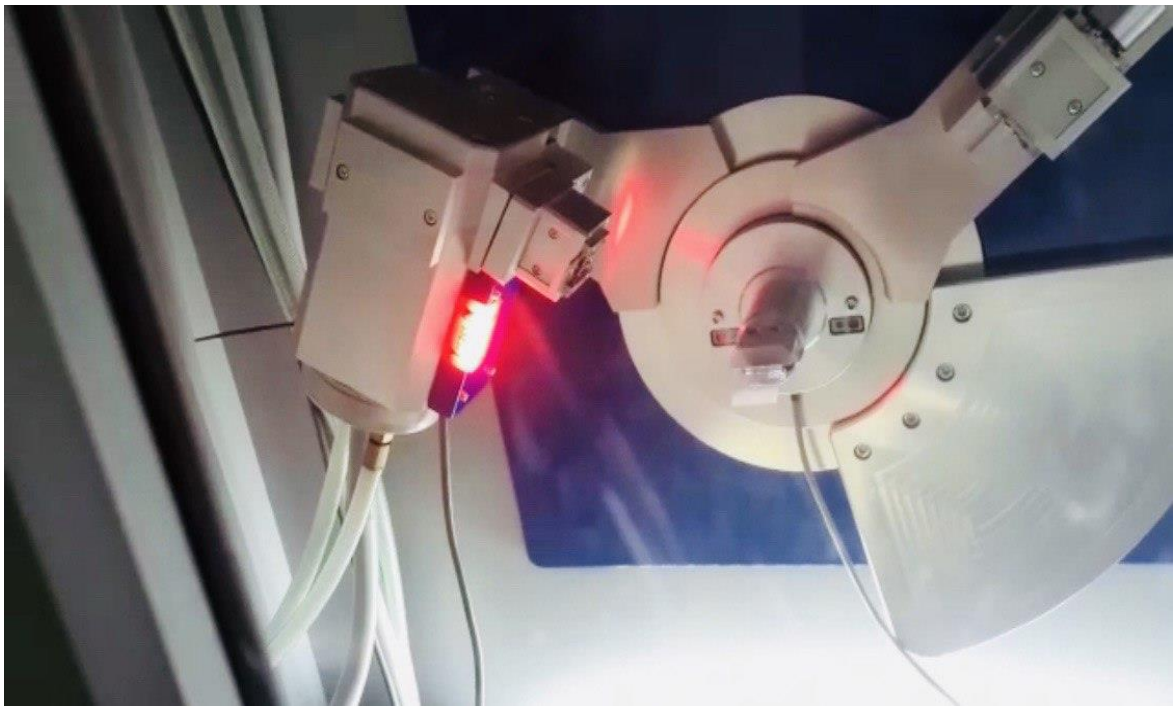

Figure 3.10: X-ray Diffraction Test.

3.7.2 Filed Emission Scanning Electron Microscopy(FE-SEM)

The surface morphology of the prepared was investigated by field emission scanning electron microscopy(FE-SEM) (SIGMA, JSM-7610F, Carl Zeiss, Germany) operating at an accelerating voltage of 10 kV. as shown in Figure 3.11. While the average particle diameter was determined from FE-SEM using Image-J software.

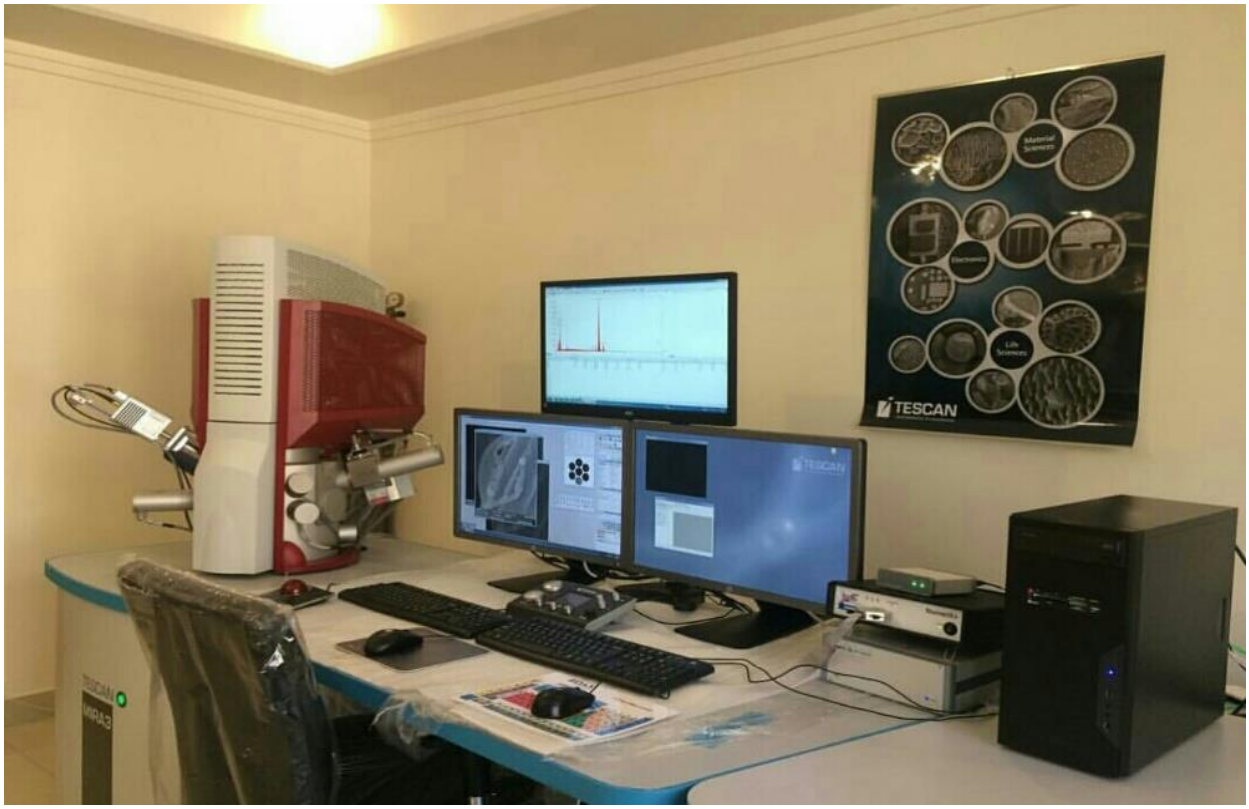

Figure 3.11: Photograph of FE-SEM device.

3.8 Optical Properties

The optical properties of the nanoparticles prepared in this work using UV-visible type spectrophotometer model (CECIL 7200,ENGLAND) shown in Figure 3.12in the wavelength ranged from (200-900) nm. This spectrometer is a one beam type contains two light sources deuterium and tungsten lamp to cover the entire spectral range. Firstly, the spectrometer is normalized using quartz cell containing distilled water. Then the suspension sample was examined in the same quartz cell.

Figure 3.12:UV-visible Absorbance Spectrometer.

3.9Using NPs to Enhanced the Solar Cell by

A previously manufactured homo-junction Si solar cell coated by TiO_2 as antireflection were used. The cells were etched by 1:10 diluted HF acid for 10 min to remove the TiO_2 coating. The Au NPs, Ag NPs, and Au NPs :Ag NPs were deposited on the surface of solar cell by dip coating device at 80 °C. The schematic diagram of the controlled and plasmonic enhanced PV cells were shown in Figure 3.13.

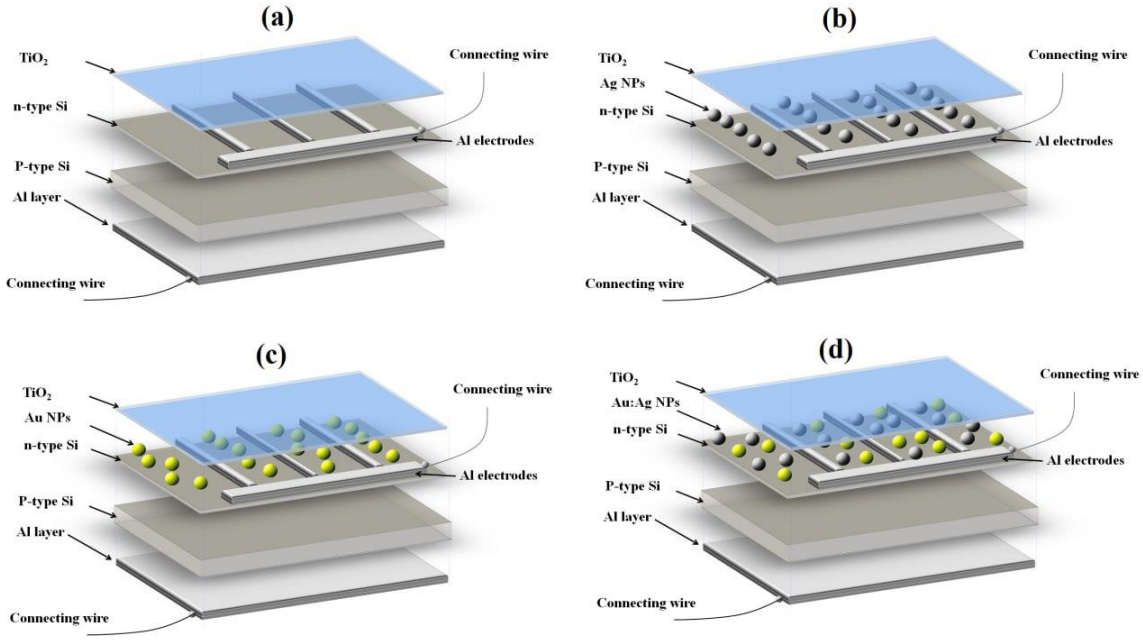

Figure 3.13: Solar Cell Configurations of (a) Control, (b)Ag, (c)Au, (d)Au:AgCoated.

3.9.1 Current –Voltage Characteristics of Solar Cell

The J-V characteristics for the solar cell based on n-Si/p-Si homojunctions substrates under illumination by 100 mW/cm^2 light intensity using a halogen lamp were examined before and after deposition of nanoparticles on substrates .The testing setup consists of Keithley electrometer digital electrometer, voltmeter and D.C. power supply. The applied varied within the range of -3 to 3 Volt. The voltage was adjusted by fine tuning the power supply .The current was measured by the Keithley. Figure 3.14 shows a schematic diagram for circuit used for I-V characteristics measurements.

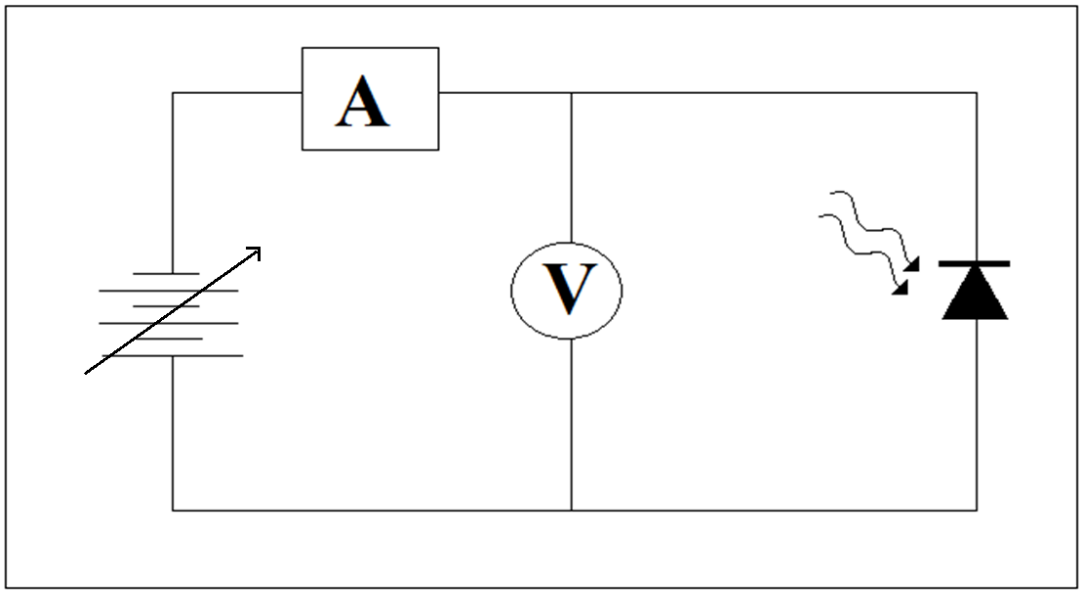

Figure3.14:Schematic Diagram I-V Characteristics Measurements Circuit.

Chapter Four

Results and Discussions

4.1 Introduction

This chapter contains the experimental results, their analysis and discussion, which includes the spectroscopic study of induced plasma and the effect of nanomaterials on the properties of induced plasma. It also includes the structural properties and nano-surface topography study of gold and silver nanoparticles and their mixtures deposited on silicon wafers. The plasmon absorption peak was also investigated and its applicability in improving the efficiency of solar cells.

4.2Plasma Emission Spectroscopy

4.2.1 Plasma Parameters of Selected Samples

The results of emitted spectrum at wavelength (200 to 900nm) by using laser ablation technique at pulse laser energy 100 mJ of the Au and Ag bulk targets, respectively shown in Figures (4.1) and)4.2), the emitted lines were matched with the standard atomic and ionic emitted lines for the used metals (AuI, AuII, AgI, and AgII) in addition to the Hα line at 656.28 nm corresponding to the adsorbed water vapor on the sample surface [111]. In the two spectra, the atomic lines appear with higher intensity compared with ionic ones, indicating the partially ionized plasma of cold plasma. The intensities of the different lines are due to different transition probability and statistical weight of energy levels [112].

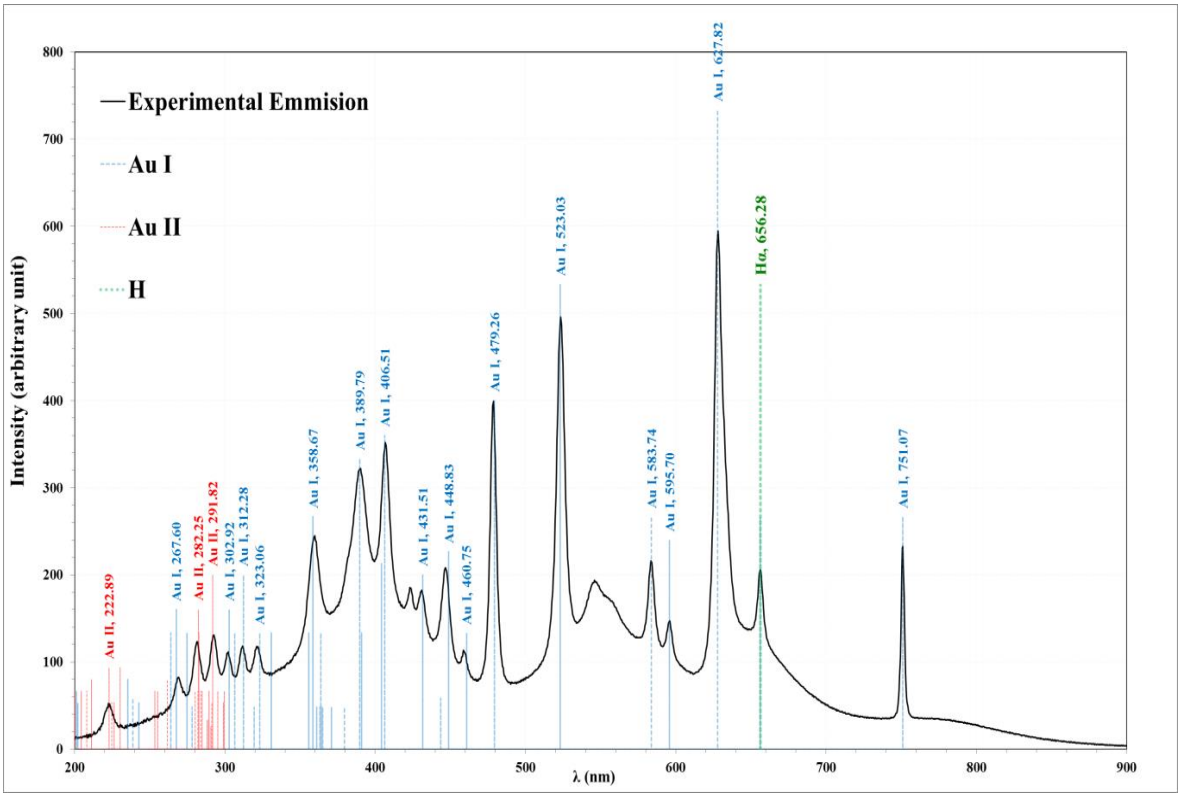

Figure 4.1 :Emitted Spectra lines of plasma from Gold (Au)at laser Pulse Energy (100mJ).

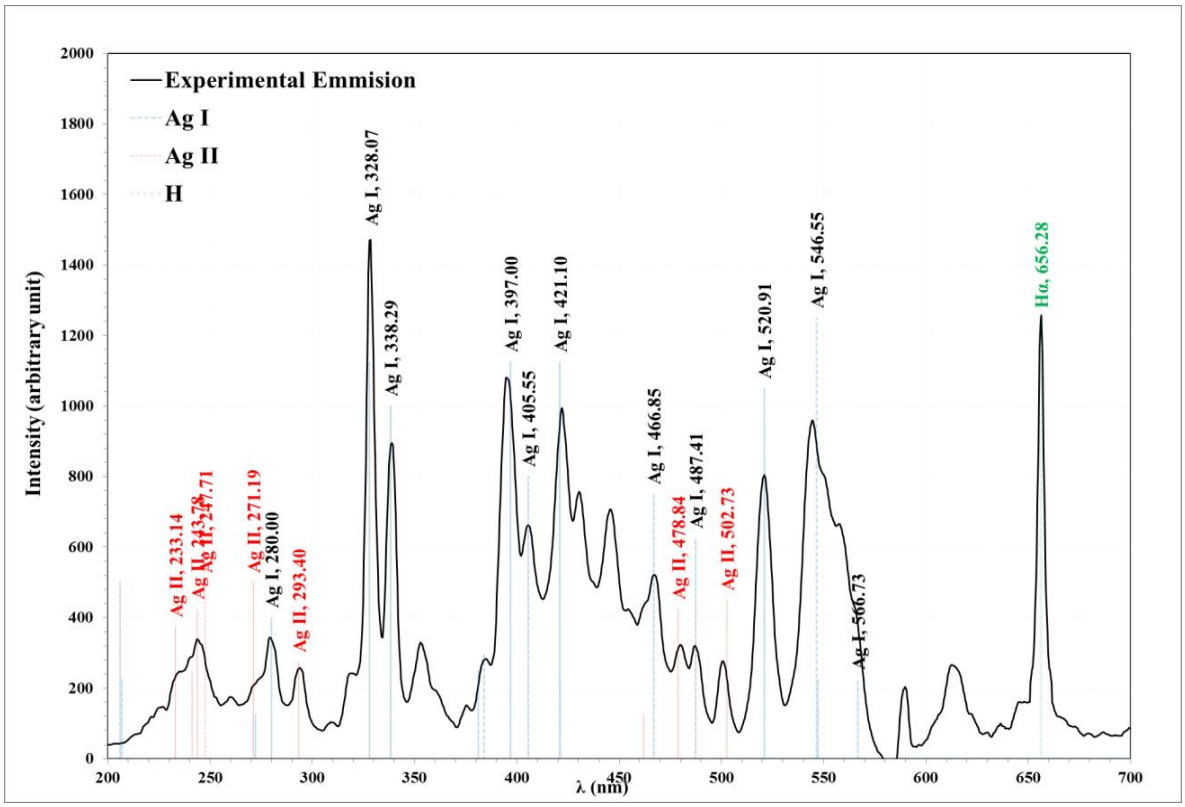

Figure 4.2:Emitted Spectra lines of plasma from Silver (Ag)at laser Pulse Energy (100mJ).

Electron temperature (T_e) was determined according to the Boltzmann Plot using the intensities of atomic lines (AuI, and AgI) emission lines. The parameters of the corresponding electronic transitions were taken from the National Institute of Standards and Technology site (NIST)[111]. Figure 4.3 shows the linear relation between $Ln\left(\frac{I_{ji}\lambda_{ji}}{hcg_jA_{ji}}\right)$ against upper energy level (E_j) of electronic transition, T_e values. The equations of fitting lines were shown in the figures. The values of T_e are equal to the inverse of the slope for the best line fitting. The R^2 values exposed with each line fit with value higher than 0.9 indicate a good linear fit.

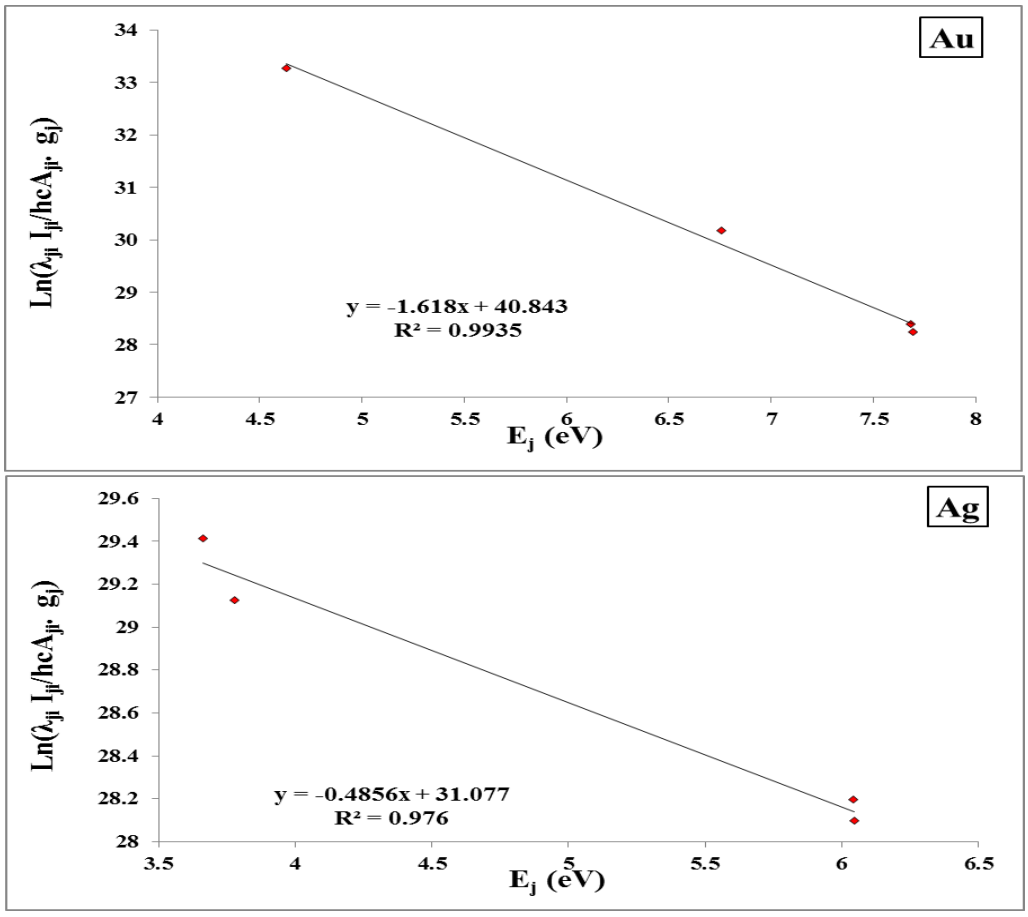

Figure 4.3: Represent of Boltzmann Plot of LIBS in : Gold (Au I)Emission lines, Silver (Ag I)Emission lines.

Figure 4.4 displays the Lorentzian fitting for the $H_\alpha$emission line at 656.28 nm for LIBS from Au and Ag targets. The line breadth ($\Delta\lambda$) was found in the best

Lorentzian fit and was employed to determine electron number density according to the data of electron impact width (ω_m) for H_α [113].

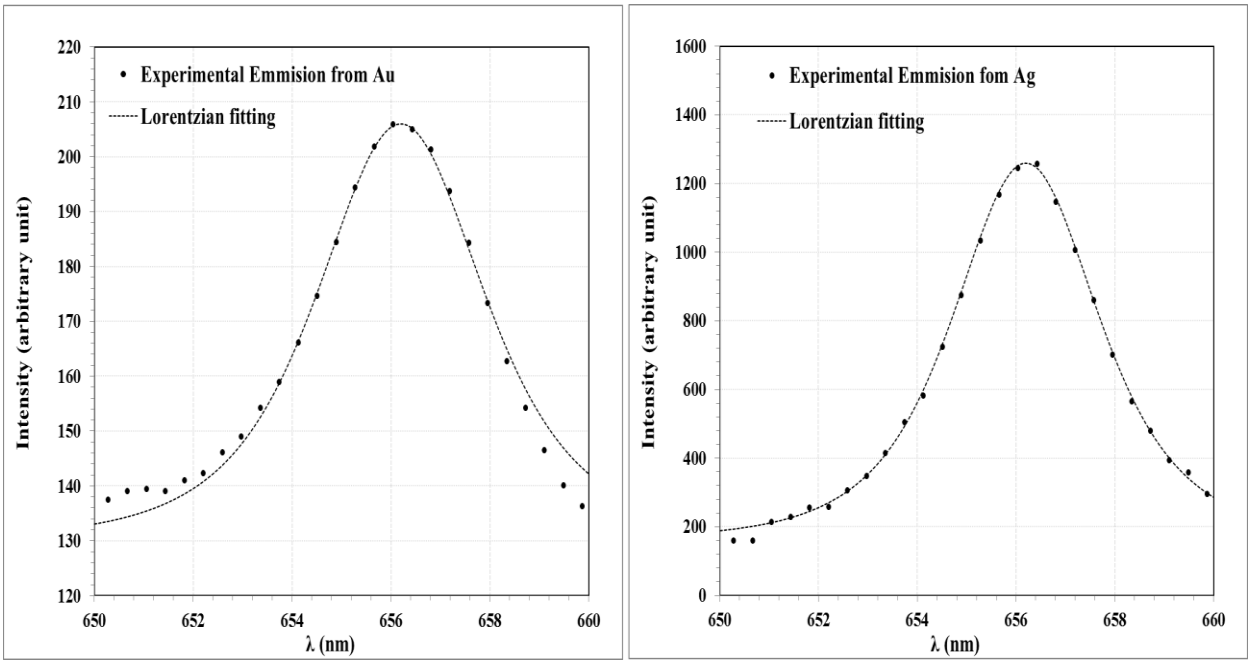

Figure4.4: Lorentzian fitting to Hα line for LIBS from Au and Ag targets.

Other plasma parameters, including plasma frequency (f_p), Debye-length (λ_D), and Debye-number (N_D)were calculated using the equations 2.4, 2.5, and 2.6 respectively, and listed in Table 4.1. The plasma parameters satisfy the plasma criteria. The difference in plasma temperature and electron number density for plasma induced from Au and Ag targets is due to their variation of laser energy absorbance and due to the higher work function of Au than Ag, which acts as a threshold energy to emit electrons from metals.

Table4.1:Parameters of Plasma Induced of Au I, and AgI transitions.

Element type	T_e(eV)	FWHM $\times10^{-7}$ (cm)	$n_e\times10^{16}$ (cm^{-3})	$f_p\times10^{13}$ (Hz)	$\lambda_D\times10^{-6}$ (cm)	N_D
Au I	0.618	4.000	3.090	0.158	33.228	4749
Ag I	2.059	3.500	10.295	0.288	33.228	15821

4.2.2 Enhanced LIBS of Nano particles

The emitted lines were matched with the atomic and ionic lines for Si (Si I, and Si II) , two metals in this part of the work .It is clear that the intensity of the lines is higher and more distinguishable for samples coated by the two types of nanoparticles, especially within the range from 400 to 550 nm, compare with the bulk Si targets. Figure 4.5 and 4.6 showed a comparison between emitted spectra of LIBS for Si target with that coated by the two types of metal nanoparticles Ag NPs, and Au NPs, respectively. The emitted lines were matched with the atomic and ionic lines for Si (Si I, and Si II) and for the two used metals .It is clear that the intensity of the lines is higher and more distinguishable for samples coated by the two types of nanoparticles, especially within the range from 400 to 550 nm, compare with the bulk Si targets. As an example, the Si II (504.1 nm) line enhanced in intensity about 2.1 fold after nano enhancement by the Au NPs. Also, revealing that the spectral lines are more broadening for the nano enhanced samples, which indicates an increase in the plasma density [114]. The probability of breakdown increased as a result of reducing the breakdown threshold on the sample surface[115].

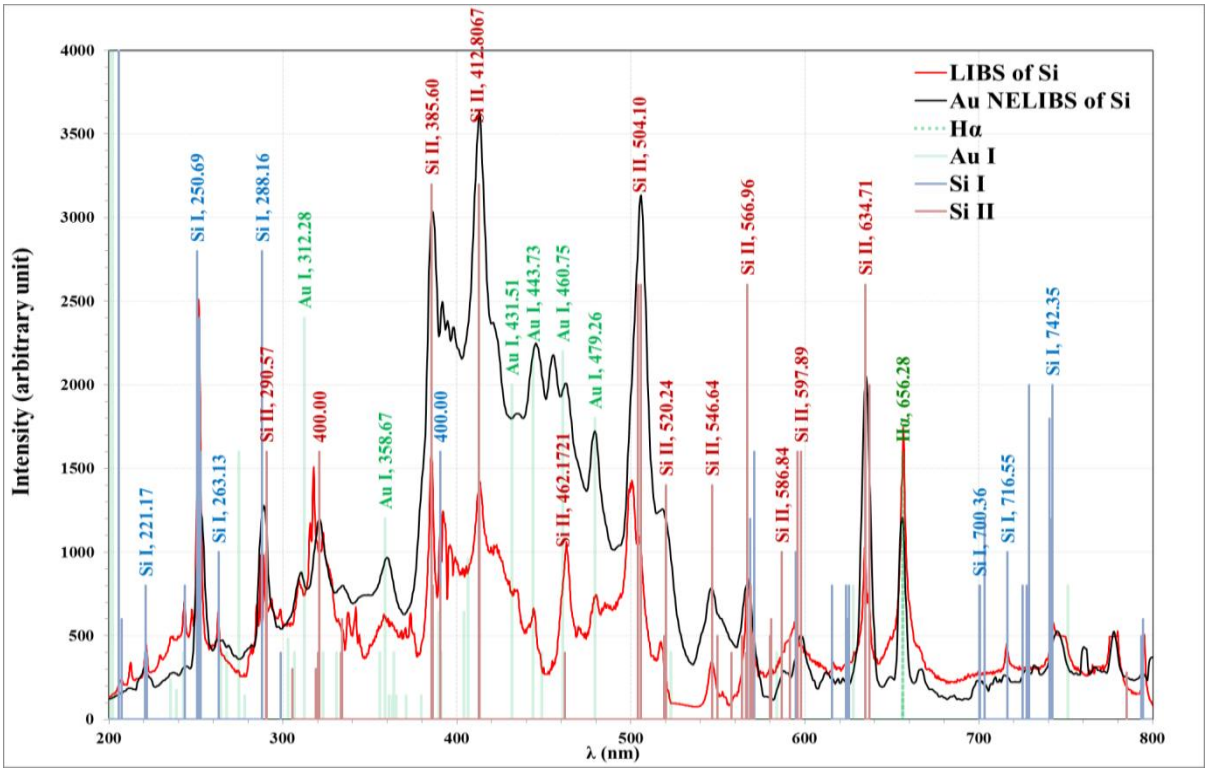

Figure 4.5 : Comparison Between theEmitted Spectra fromBareSi Target with that Coated by the AuNPs.

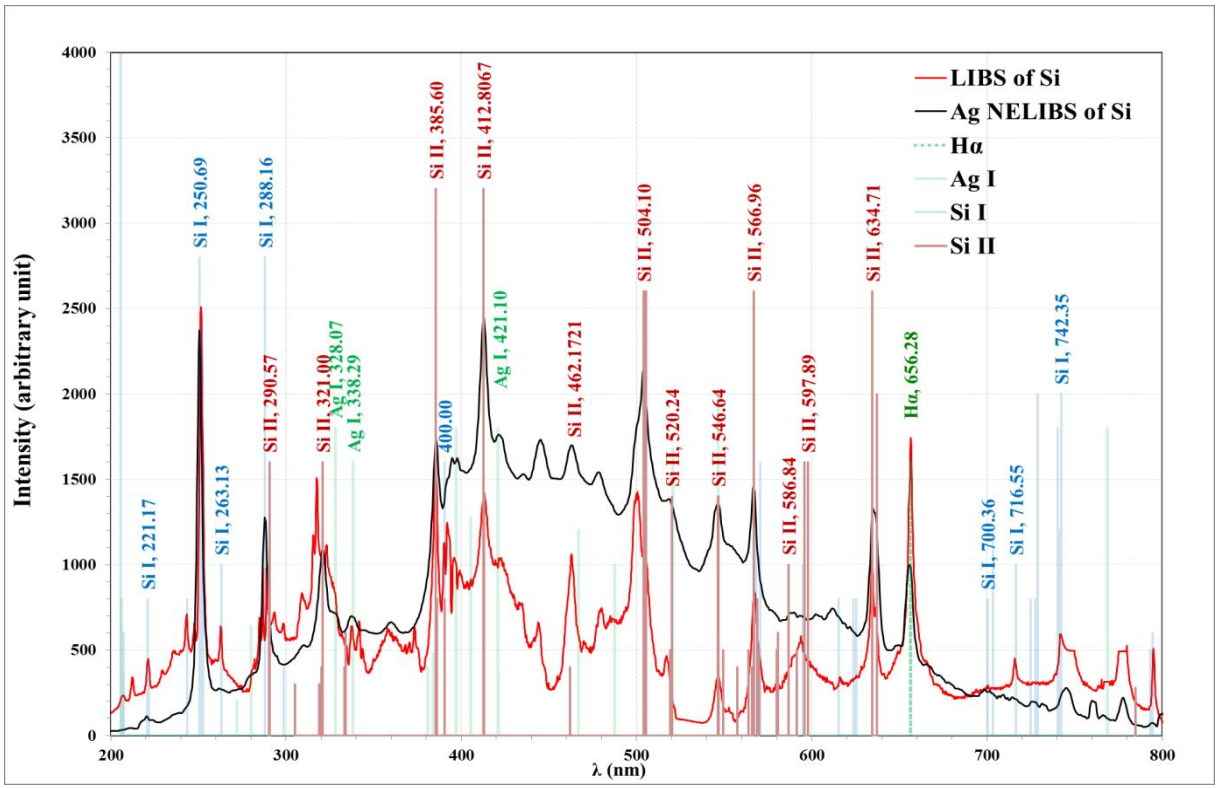

Figure 4.6:Comparison between the Emitted Spectra from Bare Si Target with that Coated by the Ag NPs.

Electron temperature (T_e) was determined by Boltzman-Plot, as shown in Figure 4.7, using the intensities of Si II lines and their parameters from NIST site[111] as listed in Table 4.2.

Table 4.2: Emitted Spectrum Lines Parameters of(Si II).

Wavelength (nm)	Intensity (a.u.)	g_kA_{ki} (s^{-1})	E_i (eV)	E_k (eV)
290.569	150	3.06×10^8	9.838769	14.104461
321.003	114.875	3.17×10^8	10.07388	13.935169
385.602	278.002	1.76×10^8	6.859448	10.07388
504.103	168.133	2.80×10^8	10.066443	12.525262
546.643	31	1.30×10^8	12.525262	14.792721
566.956	40	4.00×10^8	14.199804	16.386036
597.893	160	2.26×10^8	10.07388	12.146991
634.710	213.08	2.34×10^8	8.121023	10.07388

Table 4.2 A: Emitted Spectrum Lines Parameters of (AuI).

λ(nm) EXP.	λ(nm) NIST	Intensity (a.u.)	gk Aki (s-1)	Ei (eV)	Ek (eV)	Ln(λjiIji/hcAji. gj)
406.479	406.507	353.741	3.40E+08	4.6319246	7.68102	28.38990574
478.506	479.258	401.633	5.30E+08	5.1050014	7.6912	28.23608457
583.613	583.737	256.871	5.90E+07	4.6319246	6.7553082	30.18302875
628.43	627.817	600	6.80E+06	2.657625	4.6319246	33.26598577

Table 4.2 B: Emitted Spectrum Lines Parameters of (Ag I).

λ(nm) EXP.	λ(nm) NIST	Intensity (a.u.)	g_kA_{ki} (s^{-1})	Ei (eV)	E_k (eV)	Ln(λjiIji/hcAji. gj)
328.833	328.068	1500	5.60E+08	0.000000	3.778129	29.12358771
338.856	338.289	900	2.60E+08	0.000000	3.663988	29.41004246
520.755	520.908	200	3.00E+08	3.663988	6.043482	28.19256866
546.108	546.55	300	5.20E+08	3.778128	6.045993	28.09552451

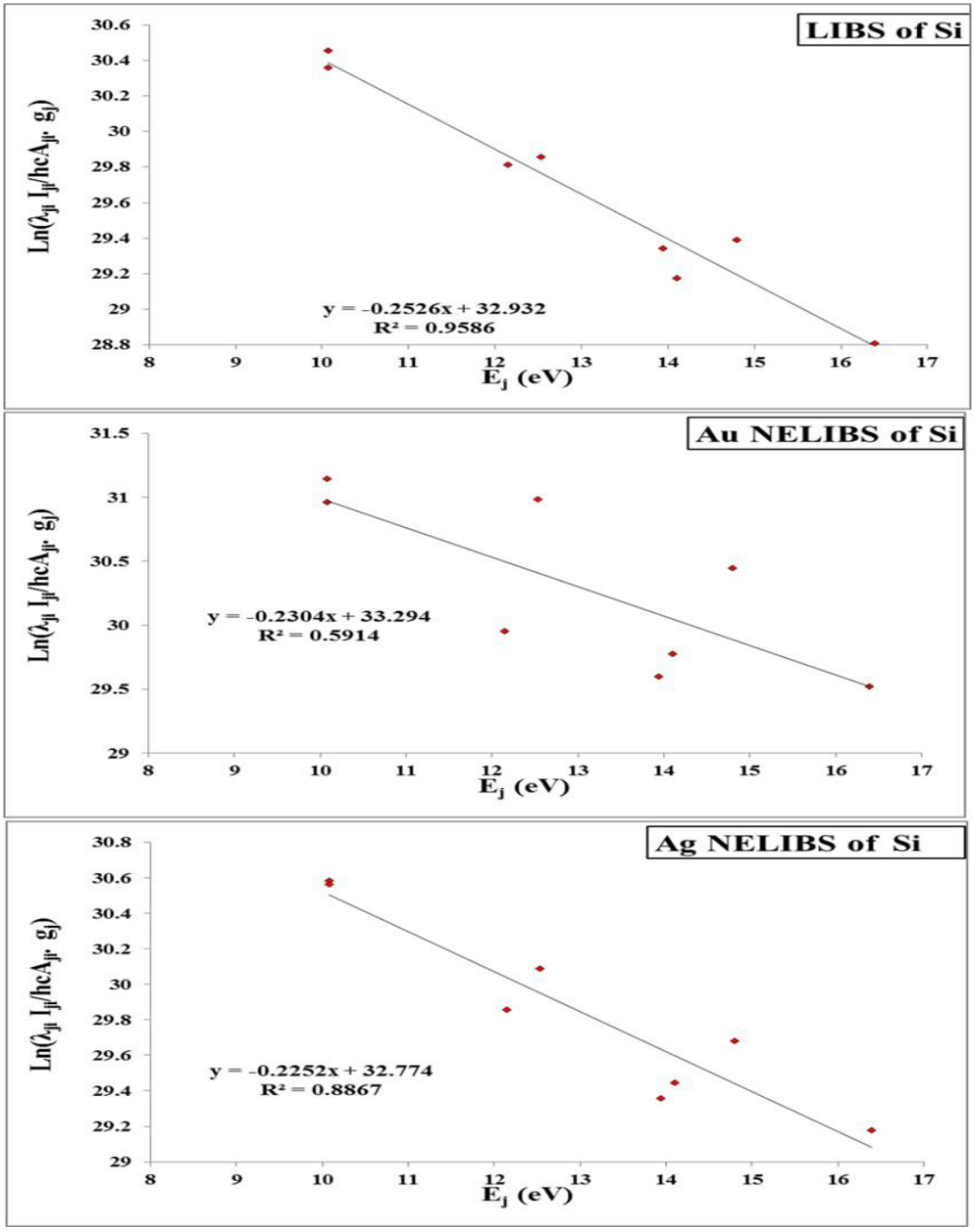

Figure 4.7: Boltzmann Plot for Spectrum lines of Si Iand a- Enhanced with the AuNPs b- Enhanced with the AgNPs.

Figure 4.8 displays the Lorentzian fitting of the Si II (634.71 nm) line ofthe LIBS from the Si target and that enhanced with the AuNPs and AgNPs. The full width of the emitted line (Δλ) was taken from the best Lorentzian which was

employed to determine electron number density in each case according to the data of electron impact width (ω_m) for this selected line[116].

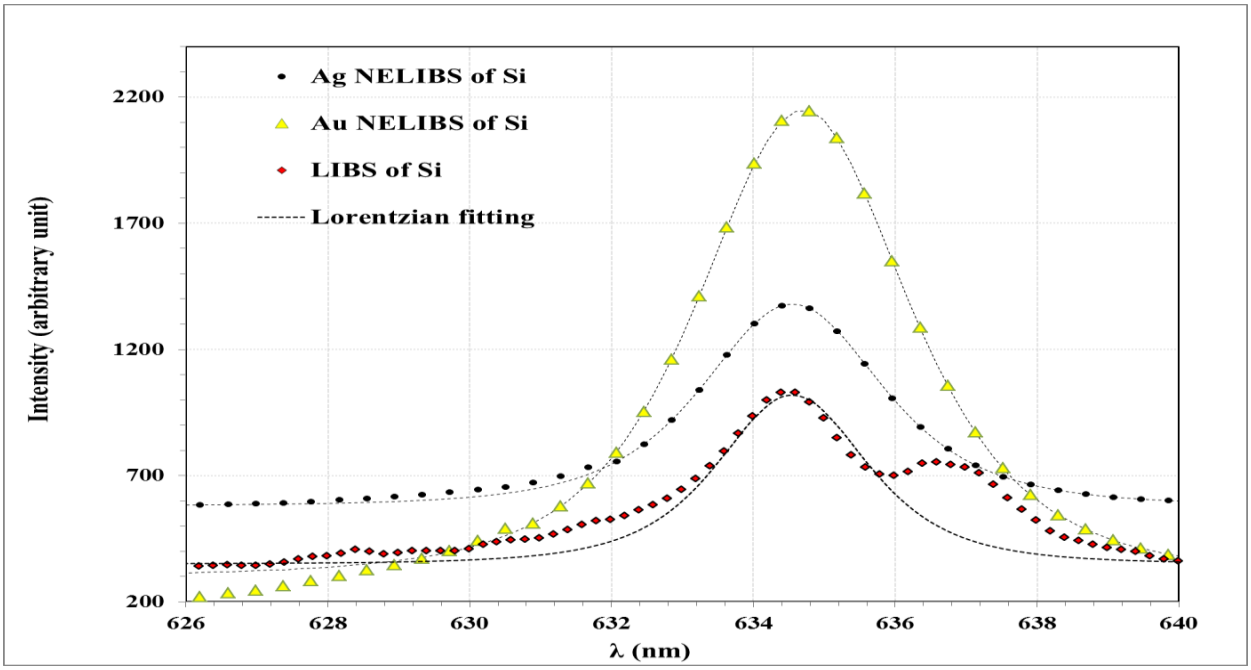

Figure 4.8: LorentzianFitting Corresponding to Si II (634.71 nm)Line for LIBS from Si Target and Enhanced with the Au NPs and Ag NPs.

Figure (4.9)and Figure (4.10)show the emitted spectra for LIBS from bare soda-lime glass targets compared with that coated by the prepared Ag NPs, and other times by Ag NPs, respectively. The emitted lines are well matched with the Si I, Si II, and the two used metals. Additional lines appeared in all spectra corresponding to sodium (Na I line at 589 nm) and calcium (Ca I line at 422.7 nm) as their content in the composition of soda lime glass[117].

It is clear that the intensity of the lines enhanced especially within the range from 400 to 550 nm for samples coated by metal nanoparticles compared with the bulk targets. The breakdown threshold is reduced on the sample surface by two mechanisms as the NPs heating by photon absorption and by the interaction of the electric field with the NPs which causes the electron seed generation by field emission enables[118].

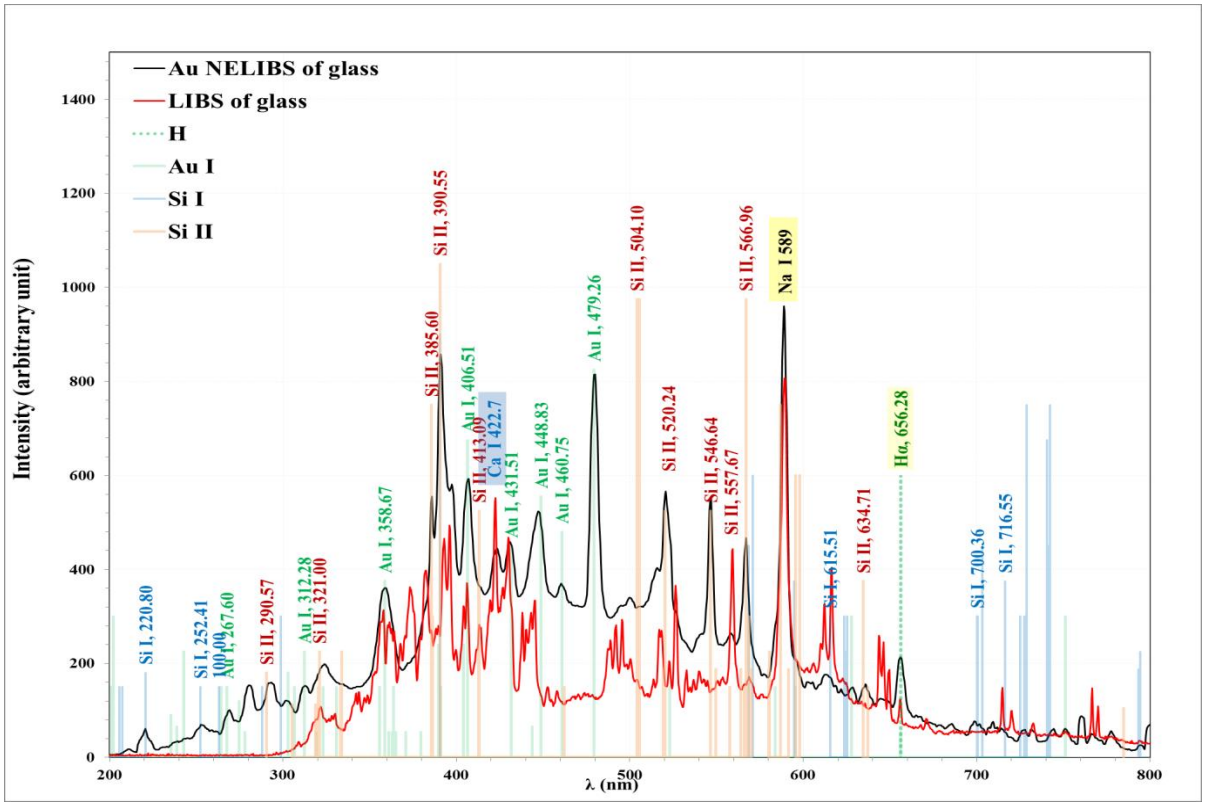

Figure 4.9:Comparison between the emitted Spectrums of bare glass target with that coated by the Au NPs spectra.

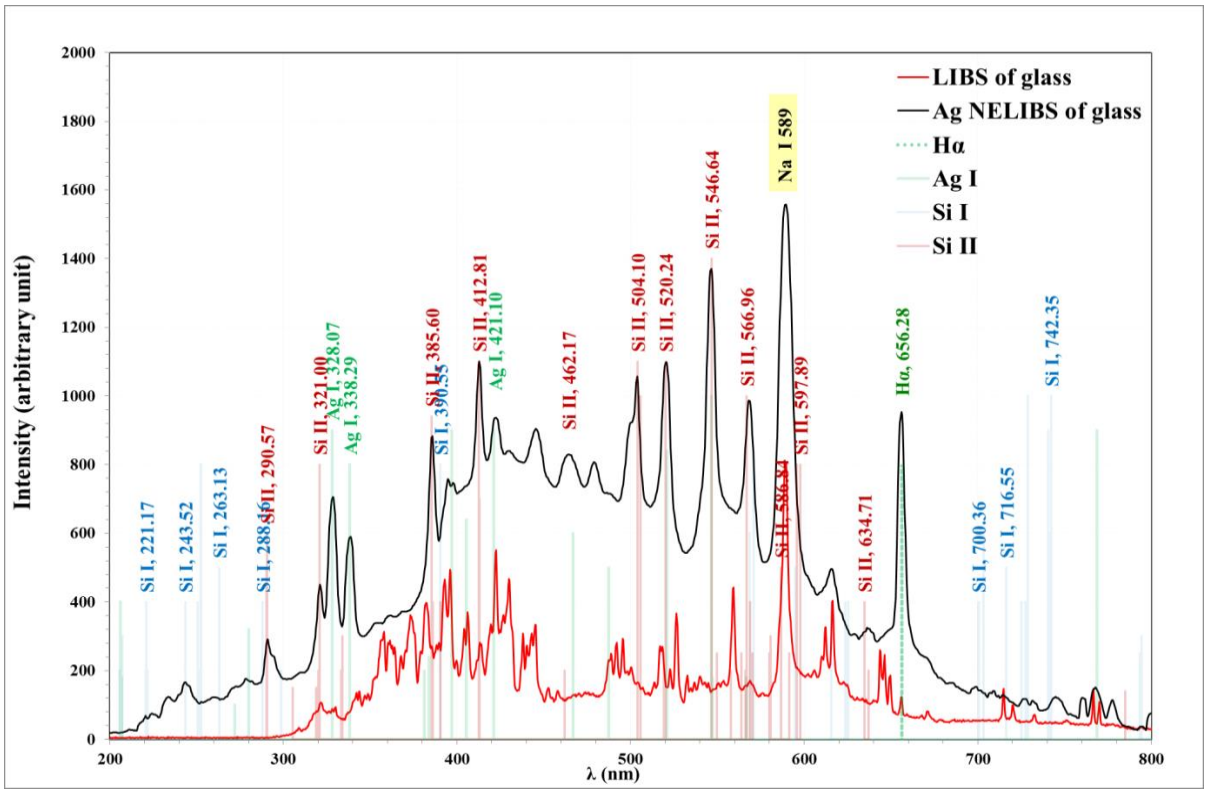

Figure 4.10:Comparison between the emitted Spectrums of bare glass target with that coated by the Ag NPs spectra.

Electron temperature (T_e) of plasma induced from soda lime glass and that enhanced with AuNPs and AgNPs were determined by Boltzmann-Plot, as shown inFigure 4.11. The calculations were done using the intensities of Si II lines. The values of T_e equal to the inverse of the slope for the best linear fit.

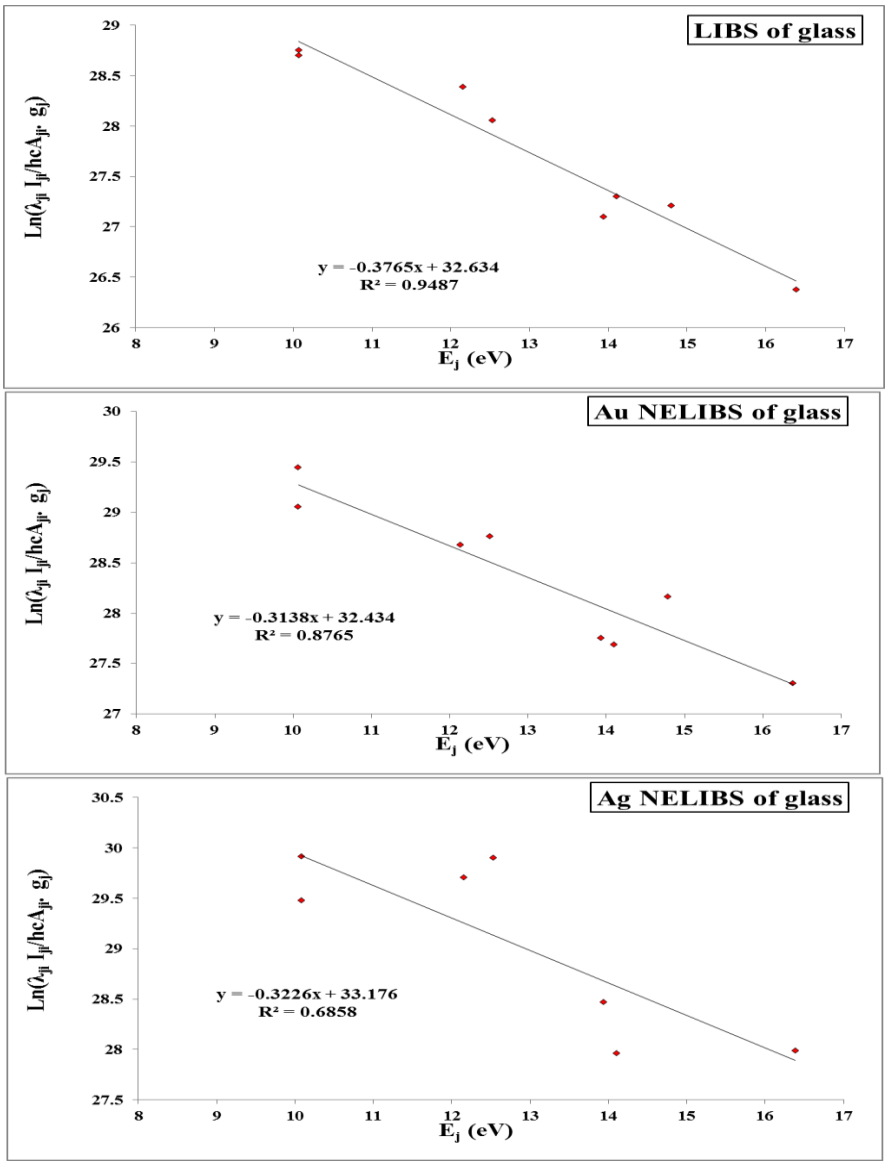

Figure 4.11: Boltzmann Plot of Spectrum lines of Si II a-Enhanced with AuNPs b- Enhanced with AgNPs.

The electron number density of plasma induced of soda lime glass and that enhanced with Au NPs and Ag NPs were determined according to Stark broadening effect. Figure 4.12 displays the Lorentzian fitting for the Si II (634.71 nm) line for LIBS from bare glass target and that enhanced with the Au NPs and

Ag NPs. The full width of the emitted line (Δλ) was taken from the best Lorentzian fitting.

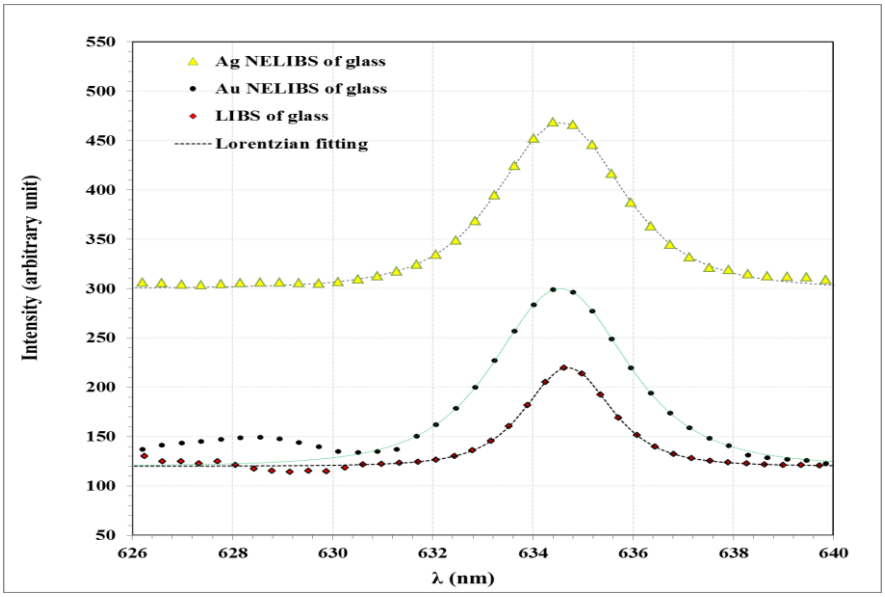

Figure 4.12: Lorentzian Fitting Corresponding to Si II (634.71 nm)Line of the LIBS of the Soda-Lime Glass and Enhanced with the Au NPs and Ag NPs.

Table 4.3lists the plasma parameters including T_e, n_e, f_p, λ_D, and N_d. The plasma parameters satisfy the plasma criteria. The NELIBS decrease the ionization threshold and so increases the electron number density. The electron also can be emitted from samples coated by the plasmonic nanoparticles due to the interaction with laser radiation which causes emitted electrons by field effect emission. On the other hand, increasing T_e is a result of enhancing energy absorption by the nanoparticles.

Table4.3:Parameters of plasma induced of the Si target, glass target ,and that enhanced by the Au NPs, and Ag NPs.

Target	T_e (eV)	FWHM (nm)	$n_e\times10^{18}$ (cm^{-3})	$f_p\times10^{12}$ (Hz)	$\lambda_D\times10^{-4}$ (cm)	$N_D\times10^4$
Si	3.958	2.500	1.042	9.165	0.145	1.33
Au coated Si	4.341	3.500	1.458	10.844	0.128	1.29
Ag coated Si	4.441	3.000	1.250	10.040	1.400	1.44
Glass	2.656	2.000	0.833	8.198	0.133	0.81
Au coated glass	3.187	3.100	1.292	10.206	0.117	0.86
Ag coated glass	3.100	2.900	1.208	9.871	0.119	8.53

Figure (4.13)and Figure (4.14) Shows the LIBS spectra from the bare Si target compared with that coated by the Au NPs : Ag NPs mixture at different ratios (Au :Ag ratio of 75:25, 50:50, and 25:70). The same emitted lines appeared in the previous figures. The intensity of the emitted lines corresponding to Au increased, while on the contrary, the intensity of the spectral lines returning to silver decreased with the increase in the ratio of gold to silver .The lines intensity corresponding to the target enhanced especially within the range from 400 to 550 nm for the samples coated with metal nanoparticles comparability with the bulk targets.

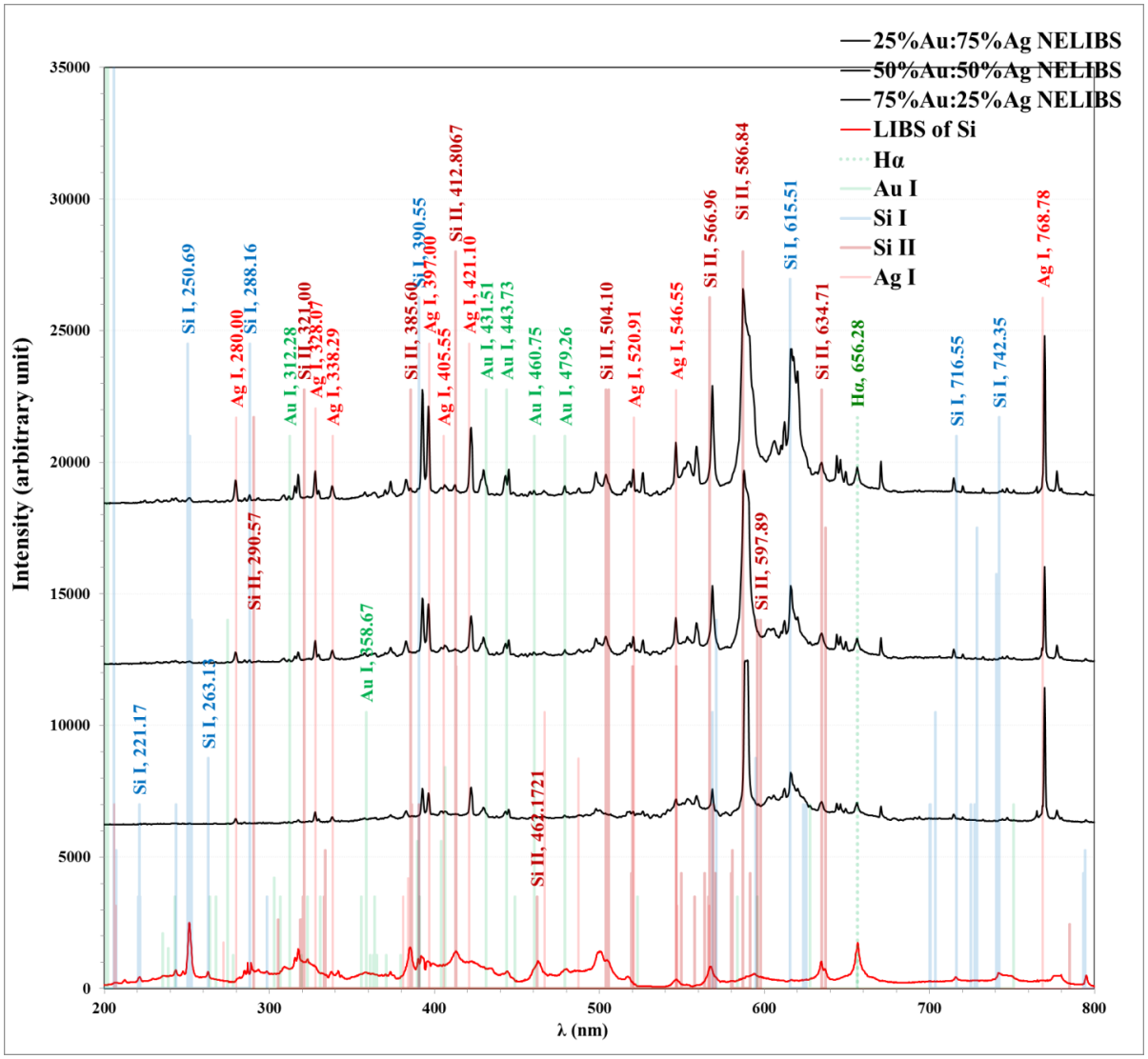

Figure 4.13:the NELIBS for Si target by Au NPs : Ag NPs at different mixing ratios.

Figure 4.14 shows the calculation of electron temperature by Boltzmann-Plot for plasma induced from silicon wafer enhanced by Au NPs :Ag NPs mixture. The calculations were done using the intensities of Si II lines.

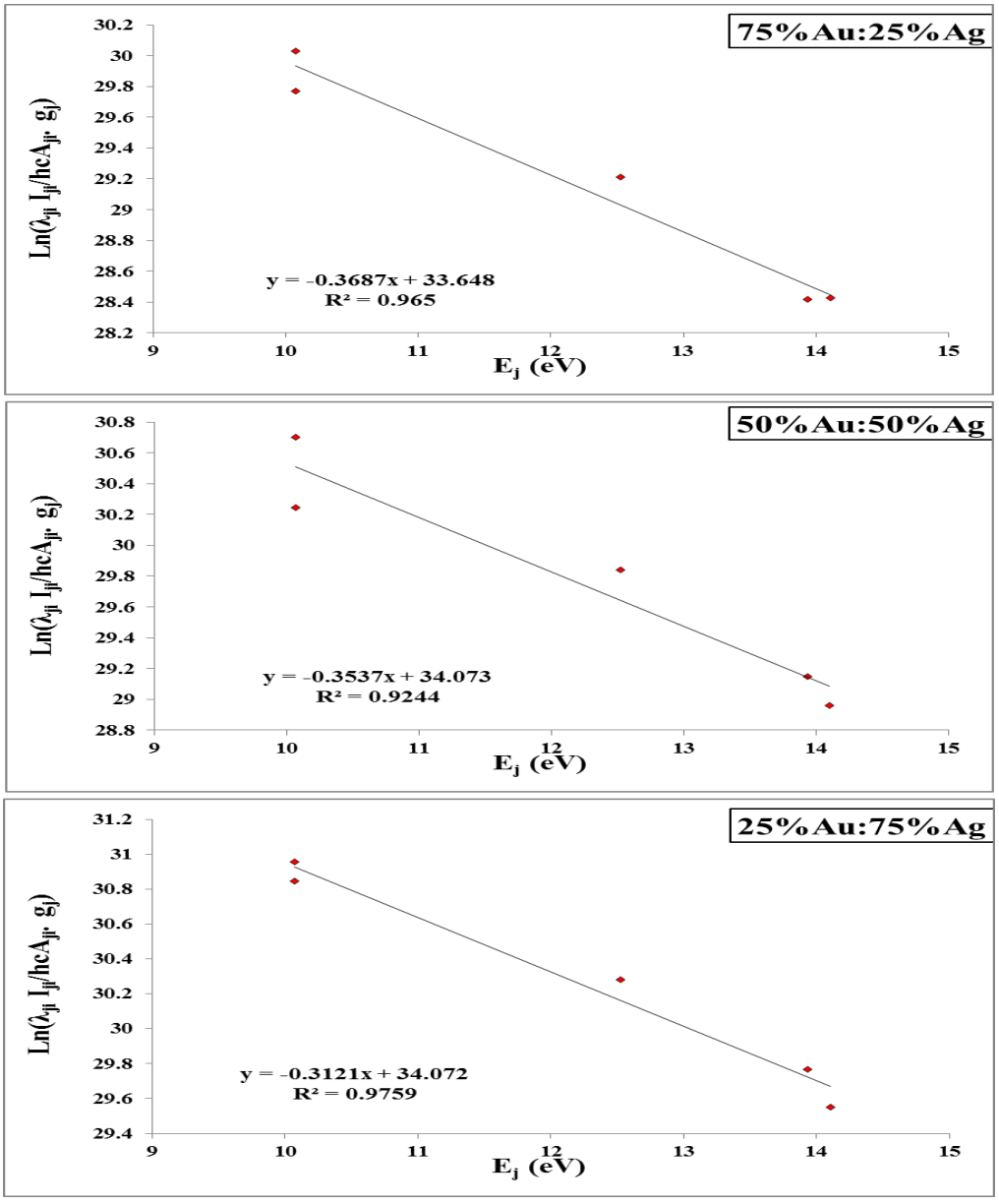

Figure4.14: Boltzmann plot for LIBS from Si target and enhanced with Au NPs :Ag NPs mixture at different ratios.

The electron density for the Si wafer and enhanced by Au NPs : Ag NPs mixture were determined according to Stark broadening effect. Figure4.15displays the Lorentzian fitting for the Si II (634.71 nm) line for LIBS from Si target and that enhanced with Au NPs : Ag NPs mixture.

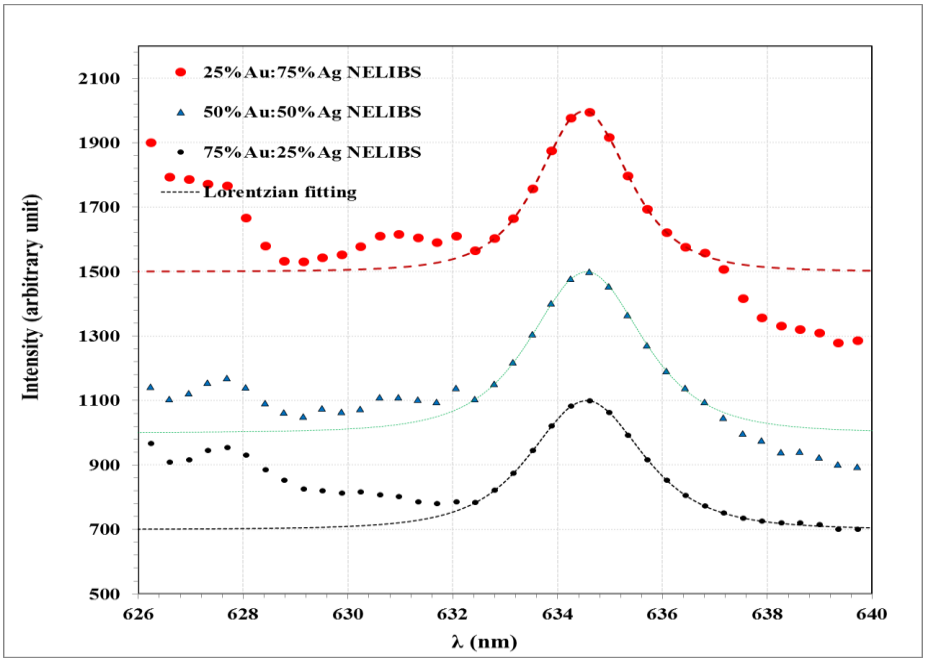

Figure 4.15: Lorentzian fitting corresponding to Si II (634.71 nm) line for LIBS of the Si target and enhanced by Au NPs : Ag NPs mixture at different ratios.

Table 4.4 displays the plasma parameters including T_e, n_e, f_p, λ_D, and N_d for LIBS from Si target enhanced by Au NPs : Ag NPs mixture at different ratios. The NELIBS decrease the ionization threshold and so increases the electron density. The interaction of laser radiation with matter depends on the matter characteristics, so the electron temperature increased while the electron number density decreased with increasing Ag NPs ratio compared with the Au NPs.

Table 4.4:Parameters of plasma induced for LIBS from Si target enhanced by Au NPs : Ag NPs Mixture at Different Ratios

Sample	T_e (eV)	FWHM (nm)	$n_e \times 10^{18}$ (cm^{-3})	$f_p \times 10^{12}$ (Hz)	$\lambda_D \times 10^{-4}$ (cm)	$N_d \times 10^3$
75%Au:25%Ag	2.713	2.500	1.042	9.165	1.199	0.75
50%Au:50%Ag	2.827	2.500	1.042	9.165	1.224	0.80
25%Au:75%Ag	3.204	2.000	0.833	8.198	0.146	1.08

4.3 Structural Properties of the Nanoparticles

In order to evaluate the structural properties of the prepared nanoparticle sample, a non-destructive analytical technique of X-ray diffraction (XRD) was employed .The XRD patterns for Au NPs, Ag NPs, and Au NPs : Ag NPs deposited on a (100) Si wafer were shown in Figure 4.16. Polycrystalline structure with four peaks for each sample located at diffraction angles of 2θ= 38.3301°, 44.3124°, 64.5285°, and 77.5933° corresponding to crystalline planes (111), (200), (220), and (311) according to No. 96-901-2954 and 96-901-2432 standard cards. The addition intense diffraction peak corresponding to the (400) Si substrate located at diffraction angle 69°.It is worth mentioning here that the standard lines for both gold and silver are very close due to the similarity in the crystal structure of the two metals and their possession of a close lattice constant value.

The interspacing distances (d_{hkl}) were determined according to Bragg's formula (equation 2.15), while the crystallite sizes determined according to the Shcerrer's formula[119] (equation 2.16). Table 4.5 lists the structural parameters for the Au NPs, Ag NPs, and Au/Ag mixture deposited on Si wafer. The d_{hkl} values are close to the standard ones. The results showed that crystal size of the obtained NPs have small dimensions of average value (10.9, 12.1, and 11.9)nm for the Au NPs, Ag NPs, and their mixture, respectively. The result in nanomaterials can be used in modern applied fields.

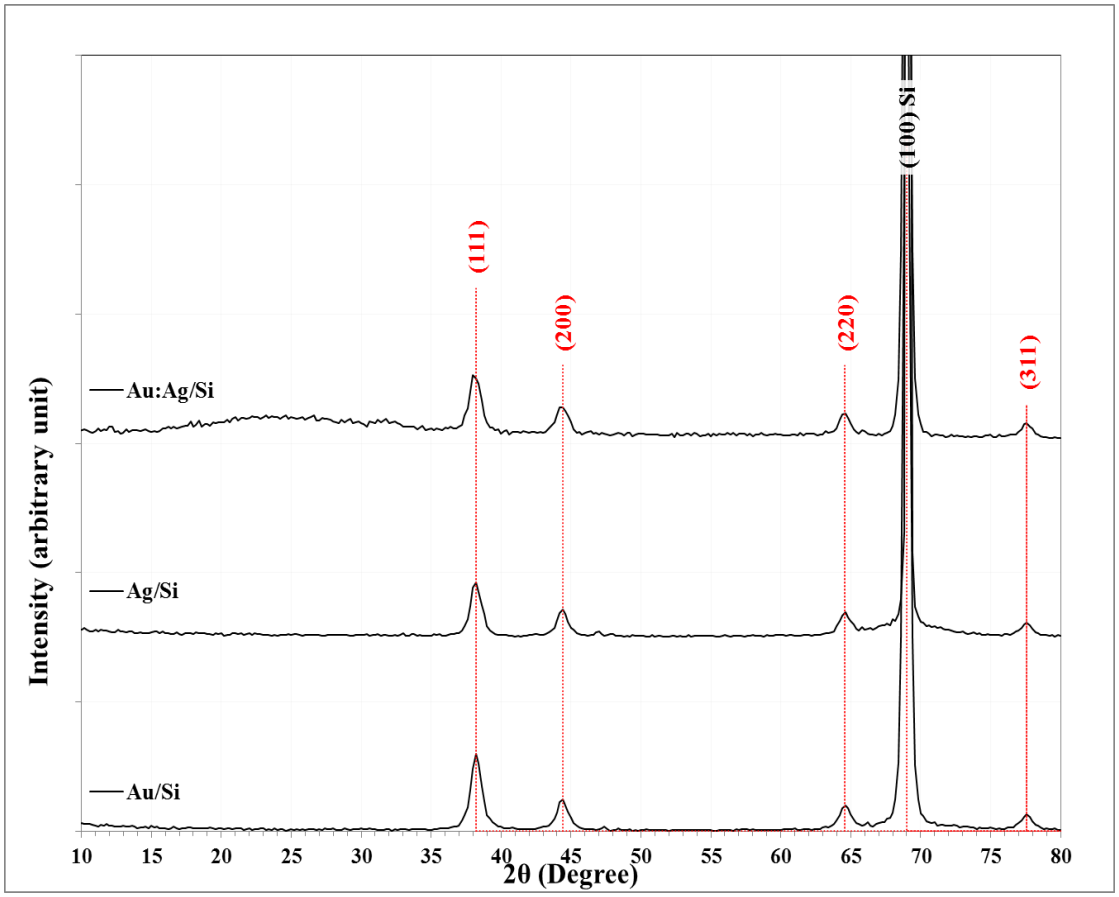

Figure 4.16: The XRD Pattern of the Au NPs, Ag NPs, and Au NPs : Ag NPs Deposited on Si Wafer.

Table4.5: Structural Parameters for the Au NPs, Ag NPs, and Au NPs : Ag NPs Deposited on Si Wafer, Including *2θ* , *FWHM*, d_{hkl}, *D*, and, Miller Indices

Sample	2θ (Deg.)	FWHM (Deg.)	d_{hkl} Exp.(Å)	C.S (nm)	Phase	Hkl
AuNPs /Si	38.3301	0.8502	2.3464	9.9	Cub. Au	(111)
	44.3124	0.8752	2.0425	9.8	Cub. Au	(200)
	64.5285	0.8251	1.4430	11.4	Cub. Au	(220)
	77.5933	0.8251	1.2294	12.4	Cub. Au	(311)
AgNPs /Si	38.1925	0.7802	2.3545	10.8	Cub. Ag	(111)
	44.4499	0.6601	2.0365	13.0	Cub. Ag	(200)
	64.5285	0.7701	1.4430	12.2	Cub. Ag	(220)
	77.5933	0.8251	1.2294	12.4	Cub. Ag	(311)
(Au:Ag)NPs /Si	38.0550	0.7630	2.3627	11.0	Au:Ag	(111)
	44.2436	0.7441	2.0455	11.5	Au:Ag	(200)
	64.5285	0.6602	1.4430	14.2	Au:Ag	(220)
	77.5933	0.9351	1.2294	10.9	Au:Ag	(311)

The (111) planes were selected to determine the lattice constant for cubic structure according to equation 2.15.Table 4.6 illustrates the lattice constant value(a) for cubic Au and Ag structure, and average crystallite size, for the three NPs samples deposited on Si wafer.The (a) values are very close to their standard one.

Table 4.6:Lattice Constant and Average Crystallite Size for the Au NPs, Ag NPs, and Au NPs : Ag NPs.

Sample	a (Å)	Average D(nm)
Au NPs	4.0641	10.9
Ag NPs	4.0782	12.1
(Au : Ag)NPs	4.0924	11.9

4.4 FE-SEM Measurements

The FE-SEM images displays in the Figure 4.17,at two magnification powers of 50.0 kX and 200.0 kX, for the Au NPs, Ag NPs, and Au NPs: Ag NPs deposited on Si wafer. The Au NPs appeared to have spherical shapes which had almost the same size uniformly deposited on the substrate. The Ag NPs also have spherical shapes of about 12 nm diameter, but aggregate to each other forming accumulations of about 200 nm diameter. These aggregations were occurred due to the oxidization capability of silver metal. The image of mixed sample consists the two shapes of nanoparticles. Also, the nano samples appeared to have almost spherical structures.

Figure 4.18 shows the granulate cumulating distribution number percentage for the diameters of Au NPs, Ag NPs, and Au NPs : Ag NPs deposited on Si wafer determined by Image J software. The spherical shapes of Au NPs have uniformly sprayed over the surface of narrow distribution from 13 to 29 nm with an average diameter of 19.49 nm .Wide particle size distribution appeared for the Ag NPs spread from 13 to 39 nm. The mixed sample consists the two shapes of nanoparticles, so the distribution appeared as double modes centered around 10 and

23 nm diameters. The average particle diameter was 12.42 nm.

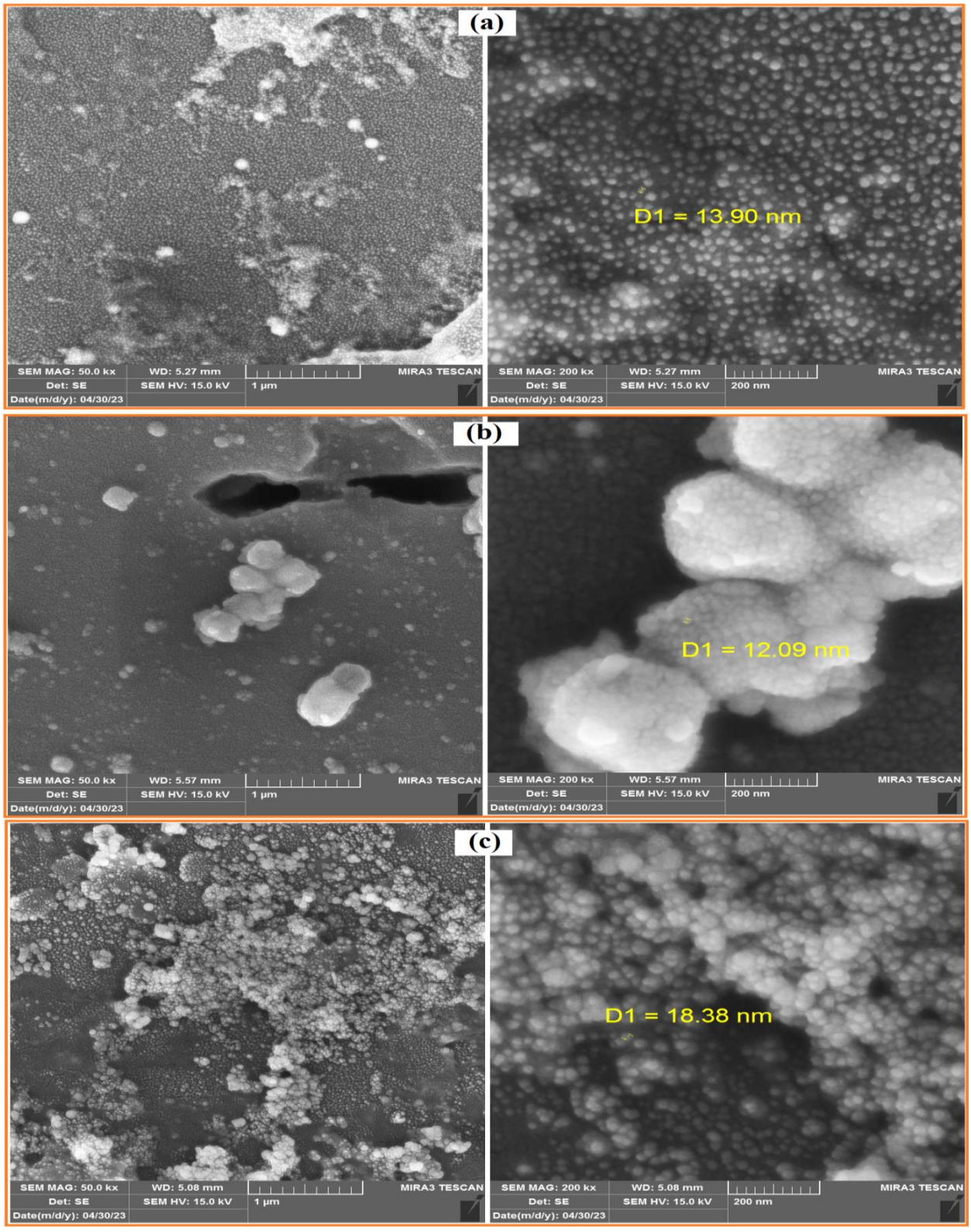

Figure 4.17: Represents of FE-SEM Images for(a)Au NPs, (b) Ag NPs, and (c) Au NPs : Ag NPs Deposited on Si.

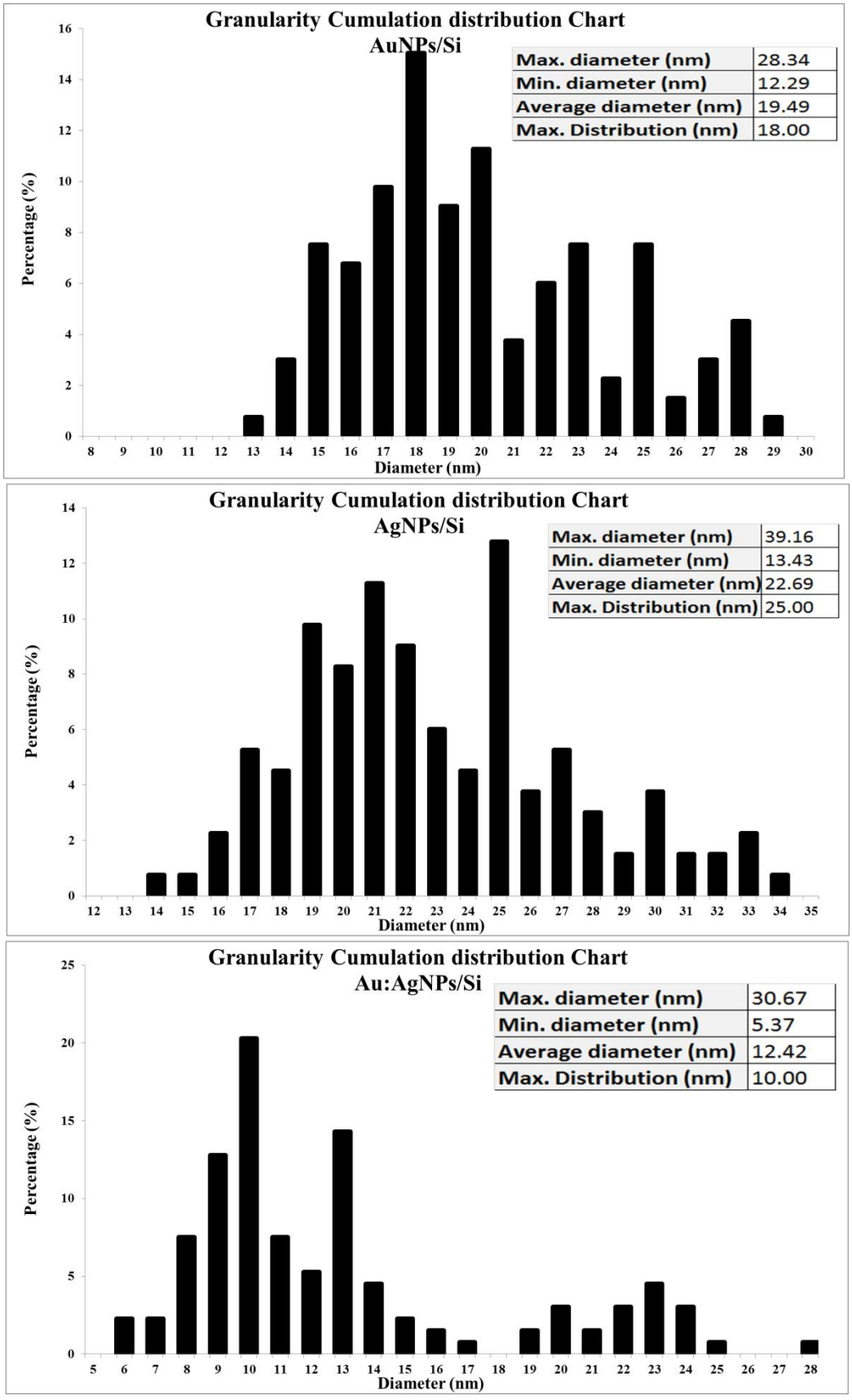

Figure 4.18: Particle Size Histogram determined using Image J Software of the Au NPs, Ag NPs, and Au NPs: Ag NPs Deposited on Si.

4.5 Optical Properties of Nanoparticles

The optical absorbance spectra of the Au NPs suspensions in distilled water prepared by different numbers of pulses (200, 400, 600, and 800) using a fundamental wavelength of Nd:YAG laser were shown in Figure 4.19. The absorption pattern for Au NPs shows a plasma line peak located around 523 nm wavelength, which are the characteristics local of Au NPs. These absorption bands due to the interaction of incident electromagnetic wave with the confined oscillated charged within nano range. The band broadening indicate on wide range of nanoparticle size distribution [120]. The plasmon peak increased in intensity with increasing number of pulses from 200 to 800 due to increasing the NPs concentration in water as a result of increasing the ablated material. As shown in Table 4.7 , the LSPR band wavelength for the Au NPs increased from 523 to 527 nm with increasing the number of pulses from 200 to800. The red-shifted of the indicates an increasing mean size of metal NPs [121].The band broadening indicate on a wide distribution of particle size[122].

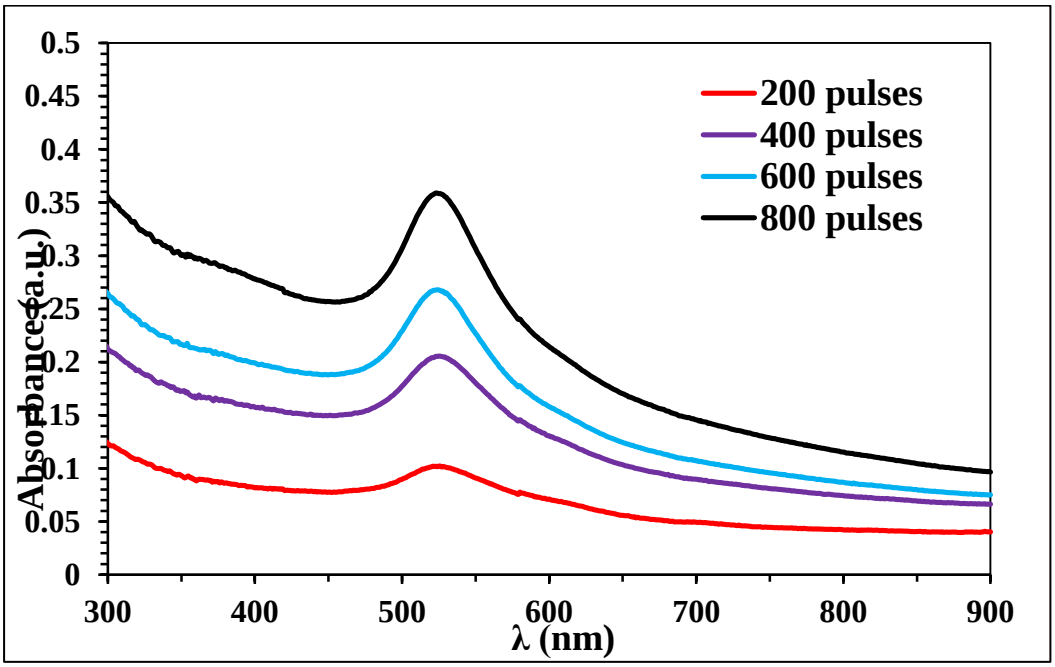

Figure 4.19: UV-VIS Absorbance of Au NPs suspension in distilled water prepared by 1064 nm laser using different numbers of pulses(200, 400, 600, and 800 pulses).

Table 4.7: The Wavelength of Absorbance of the Au NPs in water prepared by different numbers of pulses.

Number of pulses	λ (nm)	Absorbance
200	523	0.102
400	524	0.206
600	526	0.268
800	527	0.359

The optical absorbance spectra of the Ag NPs suspensions in distilled water prepared by different numbers of pulses (200, 400, 600, and 800) using1064 nm wavelength of Nd:YAG laser was shown in Figure 4.20. The absorption curves show band located around400 nm wavelength,which are the characteristics LSPR bandforAgNPs[123]. NPs concentration is high when the increase of intensity with increasing number ofpulses. The band of wavelength slightly shifted from 400 to 404 nm with increasing the number of pulses from 200 to 800 indicating increasing mean size [122].

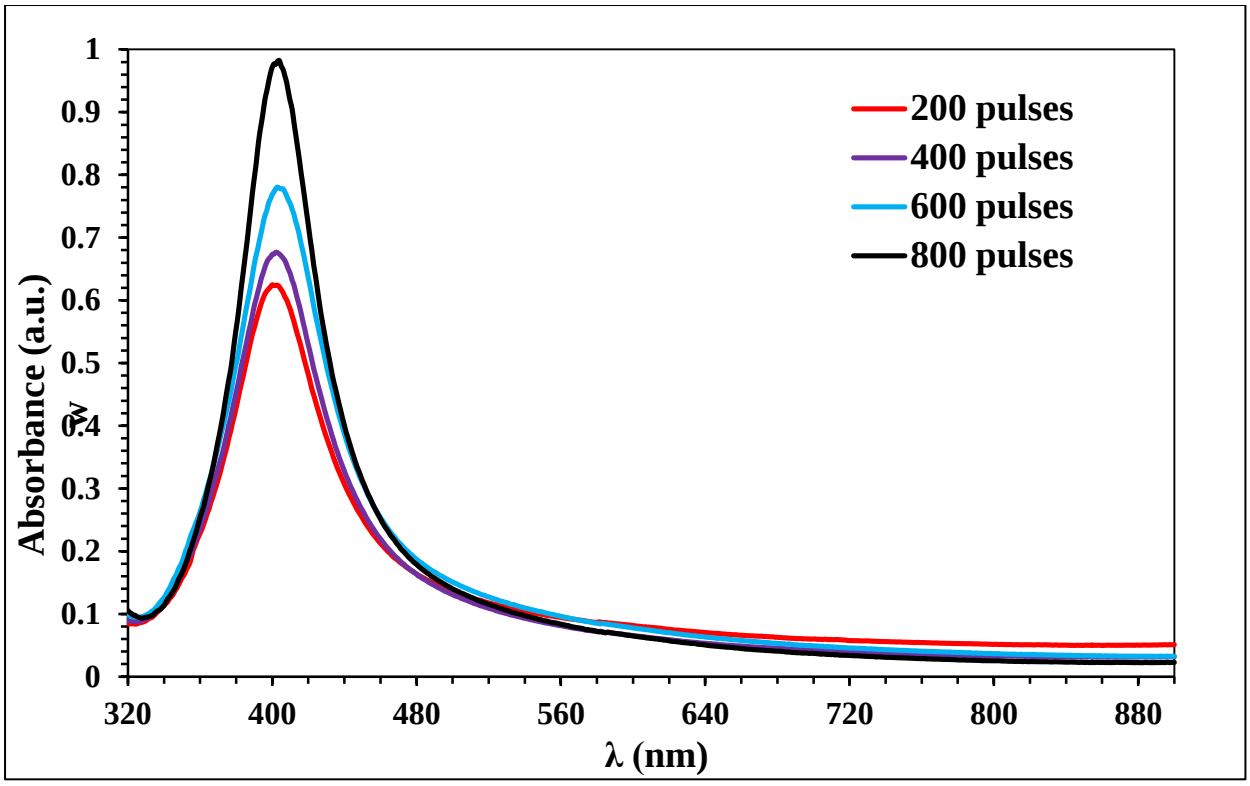

Figure 4.20: UV-VIS Absorbance of the Ag NPs suspension in distilled water prepared by 1064 nm laser using different numbers of pulses(200, 400, 600, and 800 pulses).

Table4.8: The Wavelength of Absorbance of the Ag NPs in Water prepared by different numbers of pulses.

Number of pulses	λ (nm)	Absorbance
200	400	0.625
400	402	0.677
600	403	0.781
800	404	0.982

The optical absorbance spectra of the Au NPs : Ag NPs mixture in distilled water at different ratios (100:0, 75:25, 50:50, 25:75, and 0:100) were shown in Figure 4.21. The absorption pattern for the mixed samples appeared with dabbled band corresponding to the two types of the metal NPs. These absorption bands corresponding to the Au NPs decreased while the band for the Ag NPs increased with increasing the Ag NPs ratio corresponding to the Au NPs. This mixing can be used to tune the absorbance to a selected range .Table 4.9 lists of wavelength of maximum absorbance for the Au NPs : Ag NPs mixture at the different ratios.

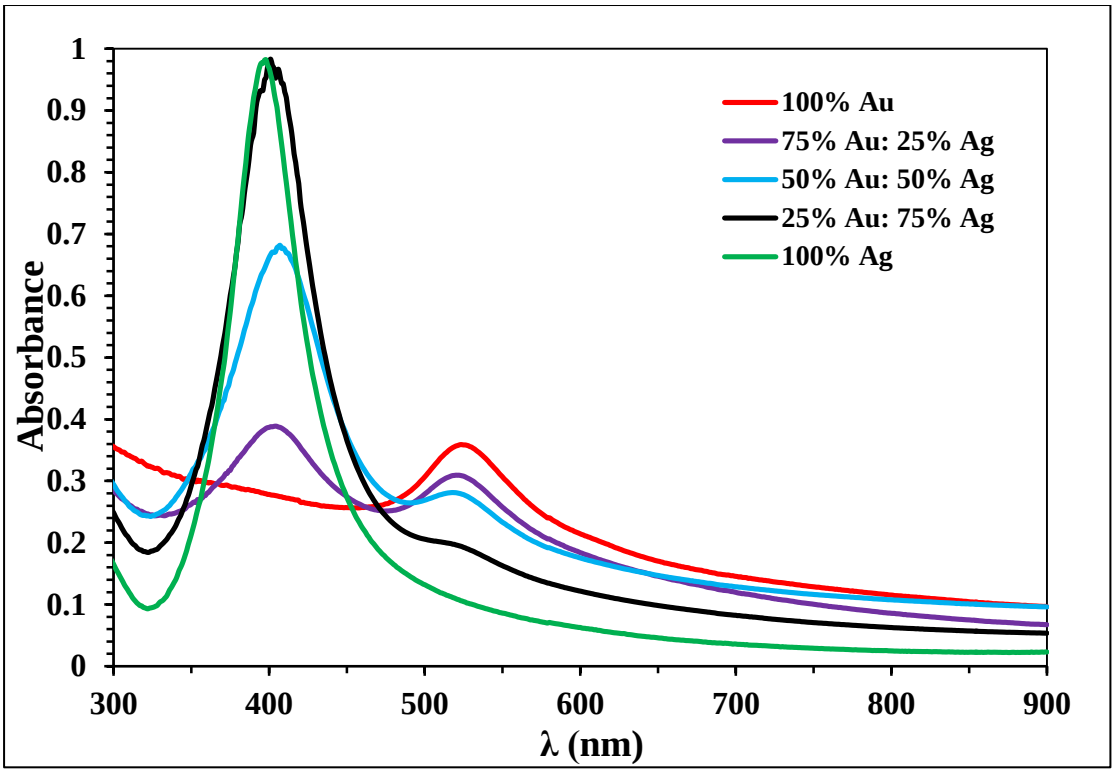

Figure 4.21: UV-VIS Absorbance for the Mixed Au NPs : Ag NPs Suspension in Distilled Water at Different Ratios.

Table 4.9 : The Absorbance of wavelength bands for the mixed Au NPs : Ag NPs Suspension in distilled water at different ratios.

Sample	λ (nm)	Absorbance	λ (nm)	Absorbance
100% Au	-	-	523	0.359
75% Au: 25% Ag	404	0.389	520	0.309
50% Au: 50% Ag	407	0.682	518	0.281
25% Au: 75% Ag	401	0.983	-	-
100% Ag	398	0.982	-	-

4.6 Solar Cell Enhancement

The result of current density –voltage (J-V), and power–voltage characteristics (P-V) for a commercial homojunction P-Si/n-Siunder illumination of (100 mW/cm^2) by a halogen lamp, which simulate the sunlight irradianceis showin Figure 4.22. The sample exhibits the photovoltaic effect with a cross area in the fourth quarter of the J-V curve. The open circuit voltage was 0.65 V and the short circuit current density 4.40 mA/cm^2. The maximum harvesting power was 1.64 mW per centimeter square at 0.4 V. The maximum power represented as an area of the rectangle drawn inside the cross area of $P_m=J_m \times V_m$. The final efficiency was 1.36%. While the shunt resistance and series resistance were 181.36, and 52.45Ω, respectively.

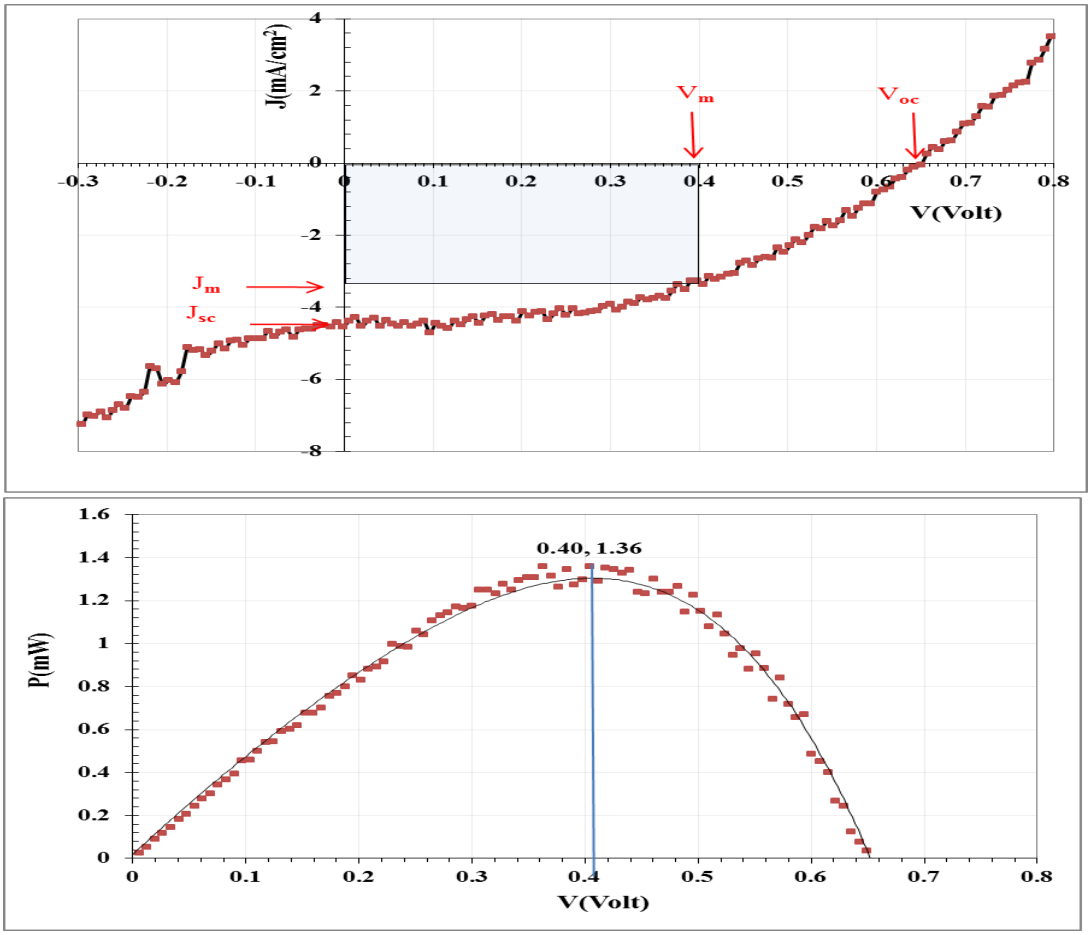

Figure 4.22: J-V and P-V Curves for the Pure Solar Cell.

Figure (4.24) shows the current J-V, and P-V curves for coated solar cells by Au NPs, Ag NPs, and their mixture under illumination of 100 mW/cm^2. All samples exhibit photovoltaic effect with a cross area in the fourth quarter of J-V curve. By comparing the results with the untreated sample, we note that there was no change or a slight change in the open circuit voltage value, while the short circuit current values increased, but with varying values. An increase of I_{sc} values is due to the presence of metal particles, which is done by two mechanisms: the first is due to the increase in absorption due to the scattering that occurs on the surface of the cell, which leads to photon trapping inside the cell, and increases the absorption process. The second is enhancing the solar cell efficiency by the LSPR effect, which cause accelerated separated charge and rapid injection of electrons

into semiconductor materials, so, lowered recombination rate[124]. Increment in photocurrent may assign to helpful injection of hot electrons by SPR effect [125].

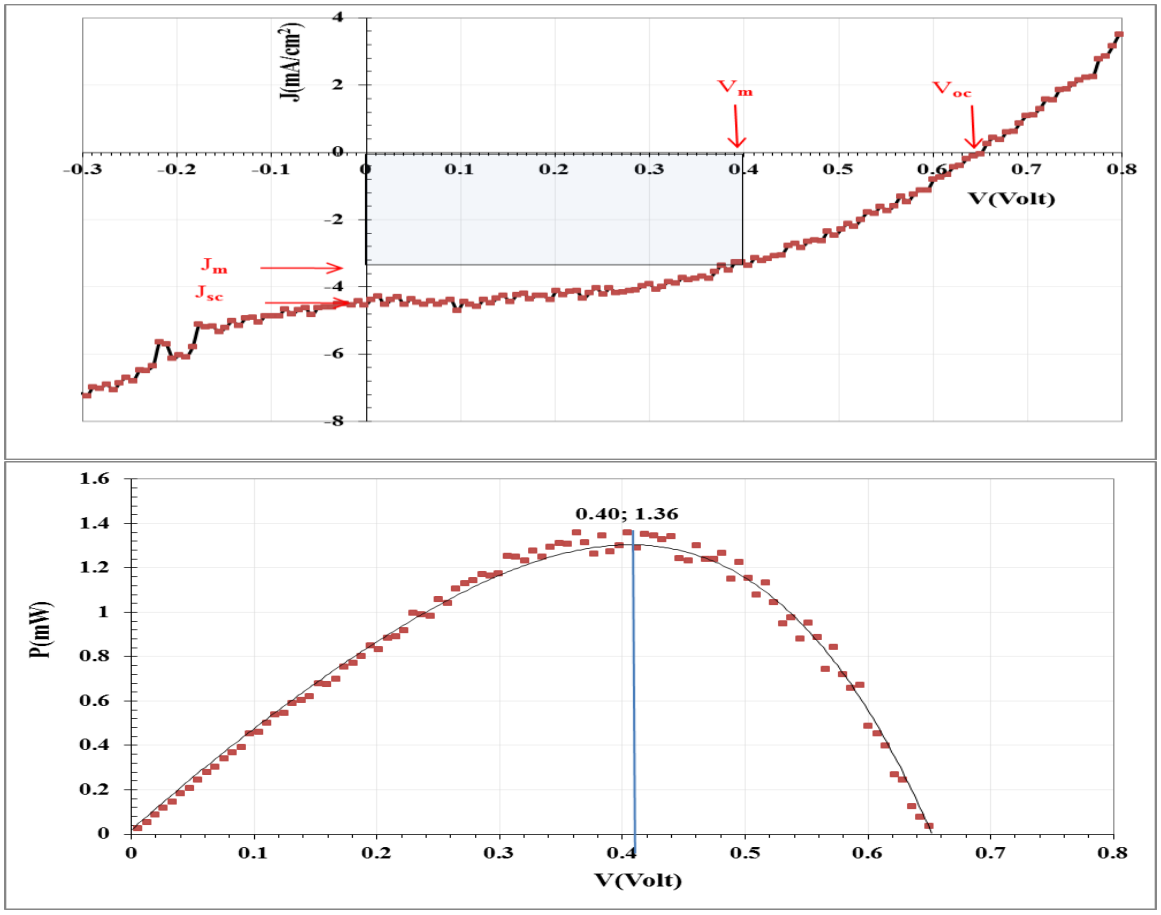

Figure 4.23: J-V and P-V curves for the solar cell coated by AgNPs.

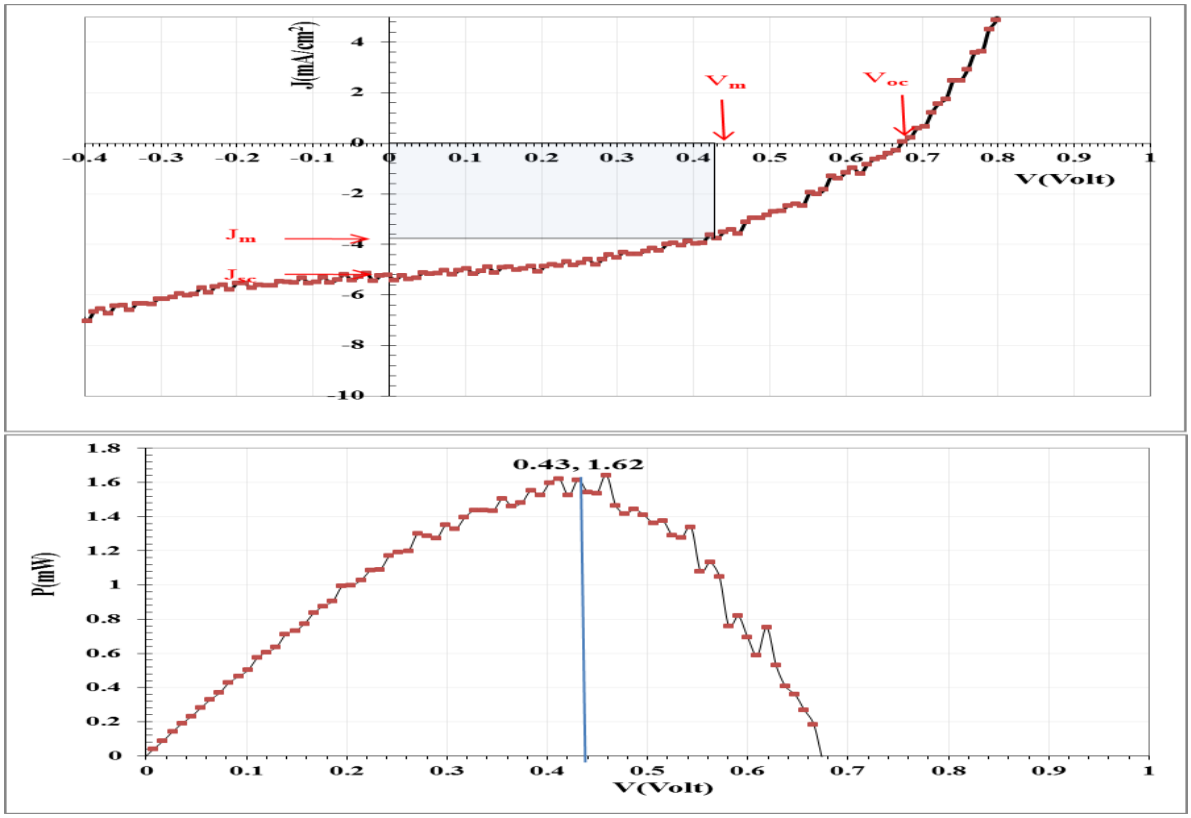

Figure 4.24:J-V and P-V curves for the solar cell coated by Au NPs.

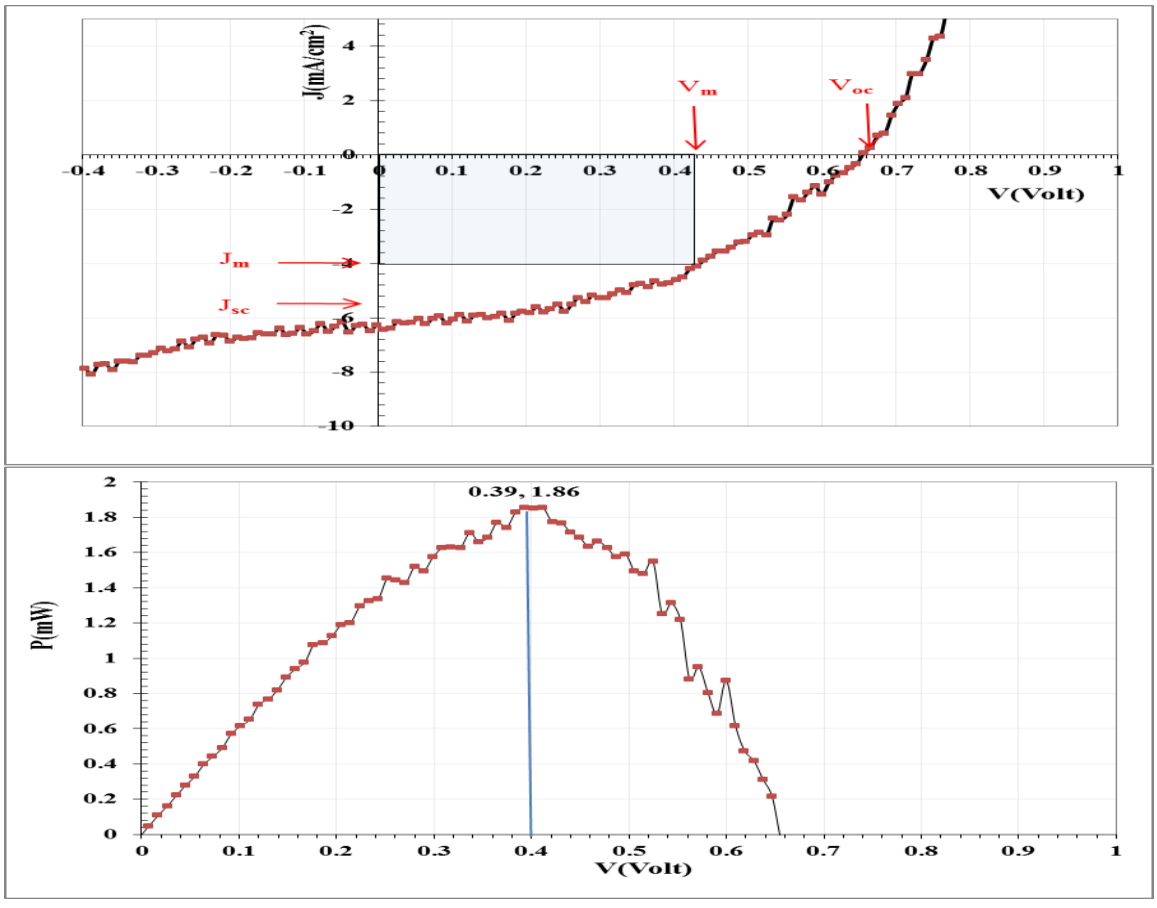

Figure 4.25:J-V and P-V curves for the solar cell coated by Au NPs : Ag NPs mixture

The solar cell characteristicsincluding the open-circuit voltage (V_{oc}), short-circuit current (Jsc), fill factor (FF), and solar efficiency (η) for these cells in the bare solar cell and that enhanced with the nanoparticles are summarized inTable4.10. The quantum efficiency increased from 1.36% of controlled cell to 1.55%, 1.62% and 1.89% of the PV cell coated by Au NPs, Ag NPs, and Au NPs : Ag NPs, respectively.

The solar cell is more enhanced in efficiency with Au NPs than the Ag NPs as their variation in plasmonic wavelength which falls about in the middle of spectral maximum cause more light harvesting. In addition, using mixed nanoparticles causes more enhancement due to the contribution of two absorption bands corresponding to the two NPs which cause harvesting more solar energy. For all coatings, the shunt resistance increased while the series resistance decreased indicating on the increase in the electron injection conductivity and reducing the recombination process [126].

Table 4.10: The specification of solar cell before and after treatment with Ag NPs, Au NPs, and Au NPs : Ag NPs mixture.

Parameters	Pure	With Ag NPs	With Au NPs	With Au NPs: Ag NPs
Jsc (mA)	4.40	5.00	5.20	6.40
V_{oc} (V)	0.65	0.65	0.67	0.65
J_m (mA)	3.40	3.78	3.77	4.85
V_m(v)	0.40	0.41	0.43	0.39
F.F	0.48	0.48	0.46	0.45
η%	1.36	1.55	1.62	1.89
R_{sh} (Ω)	181.36	394.16	339.56	234.74
R_s (Ω)	52.45	33.03	34.21	23.81

Chapter Five

Conclusions and Future works

5.1 Conclusion

In the present study, we have focused on the plasma spectra which is emitted from gold and silver metals under the influence of laser pulses. In addition, the Au NPs and Ag NPs are generated experimentally by pulsed laser ablation method with nanosecond laser pulses at 1064 nm at 600 number of pulses.

Moreover, the metals nanoparticles are mixed with each other in different proportions to be later cast on the surface of a solar cell for the purpose of improving its properties.

From this study, we can conclude the following:-

1- The results indicated obtaining quantitative plasma confinement, and thus the dimensions of the nanoparticles are very small which candidate for use in multiple scientific applications based on the plasma parameters resulting of the emission spectra.
2- The Silicon and glass substrates have a clear effect on the results the LIBS of plasma characteristics induced by pulsed laser as a result of the variation in the mechanism of laser-matter interaction.
3- The generation mechanism of seeds electron may reduce the breakdown threshold, so increase the intensity of characteristics lines and enhance the LIBS detection capability, especially for low absorption materials.
4- The plasma temperature and plasma number density of silver is higher than that of gold, this is due to the wavelength of the laser used to heat metals.
5- The FE-SEM results show of the metal nanoparticles of quasi-spherical morphology with an average size 13-20 nm.
6- The XRD patterns show of the metal nanoparticles of polycrystalline cubic structure, as well as the average crystallite size were (10.9, 12.1, and 11.9) nm of the Au NPs, Ag NPs, and their mixture, respectively.
7- Depositing the metal nanoparticles on the solar cells is highly enhanced their performance to harvest more energy by increasing the absorption inside the active layer at the plasmonic wavelength or by reducing the recombination

process by increasing surface conductivity. The absorbance is greater in the case of mixtures compared to pure elements, which leads to an increase in the efficiency of the solar cell.

5.2 Future Work

1. Studying the NELIBS using different lasers wavelength.
2. A study of the optical and structural properties of some semiconductors doped with different types of metals.
3. New solar cells can be built As a result of the increased efficiency based on grafting them with highly conductive materials.

References

References

[1] T. Gera, E. Nagy, T. Smausz, J. Budai, T. Ajtai, F. Kun-Szabó, Z. Homik, J. Kopniczky, Z. Bozóki, P. Szabó-Révész, R. Ambrus, and B. Hopp, "Application of pulsed laser ablation (PLA) for the size reduction of non-steroidal anti-inflammatory drugs (NSAIDs)," *Sci. Rep.*, vol. 10, no. 1, p. 15806, 2020.

[2] E. Fazio *et al.*, "Nanoparticles Engineering by Pulsed Laser Ablation in Liquids: Concepts and Applications," *Nanomaterials*, vol. 10, no. 11, p. 2317, 2020.

[3] S. Horikoshi and N. Serpone, "Introduction to Nanoparticles," in *Microwaves in Nanoparticle Synthesis*, 1st Ed., WILEY-VCH Verlag GmbH & Co. kGaA, 2013, pp. 1–24.

[4] D. A. Goncharova, T. S. Kharlamova, I. N. Lapin, and V. A. Svetlichnyi, "Chemical and Morphological Evolution of Copper Nanoparticles Obtained by Pulsed Laser Ablation in Liquid," *J. Phys. Chem. C*, vol. 123, no. 35, pp. 21731–21742, 2019.

[5] M. Dell'Aglio, A. Santagata, G. Valenza, A. De Stradis, and A. De Giacomo, "Study of the Effect of Water Pressure on Plasma and Cavitation Bubble Induced by Pulsed Laser Ablation in Liquid of Silver and Missed Variations of Observable Nanoparticle Features," *ChemPhysChem*, vol. 18, no. 9, pp. 1165–1174, 2017.

[6] C. De Mello Donegá, *Nanoparticles*, vol. 9783662448. Berlin, Heidelberg: Springer Berlin Heidelberg, 2014.

[7] C. Buzea and I. Pacheco, "Gold and silver nanoparticles: Properties and toxicity," in *Gold and Silver Nanoparticles*, Elsevier, 2023, pp. 59–82.

[8] M. Z. Butt, "Laser ablation characteristics of metallic materials: Role of Debye-Waller thermal parameter," *IOP Conf. Ser. Mater. Sci. Eng.*, vol. 60, no. 1, p. 012068, 2014.

References

[9] A. A. Menazea, "Femtosecond laser ablation-assisted synthesis of silver nanoparticles in organic and inorganic liquids medium and their antibacterial efficiency," *Radiat. Phys. Chem.*, vol. 168, p. 108616, 2020.

[10] M. Dell'Aglio, R. Alrifai, and A. De Giacomo, "Nanoparticle Enhanced Laser Induced Breakdown Spectroscopy (NELIBS), a first review," *Spectrochim. Acta Part B At. Spectrosc.*, vol. 148, pp. 105–112, 2018.

[11] D. A. Cremers and L. J. Radziemski, "History and fundamentals of LIBS," in *Laser-Induced Breakdown Spectroscopy (LIBS)*, A. W. Miziolek, V. Palleschi, and I. Schechter, Eds. Cambridge: Cambridge University Press, 2009, pp. 1–39.

[12] C. Koral, M. Dell'Aglio, R. Gaudiuso, R. Alrifai, M. Torelli, and A. De Giacomo, "Nanoparticle-Enhanced Laser Induced Breakdown Spectroscopy for the noninvasive analysis of transparent samples and gemstones," *Talanta*, vol. 182, pp. 253–258, 2018.

[13] S. Iqbal, X. Guo, J. Nanxi, and T. Zhang, "Advances in solar cell fabrication and applications using nanotechnology," in *Solar Energy Harvesting, Conversion, and Storage*, Elsevier, 2023, pp. 223–250.

[14] M. hosein Mohammadi, M. Eskandari, and D. Fathi, "Effects of the location and size of plasmonic nanoparticles (Ag and Au) in improving the optical absorption and efficiency of perovskite solar cells," *J. Alloys Compd.*, vol. 877, p. 160177, 2021.

[15] De Giacomo, A., Gaudiuso, R., Koral, C., Dell'Aglio, M., & De Pascale, O. (2013). Nanoparticle-enhanced laser-induced breakdown spectroscopy of metallic samples. Analytical chemistry, 85(21), 10180-10187.

[16] DE GIACOMO, A., et al. Nanoparticle Enhanced Laser Induced Breakdown Spectroscopy: Effect of nanoparticles deposited on sample surface on laser ablation and plasma emission. Spectrochimica Acta Part B: Atomic Spectroscopy, 2014, 98: 19-27.

[17] L. Sládková, D. Prochazka, P. Pořízka, P. Škarková, M. Remešová, A.

Hrdlička, K. Novotný, L. Čelko, and J. Kaiser, "Improvement of the Laser-Induced Breakdown Spectroscopy method sensitivity by the usage of combination of Ag-nanoparticles and vacuum conditions," *Spectrochim. Acta Part B At. Spectrosc.*, vol. 127, pp. 48–55, 2017.

[18] A. M. EL Sherbini, A. E. EL Sherbini, C. G. Parigger, and T. M. EL Sherbini, "Nano-particle enhancement of diagnosis with Laser-Induced plasma spectroscopy," *J. Phys. Conf. Ser.*, vol. 1253, no. 1, p. 012002, 2019.

[19] SALAJKOVÁ, Zita, et al. Effect of spherical gold nanoparticles size on nanoparticle enhanced laser induced breakdown spectroscopy. Spectrochimica Acta Part B: Atomic Spectroscopy, 2021, 179: 106105 .

[20] A. F. Ahmed, M. R. Abdulameer, M. M. Kadhim, and F. A.-H. Mutlak, "Plasma parameters of Au nano-particles ablated on porous silicon produced via Nd-YAG laser at 355 nm for sensing NH3 gas," *Optik (Stuttg).*, vol. 249, p. 168260, 2022.

[21] H. M. Fadhil, K. I. Hassoon, and H. A. Salih, "Structural and Spectroscopic Analysis for Silver Bulk and Nanoparticles," *Karbala Int. J. Mod. Sci.*, vol. 8, no. 2, pp. 52–62, 2022.

[22] S. K. Hameed, N. A. Razzak, A. F. Mahood, and K. L. Nahi, "Optical Emission Spectroscopy of Laser-Produced Plasmas of Some Metal Targets," *Iraqi J. Appl. Phys.*, vol. 18, no. 1, pp. 15–20, 2022.

[23] M. R. Khan, S. U. Haq, Q. Abbas, and A. Nadeem, "Improvement in signal sensitivity and repeatability using copper nanoparticle-enhanced laser-induced breakdown spectroscopy," *Spectrochim. Acta Part B At. Spectrosc.*, vol. 195, p. 106507, 2022.

[24] AHMED, Nasar, et al. The emission intensity enhancement and improved limit of detection of Cu, Ag, and Au using electric field assisted LIBS. Optical Materials, 2023, 143: 114309

[25] H. O. Pierson, *Handbook of Chemical Vapor Deposition*. New Jersey: William Andrew Publishing, 1999.

[26] A. A. Ruddyard, D. S. Soejoko, and Nurlely, "Effect of the quantity of carbonate components and sintering parameters on the quality of hydrothermally synthesized carbonate hydroxyapatite," in *AIP Conference Proceedings*, 2017, vol. 1862, p. 030070.

[27] A. Al Baroot, M. Alheshibri, Q. A. Drmosh, S. Akhtar, E. Kotb, and K. A. Elsayed, "A novel approach for fabrication ZnO/CuO nanocomposite via laser ablation in liquid and its antibacterial activity," *Arab. J. Chem.*, vol. 15, no. 2, pp. 103606–13, 2022.

[28] J. Cao, "Laser Pulse Duration Optimization for Photothermal Therapy with Gold Nanostars," *Int. J. Med. Physics, Clin. Eng. Radiat. Oncol.*, vol. 07, pp. 391–402, 2018.

[29] J. Zhang, J. Claverie, M. Chaker, and D. Ma, "Colloidal Metal Nanoparticles Prepared by Laser Ablation and their Applications," *ChemPhysChem*, vol. 18, no. 9, pp. 986–1006, 2017.

[30] M. S. Brown and C. B. Arnold, *Laser Precision Microfabrication*. Springer-Verlag Berlin Heidelberg, 2010.

[31] N. Kumar, S. Dash, A. Tyagi, and B. Raj, "Dynamics of plasma expansion in the pulsed laser material," *Sadhana,Indian Acad. Sci*, vol. 35, pp. 493–511, 2010.

[32] R. Bernath, C. G. Brown, J. Aspiotis, M. Fisher, and M. Richardson, "Shock-wave generation in transparent media from ultra-fast lasers," *SPIE*, vol. 6219, pp. 62190–62195, 2006.

[33] S. Link, C. Burda, Z. L. Wang, and M. A. El-Sayed, "Electron dynamics in gold and gold–silver alloy nanoparticles: The influence of a nonequilibrium electron distribution and the size dependence of the electron–phonon relaxation," *J. Chem. Phys.*, vol. 111, no. 3, pp. 1255–1264, 1999.

[34] S. J. Hill, *Inductively Coupled Plasma Spectrometry and its Applications*. Oxford, UK: Blackwell Publishing Ltd, 2006.

[35] G. James, B. Stephen, P. Tina, and P. Hua, "An 11.5 W Yb:YAG planar

waveguide laser fabricated via pulsed laser deposition," *Opt. Mater. Express.*, vol. 1, pp. 1–5, 2016.

[36] E. Karahan, D. Er, and S. Kaynak, "An Overview of Nd:YAG Laser Capsulotomy.," *Medical hypothesis, discovery & innovation ophthalmology journal*, vol. 3, no. 2. pp. 45–50, 2014.

[37] L. Hribar, P. Gregorčič, M. Senegačnik, and M. Jezeršek, "The Influence of the Processing Parameters on the Laser-Ablation of Stainless Steel and Brass during the Engraving by Nanosecond Fiber Laser," *Nanomaterials*, vol. 12, no. 2, p. 232, 2022.

[38] J. Polte, "Fundamental growth principles of colloidal metal nanoparticles – a new perspective," *CrystEngComm*, vol. 17, no. 36, pp. 6809–6830, 2015.

[39] K. Chaudhary, S. Z. H. Rizvi, and J. Ali, "Laser-Induced Plasma and its Applications," in *Plasma Science and Technology - Progress in Physical States and Chemical Reactions*, InTech, 2016.

[40] X. Wang, R. Liu, Y. He, Y. Fu, J. Wang, A. Li, X. Guo, M. Wang, W. Guo, T. Zhang, Q. Shu, and Y. Yao, "Determination of detonation characteristics by laser-induced plasma spectra and micro-explosion dynamics," *Opt. Express*, vol. 30, no. 4, p. 4718, 2022.

[41] X. Li and Y. Guan, "Theoretical fundamentals of short pulse laser–metal interaction: A review," *Nanotechnol. Precis. Eng.*, vol. 3, no. 3, pp. 105–125, 2020.

[42] L. Torrisi, "Laser–matter interaction and plasma production: methodologies, radiation emission, diagnostics and applications," *Radiat. Eff. Defects Solids*, vol. 170, no. 4, pp. 239–240, 2015.

[43] Y. Ishikawa, N. Koshizaki, and S. Sakaki, "Spherical Particle Formation Mechanism in Pulsed Laser Melting in Liquid under Controlled-Pulse-Number Irradiation using a Slit Nozzle Flow System," *J. Phys. Chem. C*, vol. 123, no. 40, pp. 24934–24942, 2019.

[44] J. Xiao, P. Liu, C. X. Wang, and G. W. Yang, "External field-assisted laser

ablation in liquid: An efficient strategy for nanocrystal synthesis and nanostructure assembly," *Prog. Mater. Sci.*, vol. 87, pp. 140–220, 2017.

[45] S. Pal, U. Jana, P. Manna, G. Mohanta, and R. Manavalan, "Nanoparticle : An overview of preparation and characterization," *J. Appl. Pharm. Sci.*, vol. 01, no. 06, pp. 228–234, 2011.

[46] C. Buzea, I. Pacheco, I. Blandino, and K. Robbie, "Nanomaterials and nanoparticles: sources and toxicity," *Biointerphases*, vol. 2, pp. 1–10, 2007.

[47] C. L. Jung, S. C. Park, and H. Lim, "Synthesis of Surface-Reinforced Biodegradable Chitosan Nanoparticles and Their Application in Nanostructured Antireflective and Self-Cleaning Surfaces," *ACS Appl. Mater. Interfaces*, vol. 11, no. 43, pp. 40835–40841, 2019.

[48] L. Zhang, X. Fang, and C. Ye, *Controlled Growth of Nanomaterials*. World Scientific, 2007.

[49] N. Baig, I. Kammakakam, W. Falath, and I. Kammakakam, "Nanomaterials: A review of synthesis methods, properties, recent progress, and challenges," *Mater. Adv.*, vol. 2, no. 6, pp. 1821–1871, 2021.

[50] F. Kong, J. Zhang, R. Li, and Z. Wang, "Unique roles of gold nanoparticles in drug delivery, targeting and imaging applications," *Molecules*, vol. 22, pp. 1–7, 2017.

[51] V. E. Bochenkov and G. B. Sergeev, "Sensitivity, Selectivity, and Stability of Gas-Sensitive Metal-Oxide Nanostructures.," in *Metal Oxide Nanostructures and Their Applications*, vol. 3, 2010, pp. 31–52.

[52] G. H. Chan, J. Zhao, E. M. Hicks, G. C. Schatz, and R. P. Van Duyne, "Plasmonic properties of copper nanoparticles fabricated by nanosphere lithography," *Nano Lett. Nano Lett, Nano Lett*, vol. 7, no. 7, pp. 1947–1952, 2007.

[53] S. K. Ghosh, "Composite materials handbook," *J. Mech. Work. Technol.*, vol. 11, no. 1, pp. 126–132, 1985.

[54] S. Phetsang, S. Nootchanat, C. Lertvachirapaiboon, R. Ishikawa, K. Shinbo,

K. Kato, P. Mungkornasawakul, K. Ounnunkad, and A. Baba, “Enhancement of organic solar cell performance by incorporating gold quantum dots (AuQDs) on a plasmonic grating,” *Nanoscale Adv.*, vol. 2, no. 7, pp. 2950–2957, 2020.

[55] G. M. Baker and E. A. Wright, “Treatment of Mouse Mammary Tumors Using Combined Hyperthermia and Ischemia,” *Natl. Cent. Biotechnol. Inf.*, vol. 43, pp. 3392–3397, 1983.

[56] H. Esmaeili, J. Hadian, M. H. Mirjalili, and H. Rezadoost, “The effect of activated charcoal and multi-walled carbon nanotubes on the growth , rosmarinic and caffeic acid content , total phenol , total flavonoid and antioxidant activity of Satureja rechingeri calluses,” vol. 6, no. 5, pp. 297–304, 2015.

[57] A. Ito and T. Kobayashi, “Intracellular Hyperthermia Using Magnetic Nanoparticles: A Novel Method for Hyperthermia Clinical Applications,” *Therm. Med.*, vol. 24, pp. 113–129, 2008.

[58] A. Bajaj, O. Miranda, and I.-B. Kim, “Detection and differentiation of normal, cancerous, and metastatic cells using nanoparticle-polymer sensor arrays,” *Proc. Nail. Acad. Sci. USA*, vol. 106, no. 27, pp. 10912–10916, 2009.

[59] O. Salata, “Applications of nanoparticles in biology and medicine.,” *Journal of nanobiotechnology*, vol. 2. pp. 1–6, 2004.

[60] J. Uddin, “Terahertz multispectral imaging for the analysis of gold nanoparticles’ size and the number of unit cells in comparison with other techniques,” *Int. J. Biosens. Bioelectron.*, vol. 4, no. 3, 2018.

[61] D. R. Lide, “CRC Handbook of Chemistry and Physics, 84th Edition, 2003-2004,” *Handb. Chem. Phys.*, vol. 53, p. 2616, 2003.

[62] C. Dupas, *Nanoscience*. Belin, France: Springer, 2007.

[63] H. S.Nalwa, “Encyclopedia of Nanoscience and Nanotechnology,” *Am. Sci.*, vol. 3, no. 1, pp. 29–40, 2004.

[64] R. Kuladeep, L. Jyothi, K. S. Alee, K. L. N. Deepak, and D. N. Rao, “Laser-

assisted synthesis of Au-Ag alloy nanoparticles with tunable surface plasmon resonance frequency," *Opt. Mater. Express*, vol. 2, no. 2, pp. 161–170, 2012.

[65] P. Yang, *The Chemistry of Nano Structured Materials*. Printed in Singapore.: World Scientific Publishing Co. Pte. Ltd., 2003.

[66] Y. Hong, Y.-M. Huh, D. S. Yoon, and J. Yang, "Nanobiosensors Based on Localized Surface Plasmon Resonance for Biomarker Detection," *J. Nanomater.*, vol. 2012, pp. 1–13, 2012.

[67] M. Chen, Y. He, J. Huang, and J. Zhu, "Synthesis and solar photo-thermal conversion of Au , Ag , and Au-Ag blended plasmonic nanoparticles Synthesis and solar photo-thermal conversion of Au , Ag , and Au-Ag blended plasmonic nanoparticles," *Energy Convers. Manag.*, vol. 127, no. November, pp. 293–300, 2016.

[68] W. Chang and X. Luo, "Laser-Assisted Machining," in *Hybrid Machining*, Elsevier, 2018, pp. 43–76.

[69] A. Zarrabi and A. J. Gross, "The evolution of lasers in urology," *Ther. Adv. Urol.*, vol. 3, no. 2, pp. 81–89, 2011.

[70] J. Šulc and H. Jelínková, "Solid-state lasers for medical applications," in *Lasers for Medical Applications*, Elsevier, 2013, pp. 127–176.

[71] P. J. Trim and M. F. Snel, "Small molecule MALDI MS imaging: Current technologies and future challenges," *Methods*, vol. 104, pp. 127–141, 2016.

[72] L. P. Vera-Londoño, J. A. Pérez-Taborda, and H. Riascos-Landázuri, "Spectroscopic analysis of coal plasma emission produced by laser ablation," *Rev. Fac. Ing. Univ. Antioquia*, no. 78, 2015.

[73] R. Noll, *Laser-Induced Breakdown Spectroscopy*. Berlin, Heidelberg: Springer Berlin Heidelberg, 2012.

[74] Y. Li, T. Liu, C. Chen, Y. Lee, and A. Yabushita, "Laser induced breakdown spectroscopy of pure aluminum with high temporal resolution," *Opt. Express*, vol. 21, no. 18, p. 21579, 2013.

[75] A. M. Abdelghany, A. A. Menazea, M. A. Abd-EllMaksoud, and T. K.

Khatab, “Pulsed laser ablated zeolite nanoparticles: A novel nano-catalyst for the synthesis of 1,8-dioxo-octahydroxanthene and N -aryl-1,8-dioxodecahydroacridine with molecular docking validation,” *Appl. Organomet. Chem.*, vol. 34, no. 2, 2020.

[76] S. Marino, S. Palanco, M. Gabás, R. Romero, and J. R. Ramos-Barrado, “Laser nano- and micro-structuring of silicon using a laser-induced plasma for beam conditioning,” *Nanotechnology*, vol. 26, no. 5, p. 055303, 2015.

[77] K. A. Aadim, M. A. Khalafand, and W. D. Hussain, “Diagnosis and analysis of laser induced plasma parameters for silicon carbide produced by Nd:YAG laser,” 2021, p. 080010.

[78] F. J. Fortes, J. Moros, P. Lucena, L. M. Cabal??n, and J. J. Laserna, *Laser-induced breakdown spectroscopy*, vol. 85, no. 2. 2013.

[79] A. De Giacomo, R. Gaudiuso, C. Koral, M. Dell’Aglio, and O. De Pascale, “Nanoparticle Enhanced Laser Induced Breakdown Spectroscopy: Effect of nanoparticles deposited on sample surface on laser ablation and plasma emission,” *Spectrochim. Acta Part B At. Spectrosc.*, vol. 98, pp. 19–27, 2014.

[80] S. Y. Davydov, “On the relationship between the ionization potential and the work function: Metals,” *Tech. Phys.*, vol. 47, no. 1, pp. 92–96, 2002.

[81] A. De Giacomo, M. Dell’Aglio, R. Gaudiuso, C. Koral, and G. Valenza, “Perspective on the use of nanoparticles to improve LIBS analytical performance: nanoparticle enhanced laser induced breakdown spectroscopy (NELIBS),” *J. Anal. At. Spectrom.*, vol. 31, no. 8, pp. 1566–1573, 2016.

[82] P. K. Chu and X. Lu, *Low Temperature Plasma Technology*. Parkway: Taylor & Francis Group, LLC, 2014.

[83] M. W. Morooka, J. E. Wahlund, D. J. Andrews, A. M. Persoon, S. Y. Ye, W. S. Kurth, D. A. Gurnett, and W. M. Farrell, “The Dusty Plasma Disk Around the Janus/Epimetheus Ring,” *J. Geophys. Res. Sp. Phys.*, vol. 123, no. 6, pp. 4668–4678, 2018.

[84] *Different plasma realizations in the density-temperature plane.*

Strongly coupled plasmas are located right from the Γ=1 line, with Γ the ratio between the average interaction energy of the heavy species and its thermal energy. After Donko et al. [2007], https://arxiv.org/abs/0710.5229 .

[85] H. C. Kim, F. Iza, S. S. Yang, M. Radmilović-Radjenović, and J. K. Lee, "Particle and fluid simulations of low-temperature plasma discharges: benchmarks and kinetic effects," *J. Phys. D. Appl. Phys.*, vol. 38, no. 19, pp. R283–R301, 2005.

[86] Z. Farooq, R. Ali, U. S. Qurashi, M. H. Mahmood, M. Yaseen, M. A. Qayyum, M. N. Hussain, S. M. Shah, and T. Jan, "Spectroscopic studies of laser produced plasma of doped nano-structured material by laser induced breakdown spectroscopy," *Phys. Plasmas*, vol. 25, no. 9, p. 093106, 2018.

[87] C. Fallon, "Optical Diagnostics of Colliding Laser Produced Plasmas : Towards Next Generation Plasma Light Sources," Dublin City University, 2013.

[88] D. M. Devia, L. V Rodriguez-Restrepo, and E. Restrepo-Parra, "Methods Employed in Optical Emission Spectroscopy Analysis," *Ing. y Cienc.*, vol. 11, no. 21, pp. 239–267, 2015.

[89] M. Guillermin, J. P. Colombier, S. Valette, E. Audouard, F. Garrelie, and R. Stoian, "Optical emission and nanoparticle generation in Al plasmas using ultrashort laser pulses temporally optimized by real-time spectroscopic feedback," *Phys. Rev. B*, vol. 82, no. 3, p. 035430, 2010.

[90] M. Zhukov, *Plasma Diagnostics*, vol. 22, no. 1. Mosco: Lightning Source UK Ltd, 2005.

[91] D. M. Devia, L. V Rodriguez-Restrepo, and E. Restrepo-Parra, "Methods Employed in Optical Emission Spectroscopy Analysis: a Review," *Ing. y Cienc.*, vol. 11, no. 21, pp. 239–267, 2015.

[92] S. S. Hamed, "Spectroscopic Determination of Excitation Premixed Laminar Flame," *Egypt. J. Solids*, vol. 28, no. 2, pp. 349–357, 2005.

[93] V. Unnikrishnan, K. Alti, V. Kartha, C. Santhosh, G. Gupta, and B. Suri, "Measurements of plasma temperature and electron density in laser-induced copper plasma by time-resolved spectroscopy of neutral atom and ion emissions," *Pramana - J. Phys.*, vol. 74, no. 6, pp. 983–993, 2010.

[94] X. F. Li, W. D. Zhou, and Z. F. Cui, "Temperature and electron density of soil plasma generated by LA-FPDPS," *Front. Phys.*, vol. 7, no. 6, pp. 721–727, 2012.

[95] A. A. Qureshi, S. Javed, H. M. A. Javed, A. Akram, M. S. Mustafa, U. Ali, and M. Z. Nisar, "Facile formation of SnO2–TiO2 based photoanode and Fe3O4@rGO based counter electrode for efficient dye-sensitized solar cells," *Mater. Sci. Semicond. Process.*, vol. 123, p. 105545, 2021.

[96] R. Belu, *Fundamentals and Source Characteristics of Renewable Energy Systems*, 1st editio. CRC Press, 2020.

[97] M. Uchqun and T. Jahongir, "The Research of the V-I Characteristics of a Solar Panel Using a Computerized Measuring Bench 'EPH 2 Advanced Photovoltaics Trainer,'" *Autom. Control Intell. Syst.*, vol. 7, no. 3, p. 79, 2019.

[98] M. Anitha, K. Saravanakumar, N. Anitha, and L. Amalraj, "Influence of fluorine doped CdO thin films by an simplified spray pyrolysis technique using nebulizer," *Opt. Quantum Electron.*, vol. 51, no. 6, pp. 1–22, 2019.

[99] T. Shen, S. Siontas, and D. Pacifici, "Plasmon-Enhanced Thin-Film Perovskite Solar Cells," *J. Phys. Chem. C*, vol. 122, no. 41, pp. 23691–23697, 2018.

[100] A. A. Tabrizi and A. Pahlavan, "Efficiency improvement of a silicon-based thin-film solar cell using plasmonic silver nanoparticles and an antireflective layer," *Opt. Commun.*, vol. 454, p. 124437, 2020.

[101] M. Li, N. Yuan, Y. Tang, L. Pei, Y. Zhu, J. Liu, L. Bai, and M. Li, "Performance optimization of dye-sensitized solar cells by gradient-ascent architecture of SiO2@Au@TiO2 microspheres embedded with Au

nanoparticles," *J. Mater. Sci. Technol.*, vol. 35, no. 4, pp. 604–609, 2019.

[102] P. Yu, F. Zhang, Z. Li, Z. Zhong, A. Govorov, L. Fu, H. Tan, C. Jagadish, and Z. Wang, "Giant optical pathlength enhancement in plasmonic thin film solar cells using core-shell nanoparticles," *J. Phys. D. Appl. Phys.*, vol. 51, no. 29, p. 295106, 2018.

[103] H.-Y. Jung, I.-S. Yeo, T.-U. Kim, H.-C. Ki, and H.-B. Gu, "Surface plasmon resonance effect of silver nanoparticles on a TiO2 electrode for dye-sensitized solar cells," *Appl. Surf. Sci.*, vol. 432, pp. 266–271, 2018.

[104] X. He, Y. Guo, X. Li, and J. Liu, "In situ ligand-free growth of TiO2-escapsulated Au nanocomposites on photoanode for efficient dye sensitized solar cells," *Chem. Eng. J.*, vol. 396, p. 125302, 2020.

[105] W.-Y. Rho, D. H. Song, H.-Y. Yang, H.-S. Kim, B. S. Son, J. S. Suh, and B.-H. Jun, "Recent advances in plasmonic dye-sensitized solar cells," *J. Solid State Chem.*, vol. 258, pp. 271–282, 2018.

[106] M. Guo, J. Chen, J. Zhang, H. Su, L. Liu, N. Fu, and K. Xie, "Coupling plasmonic nanoparticles with TiO2 nanotube photonic crystals for enhanced dye-sensitized solar cells performance," *Electrochim. Acta*, vol. 263, pp. 373–381, 2018.

[107] W. H. Bragg and W. L. Bragg, *X Rays and Crystal Structure*. London: G. Bell and Sons, LTD., 1918.

[108] P. Scherrer, "Göttinger Nachrichten Gesell," *Univ. zu Göttingen*, vol. 2, p. 98, 1918.

[109] D. Raha and D. Das, "Nanocrystalline silicon thin films prepared by low pressure planar inductively coupled plasma," *J. Appl.Surf. Sci.*, vol. 276, pp. 249–257, 2013.

[110] "NIST Atomic Spectra Database (ver. 4.1.0)." [Online]. Available: http://kinetics.nist.gov/index.php.

[111] F. Bredice, P. Pacheco Martinez, C. Sánchez-Aké, and M. Villagrán-Muniz, "Temporal evolution of the spectral lines emission and temperatures in laser

induced plasmas through characteristic parameters," *Spectrochim. Acta Part B At. Spectrosc.*, vol. 107, pp. 25–31, 2015.

[112] J. F. Kielkopf and N. F. Allard, "Shift and width of the Balmer series H α line at high electron density in a laser-produced plasma," *J. Phys. B At. Mol. Opt. Phys.*, vol. 47, no. 15, p. 155701, 2014.

[113] B. Zmerli, B. Nessib, and M. S. Dimitrijevi, "On the Stark broadening of CuI spectral lines," vol. 15, pp. 152–156, 2010.

[114] S. Hashimoto, D. Werner, and T. Uwada, "Studies on the interaction of pulsed lasers with plasmonic gold nanoparticles toward light manipulation, heat management, and nanofabrication," *J. Photochem. Photobiol. C Photochem. Rev.*, vol. 13, no. 1, pp. 28–54, 2012.

[115] N. Konjević and W. L. Wiese, "Experimental Stark widths and shifts for spectral lines of neutral and ionized atoms," *J. Phys. Chem. Ref. Data*, vol. 19, no. 6, pp. 1307–1385, 1990.

[116] S. M. Karazi, I. U. Ahad, and K. Y. Benyounis, "Laser Micromachining for Transparent Materials," in *Reference Module in Materials Science and Materials Engineering*, Elsevier, 2017.

[117] M. Dell'Aglio, R. Alrifai, and A. De Giacomo, "Nanoparticle Enhanced Laser Induced Breakdown Spectroscopy (NELIBS), a first review," *Spectrochim. Acta Part B At. Spectrosc.*, vol. 148, pp. 105–112, 2018.

[118] D. R. A. El-Hafiz, M. A. Ebiad, and A. A. E. Sakr, "Ultrasonic-Assisted Nano-Nickel Ferrite Spinel Synthesis for Natural Gas Reforming," *J. Inorg. Organomet. Polym. Mater.*, vol. 31, pp. 1–10, 2021.

[119] R. Borah and S. W. Verbruggen, "Effect of size distribution, skewness and roughness on the optical properties of colloidal plasmonic nanoparticles," *Colloids Surfaces A Physicochem. Eng. Asp.*, vol. 640, p. 128521, 2022.

[120] F. Castillo, E. De la Rosa, and E. Pérez, "Gold aggregates on silica templates and decorated silica arrays for SERS applications," *Eur. Phys. J. D*, vol. 63, no. 2, pp. 301–306, 2011.

[121] Y. Mansour, Y. Battie, A. En Naciri, and N. Chaoui, "Determination of the Size Distribution of Metallic Colloids from Extinction Spectroscopy," *Nanomaterials*, vol. 11, no. 11, p. 2872, 2021.

[122] C.-C. Huang, H.-J. Chen, Q. L. Leong, W. K. Lai, C.-Y. Hsu, J.-C. Chen, and C.-L. Huang, "Synthesis of silver nanoplates with a narrow LSPR band for chemical sensing through a plasmon-mediated process using photochemical seeds," *Materialia*, vol. 21, p. 101279, 2022.

[123] Q. Liu, Y. Wei, M. Z. Shahid, M. Yao, B. Xu, G. Liu, K. Jiang, and C. Li, "Spectrum-enhanced Au@ZnO plasmonic nanoparticles for boosting dye-sensitized solar cell performance," *J. Power Sources*, vol. 380, pp. 142–148, 2018.

[124] V. S. Manikandan, A. K. Palai, S. Mohanty, and S. K. Nayak, "Surface plasmonic effect of Ag enfold ZnO pyramid nanostructured photoanode for enhanced dye sensitized solar cell application," *Ceram. Int.*, vol. 44, no. 17, pp. 21314–21322, 2018.

[125] T. Solaiyammal and P. Murugakoothan, "Green synthesis of Au and the impact of Au on the efficiency of TiO2 based dye sensitized solar cell," *Mater. Sci. Energy Technol.*, vol. 2, no. 2, pp. 171–180, 2019.

[126] W.-Y. Rho, H.-S. Kim, W.-J. Chung, J. S. Suh, B.-H. Jun, and Y.-B. Hahn, "Enhancement of power conversion efficiency with TiO2 nanoparticles/nanotubes-silver nanoparticles composites in dye-sensitized solar cells," *Appl. Surf. Sci.*, vol. 429, pp. 23–28, 2018.

الخلاصة

ركزت الدراسة الحالية على أطياف البلازما المنبعثة من معادن الذهب والفضة تحت تأثير نبضات الليزر. ولتحقيق هذا الغرض تم استخدام ليزر Nd:YAG عند الطول الموجي ١٠٦٤ نانومتر، ومدة النبضة ١٠ نانو ثانية ، وطاقة الليزر ١٠٠ ملي جول، والتردد ٦ هرتز، وعدد النبضات ٦٠٠ نبضة تركز مباشرة على الأهداف المعدنية.

علاوة على ذلك، يتم تصنيع جزيئات الذهب والفضة النانوية بشكل تجريبي باستخدام الاستئصال بالليزر النبضي في السوائل. تم بعد ذلك ترسيب الجسيمات النانوية المعدنية على ركائز السيليكون والزجاج بطريقة الغمس، وتمت دراسة أطياف انبعاثها باستخدام تقنية التحليل الطيفي للانهيار المستحث بالليزر (LIBS).

وبالتالي، يتم إجراء مقارنة بين الأهداف السائبة والركائز المعززة بالنانو. يتم حساب معلمات البلازما مثل درجة الحرارة والكثافة والتردد وطول ديباي. وكذلك يتم قياس الخواص البصرية والهيكلية والكهربائية عن طريق قياس خصائص الأشعة فوق البنفسجية و المرئية، XRD، FE-SEM وIV، على التوالي. وأخيرا، يتم ترسيب جزيئات الذهب والفضة النانوية وخليطها على سطح الخلية الشمسية لتحسين كفاءتها.

أثبتت النتائج التي توصلنا اليها أن الفضة لها معاملات بلازما أكبر من الذهب، وذلك بسبب الطول الموجي لليزر المستخدم، مما يجعل الفضة تمتص ضوء الليزر أكثر من الذهب، وهذه النتيجة تتفق مع نتائج الامتصاص. تم الحصول على زيادة في معلمات البلازما عند مقارنة معلمات البلازما قبل وبعد ترسيب الجسيمات النانوية على ركائز الزجاج والسيليكون.

أظهرت نتائج FE-SEM للجسيمات النانوية أشكال كروية بمتوسط حجم (١٣.٩، ١٢.٠٩، ١٨.٣٨) نانومتر بينـما أظـهرت نتائج XRD حجم البلـورة الذي بلغ (١٠.٩، ١٢.١، ١١.٩) نانومتر لكل من الـ (Au NPs، Ag NPsومخالطيها) ، على التوالي.

أثبتت النتائج أيضًا أنه يمكن استخدام تقنية NELIBS لتحسين العينات منخفضة الامتصاص دون ان تسبب في حدوث شقوق داخلية في العينة. قد تؤدي هذه الآلية إلى خفض عتبة الانهيار لـ Si، وبالتالي زيادة شدة خطوط الانبعاث مما يؤدي إلى تعزيز إمكانية اكتشاف LIBS، خاصة بالنسبة لنطاق الطول الموجي من ٤٠٠ إلى ٥٥٠ نانومتر. وذلك لأن الاختلاف في آلية تفاعل إشعاع الليزر مع الجسيمات النانوية الموجودة يؤدي إلى تعزيز خط الانبعاث.

وأخيرا، أدى ترسيب الجسيمات النانوية المعدنية على أسطح الخلايا الشمسية إلى تحسين أدائها للحصول على المزيد من الطاقة عن طريق زيادة الامتصاص داخل الطبقة النشطة عند الطول الموجي البلازموني أو عن طريق تقليل عملية إعادة التركيب عن طريق زيادة الموصلية السطحية.

جمهورية العراق
وزارة التعليم العالي والبحث العلمي
جامعة بابل
كلية العلوم للبنات
قسم فيزياء الليزر

دراسة اطياف أنبعاث البلازما للذهب والفضة النانوية المحضرة بواسطة الاستئصال بالليزر

رسالة مقدمة الى مجلس كلية العلوم للبنات في جامعة بابل

وهي جزء من متطلبات نيل درجة الماجستير في علوم فيزياء الليزر

من قبل

براء حسام علي

بأشراف

أ.م.د لازم حسن عبود

م.د محمد جواد جادر

٢٠٢٣م

١٤٤٥ هـ